INCLUSIVE STUDY

OF

200 GeV/c PI-NEON INTERACTIONS

by

Henry Reyer Band
Department of Physics
Duke University

Date:_____

Approved:

_____
William D. Walker, supervisor

_____

_____

_____

_____

Dissertation submitted in partial fulfillment of
the requirements for the degree of Doctor
of Philosophy in the Department of
Physics in the Graduate School
of Duke University

1980

DE-AS05-76ER03065

DISCLAIMER

Abstract

Physics - Particle

INCLUSIVE STUDY

OF

200 GeV/c PI-NEON INTERACTIONS

by

Henry Reyer Band
Department of Physics
Duke University

Date:_____

Approved:

_____
William D. Walker, supervisor

_____

_____

_____

_____

An abstract of a dissertation submitted in partial fulfillment of the requirements for the degree of Doctor of Philosophy in the Department of Physics in the Graduate School of Duke University

1980

ABSTRACT

200 GeV/c pi-neon interactions are studied in the Fermilab 30 inch bubble chamber which was filled with a neon - hydrogen mixture (31 molar % neon). Scan results and measurements of a representative event sample yield proton, gamma and pion multiplicities and single particle spectra.

R was measured to be 1.21 $\pm$ 0.05 for both $pi^{\pm}$ and pi^{0}. Nearly identical to lower energy measurements, R is strongly dependent on the number of observed protons in the event. KNO scaling is observed for the corrected multiplicity distributions. Scaling, however, appears violated if events with a fixed number of protons are considered.

Study of the pion single particle spectra show the excess particle production of the neon target over that of hydrogen is largest in the target fragmentation region and nearly constant (1.28$\pm$ 0.02) in the central production region. The dependence of the pion rapidity distribution on the number of protons is consistent with collisions on either one or two nucleons.

The $s^{-1/2}$ dependence of the $p_{||}$ spectra is very similar to that seen in hydrogen, with limiting fragmentation reached only for beam energies much greater than 200 GeV/c. The

proton momentum distribution is energy independent with the protons carrying proportionally less of the bombarding energy as s increases.

ACKNOWLEDGEMENTS

I would like to thank Dr. W.D.Walker for giving me the opportunity to undertake this thesis and for his guidance and support throughout this work. Many members of the Duke high energy group have been of invaluable assistance. In particular, I thank Dr. W.J.Robertson for his aid in the event processing and Drs. J.Loos and A.T.Goshaw for many helpful discussions.

I wish to express my appreciation to Dr. S.G.Glendinning and Mrs. Mike Bailey for their help in the preparation of this manuscript, and finally I wish to thank my parents for their support during my years of graduate studies.

TABLE OF CONTENTS

LIST OF FIGURES

LIST OF TABLES

Chapter I

INTRODUCTION

Most of the recent advances in strong interaction theory have been focussed on the properties of the quark constituents of hadron matter. No theory, however, has made successful quantitative predictions for strong interactions involving many final state particles. The area of multiparticle production has long been dominated by phenomenologies where simple assumptions about the character of the strong interaction are extrapolated into predictions of the final state particle distributions. Experimental activity in the area concentrated on presenting the large amounts of information obtained in those integrated forms which were thought to best reveal the underlying physics.

In traditional hadron-nucleon interactions only the asymptotic final state particles are available for study. It has been suggested (1,2) that the space-time development of the strong interactions could be probed in hadron-nucleus collisions. If the beam hadron can be assumed to interact successively with several of the nucleons in the nucleus, then collisions occuring after the initial hadron-nucleon collision sample the products of that initial interaction. These subsequent interactions should be reflected in the final state particle distributions.

In this experiment the properties of 200 GeV/c pi-neon interactions are investigated through inclusive study of the final state particles. Comparisons with 200 GeV/c pi-proton and 10.5 GeV/c pi-neon data should yield insights into the time development of the particle production process.

1.1 INCLUSIVE STUDIES OF HADRON - NUCLEON COLLISIONS

The dominant feature of strong inelastic interactions at high energies is the large number of particles in the final state. For center of mass energies ($s^{1/2}$) above 20 GeV resonance production does not seem to account for more than a small fraction of the final state particles. Analysis of specific final states are often inhibited by the experimental difficulty of identifying all final state particles and by combinatorial problems if the final state has more than a few particles. Such difficulties have stimulated interest in studies of the general or average properties of the strong interaction as seen in selected variables (cross section, momenta, etc.) that have been summed over all possible final state configurations.

In the inclusive reaction

$$a + b \longrightarrow c + X$$

incident particle a collides with target b producing final state particle c and anything else. The single particle spectra of c should be useful in revealing the essential nature of the collision and should pose a test for any potential theory for the strong interactions.

The simplest choices for inclusive variables are the total cross section (σ) for the reaction a + b ---> anything and the topological cross section (σ_n) for the reaction

$$a + b \longrightarrow n \text{ charged particles}$$

The total cross section increases logarithmically as s (center of mass energy squared) rises from several hundred $(GeV)^2$ to 2000 $(GeV)^2$. The average charged multiplicity $< n >$ is also seen to increase as ln(s). The (σ_n) distribution broadens with increasing s and the most probable multplicity also shifts to larger values as s increases.

A model free parameterization of the σ_n distribution was developed by Koba, Nielsen and Olson (3). Using Feynman's hypothesis of scaling (4) in the single particle spectra at large s, it was shown that the σ_n distribution was given by

$$\sigma_n(s) = \frac{\sigma_i(s)}{< n >} * \Psi\left(\frac{n}{<n>}\right)$$

for large s. $\sigma_n(s)$ is given by an energy independent function Ψ of the scaled number of particles. Impressive agreement with the KNO law has been found, even at low energies (Figure 1).

The logarithmic energy dependence of $< n >$ is possibly related to another well established feature of high energy interactions; the near energy independence of the transverse momenta (PT) spectra of the final state particles. For PT > 0.2 GeV/c and < 1.0 GeV/c the transverse momentum distribution can be described by a universal function

$$f(p_{||}, PT) = A \exp(-b*PT)$$

with $b \sim 6$ $(GeV/c)^{-1}$. Deviations from this simple behavior exist at large values of PT and in the dependence of b on

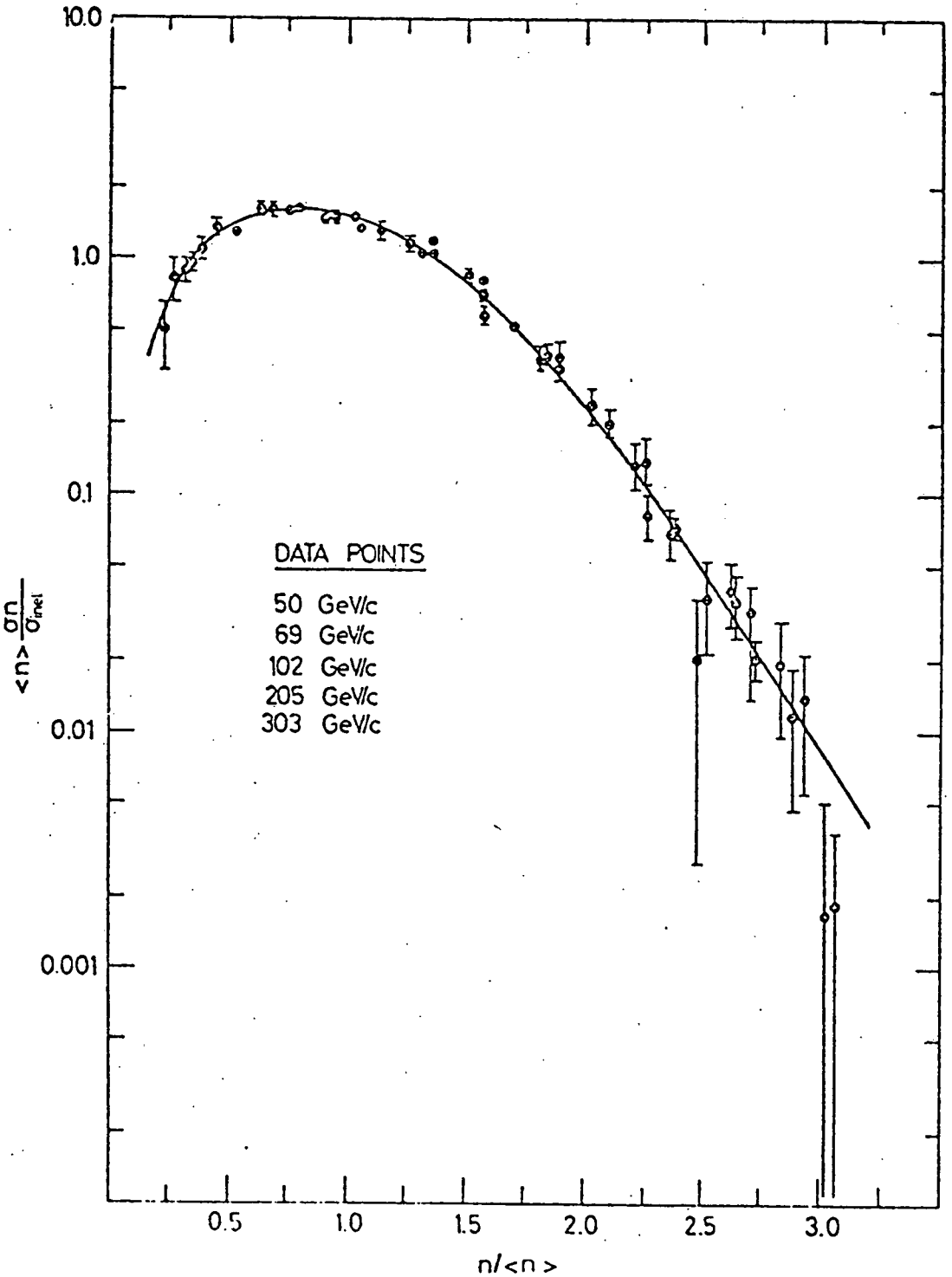

Figure 1: KNO scaling for pp interactions. Data are from reference (5).

the mass of the final state particles. However, as greater than 80% of the final state particles are pions, this PT distribution describes the bulk of the single particle data. If the phase space for particle production does not increase like $s^{1/2}$ as allowed by energy conservation but is restricted to PT damped phase space, then the increase of particle production with s corresponds to the growth of phase space(proportional to ln(s)).

Single particle distributions are used to study the kinematic properties of the final state particles. The Lorentz - invariant differential cross section for particle c is given by

$$f(p,s) = E \frac{d\sigma}{d^3p}$$

where E is the energy of the particle in the rest frame where p was measured. If the beam and target are unpolarized the cross section should only depend on PT and $p_{||}$ (the longitudinal momentum of the particle along the beam momentum). The scaling hypothesis of Feynman (4) was that in some kinematic regions at large s, the cross section would depend on $\vec{p}$ and s only through the variable $x = 2*p_{||}/s^{1/2}$ (Figure 2)

$$f(x,PT^2,s) = \frac{2E}{s^{1/2}} \frac{d\sigma}{dx dPT^2}$$

The Feynman x runs from -1.0 to 1.0 and has traditionally been broken into several kinematic regions where qualita-

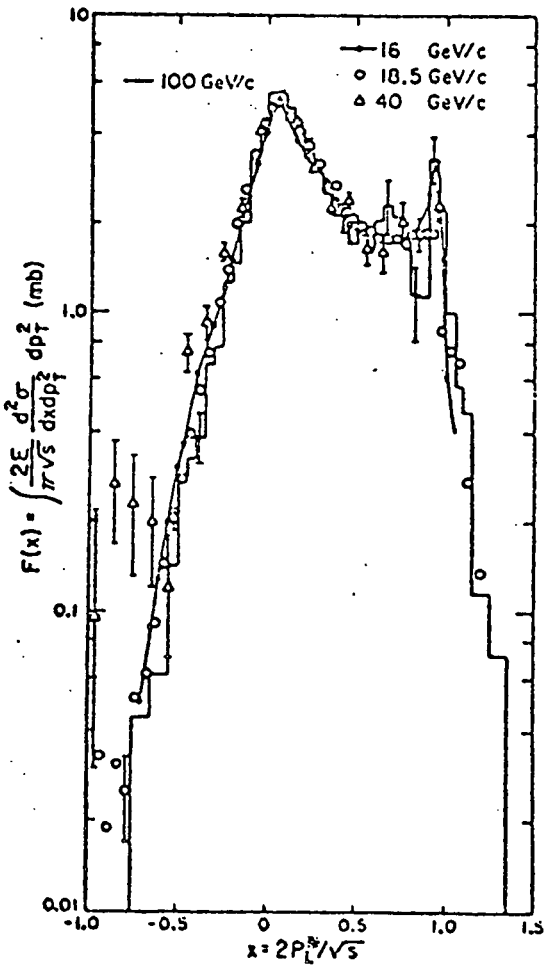

Figure 2: Feynman scaling in x for $\pi^- p$ interactions. Data are from reference (6).

tively different behavior was expected of the final state particles. Cross sections for particles with $x > 0.8$ are very small unless the particle is identical with the beam or target (leading particle). Particles with $x < 0.1$ (pionization region) are slow in the center of mass and should be roughly independent of the beam and target particles. Particles with intermediate x ($0.1 \leq x \leq 0.6$, the fragmentation region) are generally considered related to or fragments of the beam or target particle. Although the energies shown in Figure 2 are still fairly low, approximate scaling in x is seen in most regions.

Another useful kinematic variable is the rapidity

$$y = 1/2 \ln\left(\frac{E + p}{E - p}\right)$$

The invariant cross section can be expressed in terms of PT and y as

$$f(y, PT^2, s) = \frac{1}{\pi} \frac{d\sigma}{dy\,dPT^2}$$

The rapidity of a particle is the boost parameter of the Lorentz transformation to the frame where the longitudinal momentum of the particle is zero. Rapidity distributions retain their shape under Lorentz transformations with the entire distribution being translated by a constant.

Unlike the x variable the length of the rapidity axis grows as ln(s). Particle multiplicity also grows with ln(s)

as previously mentioned. If the increased particle production is confined to the pionization region, a central plateau will develop in the rapidity spectrum at high energies. The maximum value at the center of the plateau will be energy independent (2 particles per unit rapidity), but the width of the distribution will grow as ln(s). This parameterization is quite close to the behavior observed in Figure 3.

A popular variant of the rapidity used by emulsion and counter experiments in which the momentum is unmeasured is the pseudo - rapidity

$$\eta = -\ln(\tan(\theta/2))$$

where θ is the angle between the beam and the outgoing track. η is a good approximation of y when PT and mass are small.

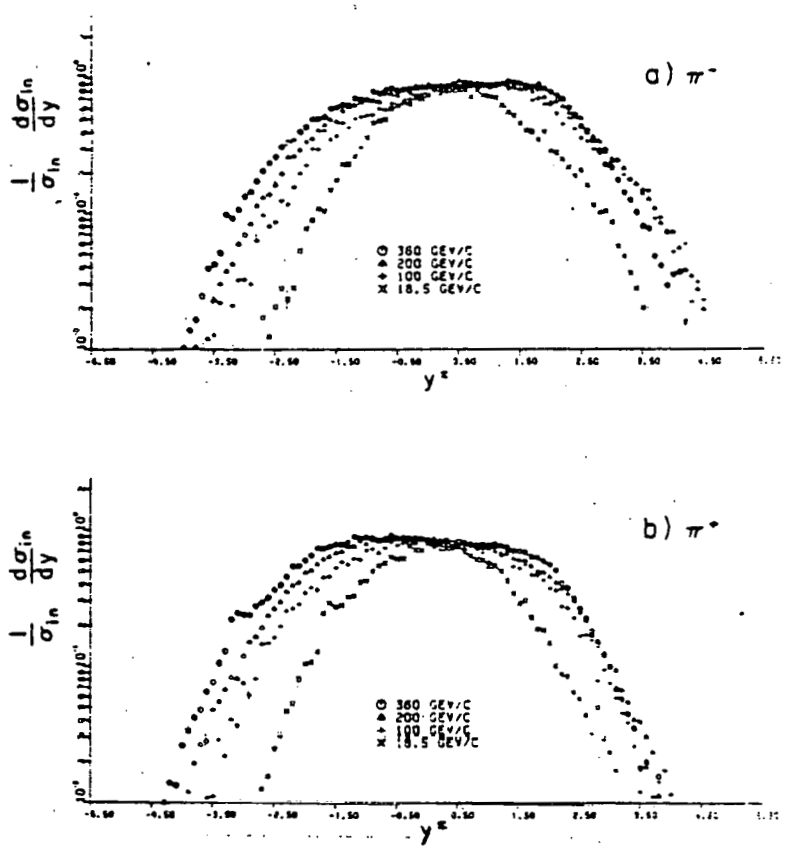

Figure 3: Rapidity plots for pi^-p interactions.
a. pi^- final state
b. pi^+ final state
Data are from reference (6).

1.2 HADRON - NUCLEUS COLLISIONS

The total cross section for hadron nucleus collisions is predicted remarkably well by the Glauber multiple scattering model using the hadron - nucleon cross section and a Wood - Saxon nuclear density as input(8).

$$\sigma_i = 28.5\ A^{.75}$$

The closeness of the exponent to 2/3 (0.69 in p - nucleus collisions) indicates that the nucleus represents an almost totally absorptive target to the incoming hadron.

If the beam hadron retained its identity and continued through the nucleus after the initial interaction it would undergo an average $\bar{\nu}$ collisions with nucleons inside the nucleus.

$$\bar{\nu} = A\sigma(h\text{-}p)/\sigma(h\text{-}A) \quad = \quad 1.56 \quad \text{neon}$$

Thus the parameter $\bar{\nu}$ is a measure of the thickness of the nuclear target as seen by the beam hadron.

The most surprising feature of hadron - nuclei interactions is the slow growth of the average multiplicity with A (atomic mass). Naive expectations of large cascades due to the outgoing particles are unsupported. If we consider the initial collision as forming a resonance of lifetime τ, then the resonance decays outside the nucleus if $\gamma\tau\ c > d$ (the nuclear diameter). The hadronic state produced by the initial interaction is thus expected to behave approximately as a single particle in traversing the rest of the nucleus.

A useful measure of the average multiplicity of a hadron - nucleus collision is

$$R(A) = \frac{< n > \text{ hadron - nucleus}}{< n > \text{ hadron - nucleon}}$$

$< n >$ is the average multiplicity of fast charged tracks ($\beta > 0.7$) with elastic and diffractive events removed. R(A) is a slowly growing function of A (Figure 4) reaching a maximum of about 2 for lead. When viewed as a function of $\bar{\nu}$

$$R(A) = 1/2 + 1/2\ \bar{\nu}$$

R is seen to be insensitive to energy or particle type.

Emulsion and counter chamber experiments have established that the bulk of the multiplicity increase occurs in the target fragmentation region. Studies of pseudo - rapidity data show that the particle density in the target fragmentation region grows slowly with increasing A(see Figure 5). Conversely the highest pseudo-rapidity values show little or no target dependence(11).

The number of nucleons ejected from the nucleus can be large, reaching 1/2 A for light nuclei. A correlation between the number of protons observed and the average multiplicity of the event has been well documented by emulsion and bubble chamber work (11,12). Suggestions that the number of observed protons is intimately related to the effective target mass is an integral part of several theories (13,14,15,9). Support for is seen in the positive correla-

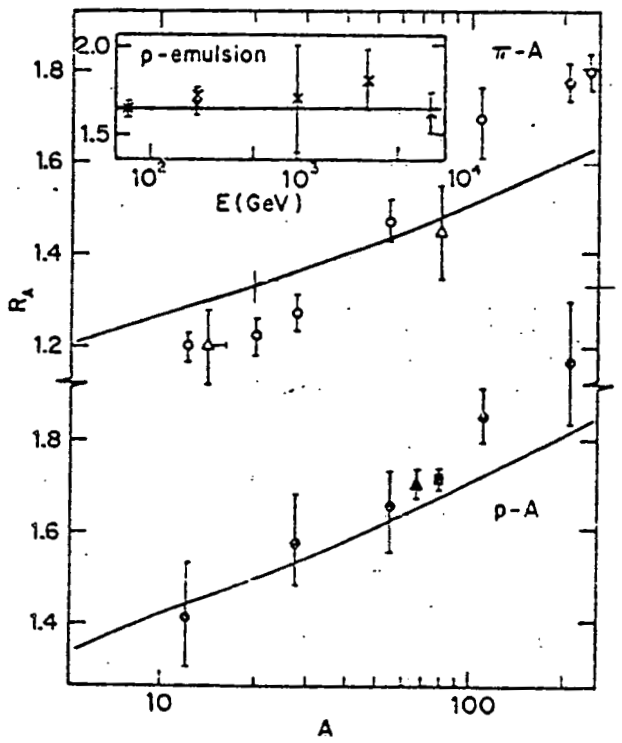

Figure 4: R(A) for p nucleus and pi nucleus interactions. Insert shows energy dependence of R(A) found in emulsion experiments A~60. Data are from reference (8).
See text (page 12) for details.

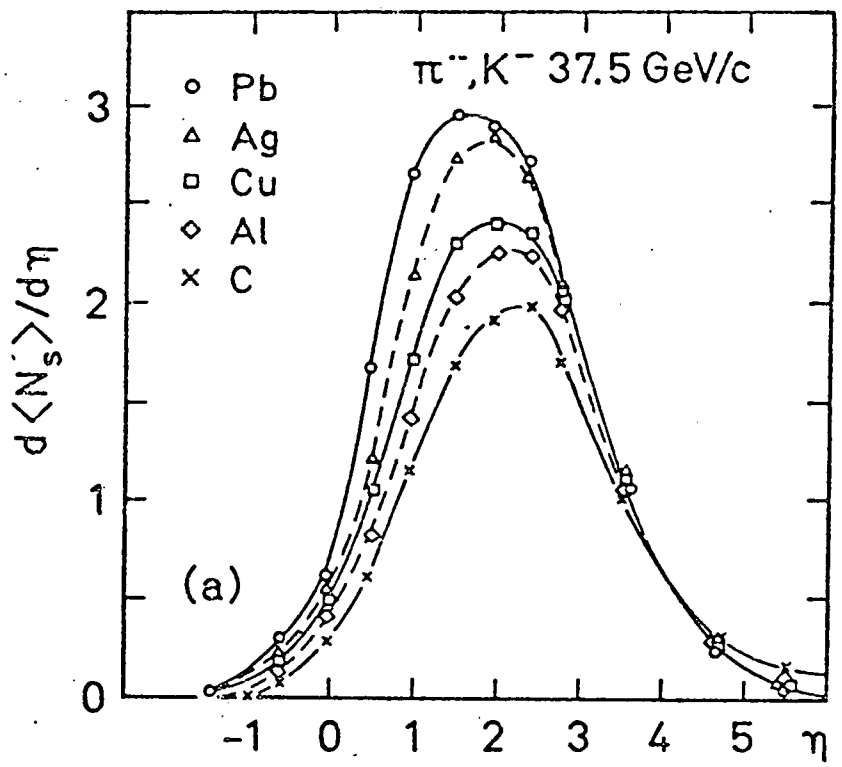

Figure 5: Pseudo-rapidity for different targets at 37.5 GeV/c. Data are from reference (9).

tion between <n> and NP and in the corresponding shift in the center of the rapidity distributions towards small y as NP increases (see Figure 6).

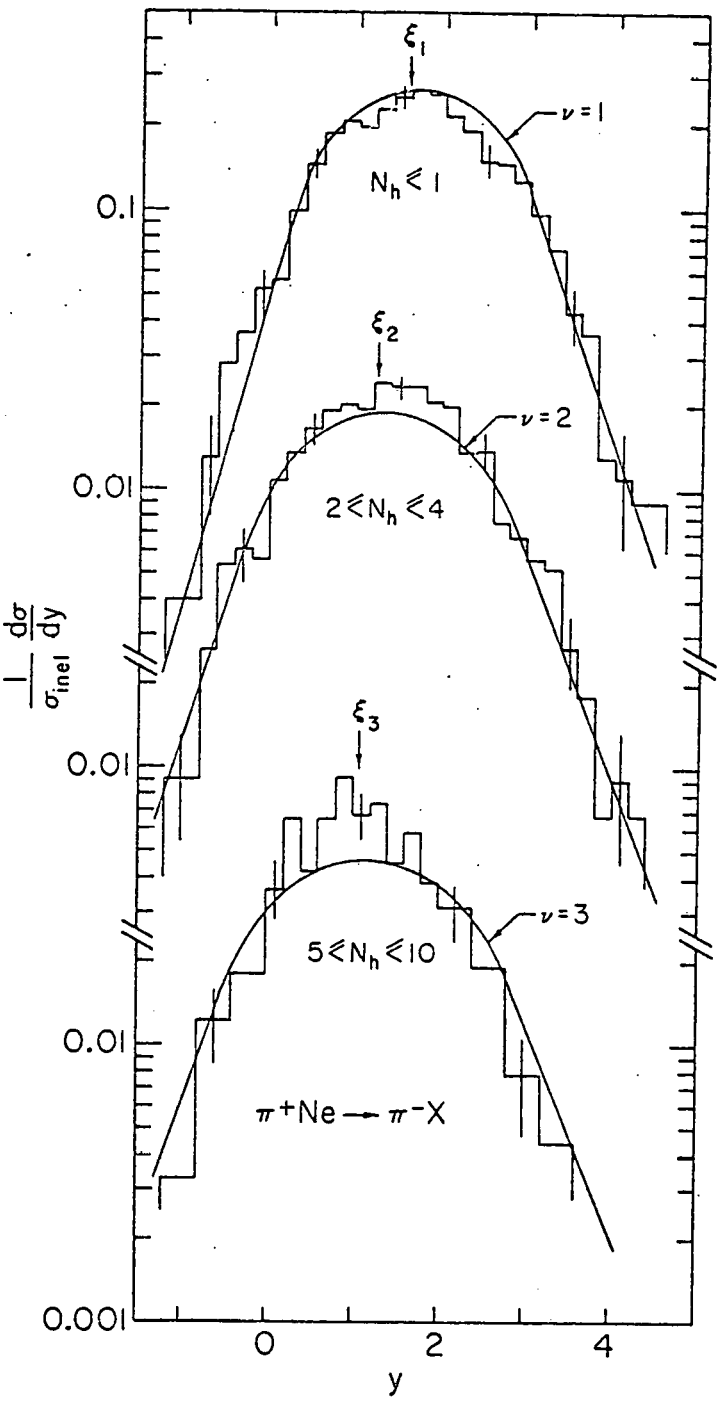

Figure 6: Rapidity distributions vs. NP. Combined pi± rapidity distributions for 10.5 GeV/c pi⁻neon events with NP=0,1; NP=2,3,4; and NP 5.0 events. $\xi_{1,2,3}$ is the respective center of mass. Curves are fits to the data using tube model of reference (13).

1.3 MODELS

Numerous phencmenological models have been proposed as descriptions of hadron - nucleus interactions. Constrained by the weak A dependent rise in the average multiplicity, all of the models provide mechanisms for the suppression of intra - nuclear cascades. The models vary widely in their approach to the problem. A short description of some representative models follows.

The Coherent Tube Model (CTM) has gained many adherents (13,14) since its original introduction (15,9). If the interaction time between two hadrons is long enough, then the beam hadron will collide with all of the nucleons in its flight path simultaneously. The effective target in a beam nucleus collision is then the i nucleons inside a tube of cross section σ centered along the beam line of flight.

Assuming that the tube behaves like a single heavy nucleon (mass i* proton mass), s is given by

$$s(i) = 2\ i\ m_p\ E(\text{beam})$$

The interaction is assumed equivalent to a beam - nucleon collision with s = s(i). The number of nucleons inside the tube varies with the impact parameter of the beam. The average hadron - nucleus collision is thus represented by an average over all impact parameters (equivalently all possible tube sizes).

Since the beam - tube collision is equivalent to a higher energy beam - hadron collision some predictions of the CTM are:

1. KNO scaling of σ_n in energy.

2. The same KNO scaling function as beam - hadron collisions.

3. A strong relation between the number of observed protons and $< n >$

$$R\ (NP) = (A/Z)\ NP^{1/4}$$

Several variations of the CTM (13,14) differ from the above by restricting the arguments and predictions to kinematic regions outside the beam fragmentation region.

In the Gottfried Energy Flux Cascade model (1) it is assumed the products of a hadron - nucleon collision are best described by collective variables for times immediately after the collision. Using relativistic hydrodynamics as a guide the subsequent reinteraction properties of this collective state are predicted. Viewed in the rest frame of the nucleus the product of an initial hadron - nucleon collision is an excited hadronic state initially confined to a thin disc. The energy flux of the matter inside the disc is approximated by the asymptotic rapidity distribution of hadron - nucleon collisions. The different energy components in the disc disperse in time forming a cylinder along

the beam direction. The large rapidity components form the leading edge of the cylinder, with lower rapidity components trailing. The central assumption of the model is that whenever a slice of the cylinder has the same thickness as a hadron of corresponding rapidity, then that slice interacts as a single hadron.

If the nucleons in the nucleus are thought of as forming a linear array of separation λ, the second nucleon is hit by several slices of the energy flux. For beam energies around 200 GeV only two slices (corresponding to two particles) interact with the second nucleon. The first particle has the equivalent of the full beam energy E. The second particle has energy $(E)^{1/3}$ (1). The low energy slice gives rise to only a slight amount of cascading, because of its low energy. Subsequent interaction of the energy flux with a third nucleon would be equivalent to the interaction of a hadron of energy E and two hadrons of energy $E^{1/3}$.

The Energy Flux Model predicts that the excess particle production due to the nuclear target will be confined to rapidities smaller than the rapidity of the center of mass. The model predicts an energy independent value of R

$$R(\bar{\nu}) = 1 + 0.38(\bar{\nu} - 1)$$

$$= 1.21 \qquad \text{(neon } \bar{\nu} = 1.55\text{)}$$

A third model (16) is based on "wee parton" interactions (17). Each nucleon in the nucleus and the beam hadron are considered to have independent parton distributions. The wee partons of the beam interact with the wee partons of the nucleons. Each nucleon interacts at most once with the beam, while the beam undergoes an average of $\bar{\nu}$ collisions per hadron - nucleus interaction. The center of mass y_i of each parton - parton collision is distributed uniformly in the central region. The partons of the beam materialize into hadrons with $y > y_i$ and the nucleon partons materialize with $y < y_i$. The beam fragmentations are spread out in rapidity from the beam rapidity to the smallest y_i with uniform density. Specific predictions of this model are (16)

$R(y) = \bar{\nu}$ Target fragmentation region

$R(y) = 1$ Beam fragmentation region

$R(y) = \bar{\nu}(1 - y/Y_c) + [1 - (1 - y/Y_c)^{\bar{\nu}}]$ Central region

where Y_c is the length of the central rapidity region. For collisions at 200 GeV/c the predicted R averaged over all regions is

$$R = \bar{\nu}/2 + \bar{\nu}/(\bar{\nu} + 1) - 0.2\,(\bar{\nu} - 1)/(\bar{\nu} + 1)$$

$$= 1.34 \quad \text{neon}$$

Chapter II

EXPERIMENTAL PROCEDURE

A 50,000 picture exposure of 200 GeV pi- incident on the Fermilab 30 inch bubble chamber was taken in June, 1974. The chamber was filled with a hydrogen - neon mixture (31 ± 1 molar % neon) at a density of 0.255 gm/cc. The beam of unseparated negative particles was produced by collisions of 303 GeV/c protons on a target 1 kilometer upstream of the bubble chamber. The beam was momentum selected with an average value of 200.0±0.2 GeV/c. An earlier experiment in the same beam line(18) found the beam to be predominantly pi- with 2.6% mu- and 1.4% K- contamination.

The film was scanned for pi- interactions on either hydrogen or neon. The charged track multiplicity, observed neutral conversion multiplicity and other characteristics of the events were recorded. About 50% of the interactions found in the initial scan were chosen for measurement. Three passes were necessary to measure 90% of these events. The track measuring efficiency was 92%. The measurements were processed through suitably altered versions of MATCH and TVGP(19). Event weights were constructed to normalize the measured multiplicity distribution to the scanned distribution. Track weights were assigned to correct for mea-

suring inefficiencies and biases. A final event weight was applied to complete the separation of events into hydrogenic and neonic categories.

2.1 SCANNING

Scanning for this experiment was done in several passes over the film. The initial scan located the interactions of interest. Subsequent passes studied the events in more detail or examined various backgrounds. Three views of each frame were taken; however, for scanning purposes, only views 1 and 2 were used. The photographs were projected on the scan table in 1.4 lifesize magnification. The optics of the table were sufficiently distortion free to permit acceptable scan table template measurement of tracks which were not adequately measured on the digitizer.

MULTIPLICITY SCAN: Found interactions, recorded charged and neutral multiplicity.

EDIT SCAN: Recorded neutral vertex position and number of positive, negative, and straight tracks.

99 SCAN: Estimated multiplicity of events with very close secondary interactions.

MEASUREMENT EDIT SCAN: Selected events for measurement. Events with confusing secondary interactions or nearby beam tracks were not chosen.

SPECIAL SCANS: Double checked scanning efficiency for gammas on low multiplicity events. Found events with pions of less than 200 MeV/c lab momentum.

REMEASUREMENT EDIT SCAN: Prepared drawings of events for use by the measurers. A close reexamination of the events was done at the same time with particular attention on locating gammas converting near the vertex.

2.1.1 Multiplicity scan

Only a small percentage of the photographs contained useful events. The exposure was untriggered so many frames had only noninteracting beam tracks. Other frames were spoiled by upstream interactions which flooded the chamber with secondary tracks. Even frames with interactions were not always used as a minimum track length was needed for both the beam track and the outgoing tracks. To satisfy these criteria a beam interaction region was defined. Only frames with a single interaction in this region were used.

The interaction region is shown in Figure 7. A frame was discarded if there were any off angle tracks entering the front of the chamber. Frames were also discarded if beam tracks passed outside of the interaction region or if an interaction occured upstream of the region. After these exclusions approximately 29,000 frames remained. These good frames were then inspected for single hadronic events in the interaction region. Events of electromagnetic origin (delta rays or direct pairs) were not intentionally included and were removed in later check scans. For each event the following information was recorded:

1. Grid(X and Y) of the primary vertex
2. Number of identified protons(NP)
3. Number of minimum ionizing tracks(NMIN). In practice minimum tracks included all charged tracks except identified protons and electrons.

4. Number of minimum tracks inside a forward $\pm$ 2° cone (NFF)

5. Number of pions with momentum <150 MeV/c (NSP)

6. Number of associated gammas (NG)

7. Number of associated V°'s (K^0 and Λ) (NV)

There was a small sample of events for which an exact count of the number of minimum tracks was unreliable. For these events NMIN=99 was recorded.

2.1.2 Edit scan

After the intial pass scanners reexamined the events in greater detail. In addition to checking the previously recorded information several other characteristics of the events where recorded. The number of positive and negative minimum tracks were counted. If a track had no perceptible curvature it was recorded as a straight track. If the event had only one proton its angle relative to the beam and track length were recorded in two views. Also, the grid locations of the gammas and V°'s were recorded in two views. Several flags were also used to indicate conditions in the frame which might cause difficulty during measurement. They were:

1. B any beam track close to the interacting beam

2. D Dalitz pair (not counted in NMIN)

3. L gamma conversion with vertex obscured by other tracks.

4. T a secondary track interacted within a 10 cm radius of the primary vertex

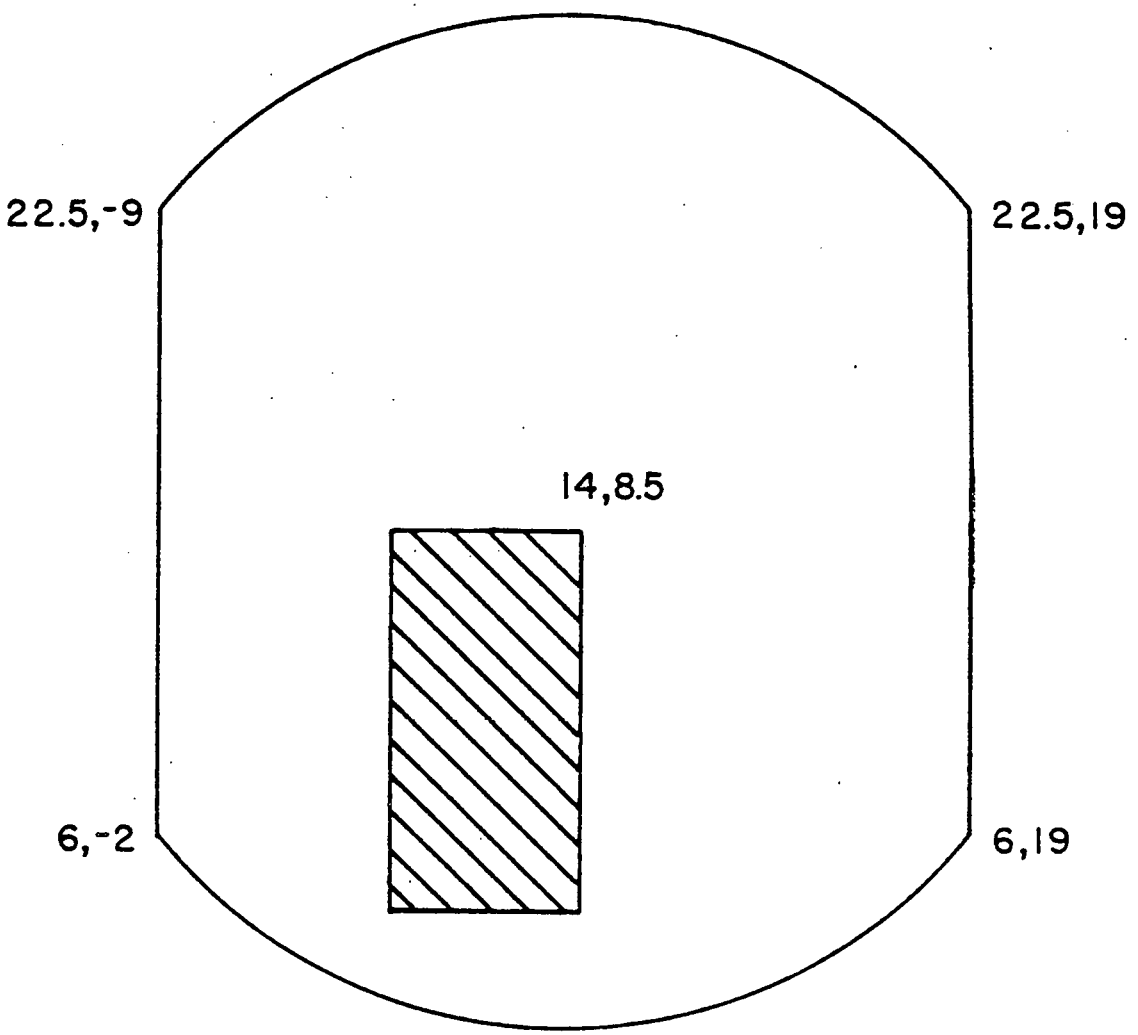

Figure 7: Beam interaction region as seen in view 2. Scan grid coordinates (1 inch in space) for the center and edges of the chamber are also shown.

5. X a secondary track interacted beyond 10 cm but inside a forward ± 2° cone

2.1.3 99 scan

As described earlier, scanners recorded NMIN=99 for an event if they were unable to determine the exact number of minimum ionizing tracks. Such events invariably resulted from the secondary collision of an outgoing track making it impossible to separate the tracks produced by the secondary interaction from those of the primary interaction. In order to determine the characteristics of the 99 type events a special scan was performed to estimate their multiplicities. The distribution found is in Table 1.

TABLE 1

SCAN EVENT POPULATION

NMIN	0-2	3-5	6-10	11-15	16-20	>20
99 TYPE	0	33	93	86	38	23
SCAN	464	1053	1799	1094	417	172
Weight	1.0	1.03	1.05	1.08	1.09	1.13

Events with NMIN≠99 (labeled SCAN) are also found in Table 1. To correct for the loss of the 99 events in scanned and measured distributions a weight as a function of

multiplicity was constructed (WT99) and applied to the remaining events. WT99 for a certain multiplicity range was given by:

$$WT99 = (SCAN + 99TYPE) / SCAN$$

The weighted NMIN scan distribution is shown in Figure 8.

2.1.4 Measurement edit scan

The next step in the scanning sequence was the preparation of a list of events to be measured. The large number of secondary interactions caused by the hydrogen-neon mix often made accurate measurements of the other non-interacting tracks in that event impossible. Also secondary interactions produce neutral particles that are often unresolvable from neutrals produced by the primary vertex. To avoid these complicating factors all events with secondary interactions within a keyhole template(a 10cm circle plus a 30cm cone $\pm 2^{0}$) were not measured. Events with beam tracks very close to the interacting beam track were also not measured. These cuts restricted the number of events on which measurements were attempted to about 2700.

2.1.5 Special scans

Two scans in addition to the normal scanning-measuring sequence were performed. Both scans measured crudely on the scan table quantities that later would be measured with greater precision on the measuring machine. A slow pi scan

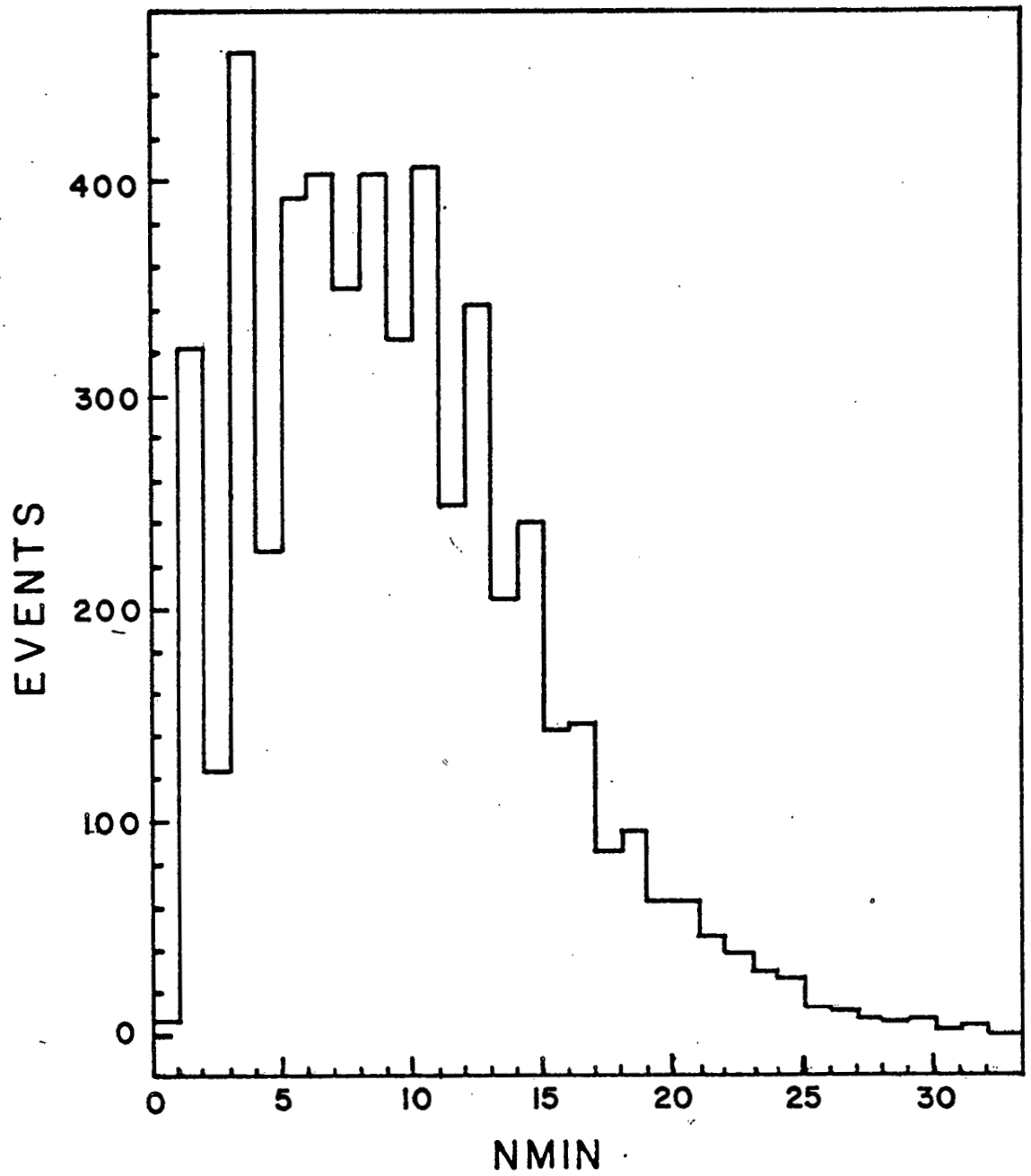

Figure 8: Weighted NMIN distribution. See text (pages 28 and 29) for definition of NMIN.

measured the angle and momentum of pi's of less than 200 MeV/c in the lab. A gamma rescan of events with less than seven NMIN tracks was also carried out. The scans provided information for the preliminary analysis of the data, but were later superceded by the measured results. Both scans provided useful consistency checks for scanning and measuring efficiencies.

2.1.6 Remeasurement edit scan

An examination of the events initially measured at SUNY showed that a sizable fraction of the measured NMIN tracks were positrons and electrons. These electron-positron pairs could only be the products of unrecognized gamma conversions. An estimate of the number of such unseen pairs was made using the scan grid information and the gamma conversion length (Appendix A) averaged over energy (<E> = 3000 MeV/c). Figure 9 shows the distribution in the number of conversions observed at a radius r from the primary vertex. The estimated true distribution (normalized to the number of conversions between r = 10 and r = 20 cm) is also shown. The loss of gammas far from the primary vertex is the effect of the finite chamber size. The difference between the observed and expected number of conversions is large (750 gammas) for r less than 10 cm from the primary vertex. Approximately 15% of the scanned events had unrecognized gamma conversions.

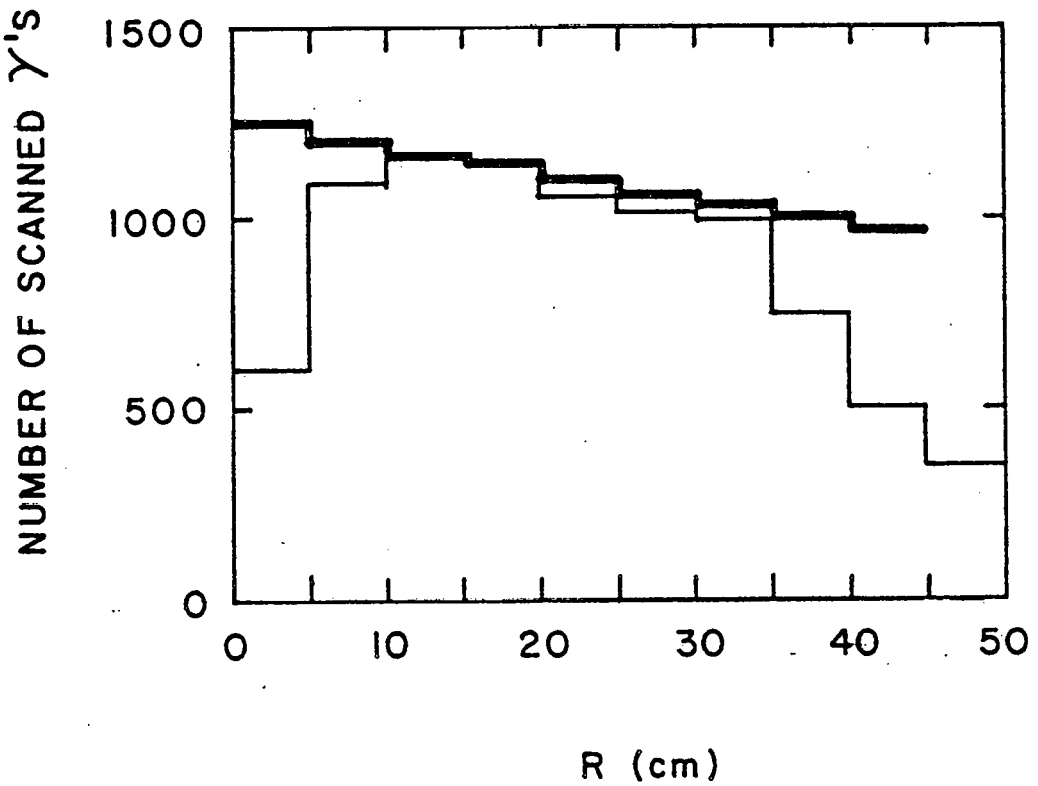

Figure 9: Gamma conversion lengths. The heavy curve represents the expected number of gamma conversions. See text (page 31) for details.

TABLE 2

UNSEEN GAMMAS

NMIN	EVENTS	GAMMAS NOT SEEN	% OF EVENTS
<4	914	22	2.4
4-7	1321	194	14.7
8-11	1312	234	17.8
12-15	863	206	23.8
16-20	417	84	20.1
>20	172	48	27.9

Since the unrecognized conversions produce pairs which are counted in the NMIN, a correction to the NMIN distribution was necessary. An estimate of the number of unseen gammas for events grouped according to multiplicity is shown in Table 2. A strong correlation between the probability for an unseen pair and the multiplicity of the event is apparent. The NMIN distribution was then corrected as shown in Figure 10.

Although the above procedure corrected the NMIN distributions summed over all events, it was not useful in detecting gammas in specific events. To gain the maximum information on each event a rescan for gammas was carried out in conjunction with preparation of a remeasurement list. Electrons

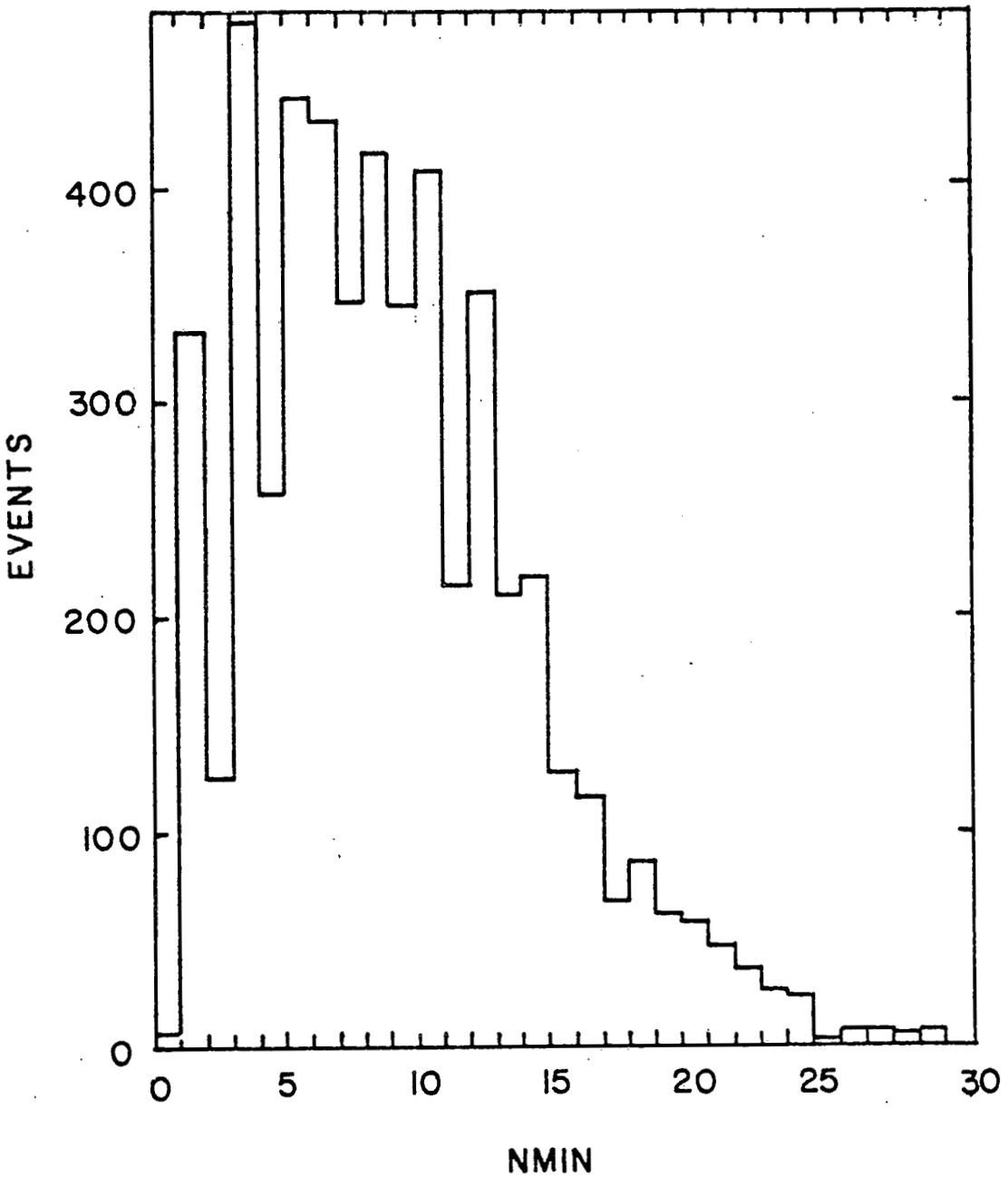

Figure 10: Corrected NMIN distribution.

and positrons have a high probability for suffering high energy losses due to bremsstrahlung radiation. If the energy loss is large enough a change in the curvature of the electron is noticable on the scan table. Closer examination of events by physicists found many gammas that were not seen by scanners in the original scans. Not all gammas were found in this rescan as described in Appendix D, but the percentage of events with unseen gammas was reduced to 7%.

2.2 MEASURING

The measuring of high momentum tracks in small bubble chambers poses a severe test to the entire measuring process. In addition to the inherent imprecision of the measuring machine, measuring errors are introduced by the difficulty of separating tracks lying close together. At 200 GeV/c the forward hemisphere of the center of mass lies in a 5° cone about the beam direction in the lab. Thus the probability for having many tracks in this region is high. Also, many neutral particles convert in this forward area. Even if a track is clearly visible in its entire length momentum measurements are limited in accuracy by purely geometric considerations. A 50 GeV/c track in a 25 Kilogauss field has a radius of curvature of 6500 cm. The deviation of such a track from a straight line is 480 microns in 50 cm of track length. Since the measuring precision of the machines averages between 100 and 300 microns the measuring error is > 25% at this energy. Additional measurement errors were caused by turbulence in the chamber. This turbulence was small and was significant for only the fastest tracks for which it could cause a systematic underestimation of momentum.

Three measuring passes measured about 90% of the events on the measurement list. The initial measuring pass attempted to measure all neutral particles and all charged tracks outside a forward $\pm 2°$ cone. Poor track selection by

the measurers resulted in a substantial number of e+ ,e- and protons being included in the minimum track sample. A second measuring pass was necessary to eliminate incorrectly measured tracks and to measure any tracks missed in the original pass. This second measuring pass was done on one of the scan tables. Although the measuring precision of this technique was limited it was accurate to within 10% in rapidity and momentum for the kinematic regions of greatest interest. A third and final measuring pass measured all the events that were poorly measured in the first two passes. As these events were in general of complicated topology several special procedures were applied to insure proper track identification by the measurers.

As an example of the difficulties faced in the measuring process a photograph of one of the events is shown in Figure 11. The event is of moderate multiplicity(NMIN=13, NP=2), but with a large number of gammas (7). Two of the gamma conversions are less than 10 cm from the primary vertex and could be easily mistaken for minimum tracks. Several bremsstrahlung gammas must be separated from gammas originating at the primary vertex. A nearby beam track must not be confused with the minimum tracks downstream. Finally the two protons must be recognized and treated separately from the minimum tracks.

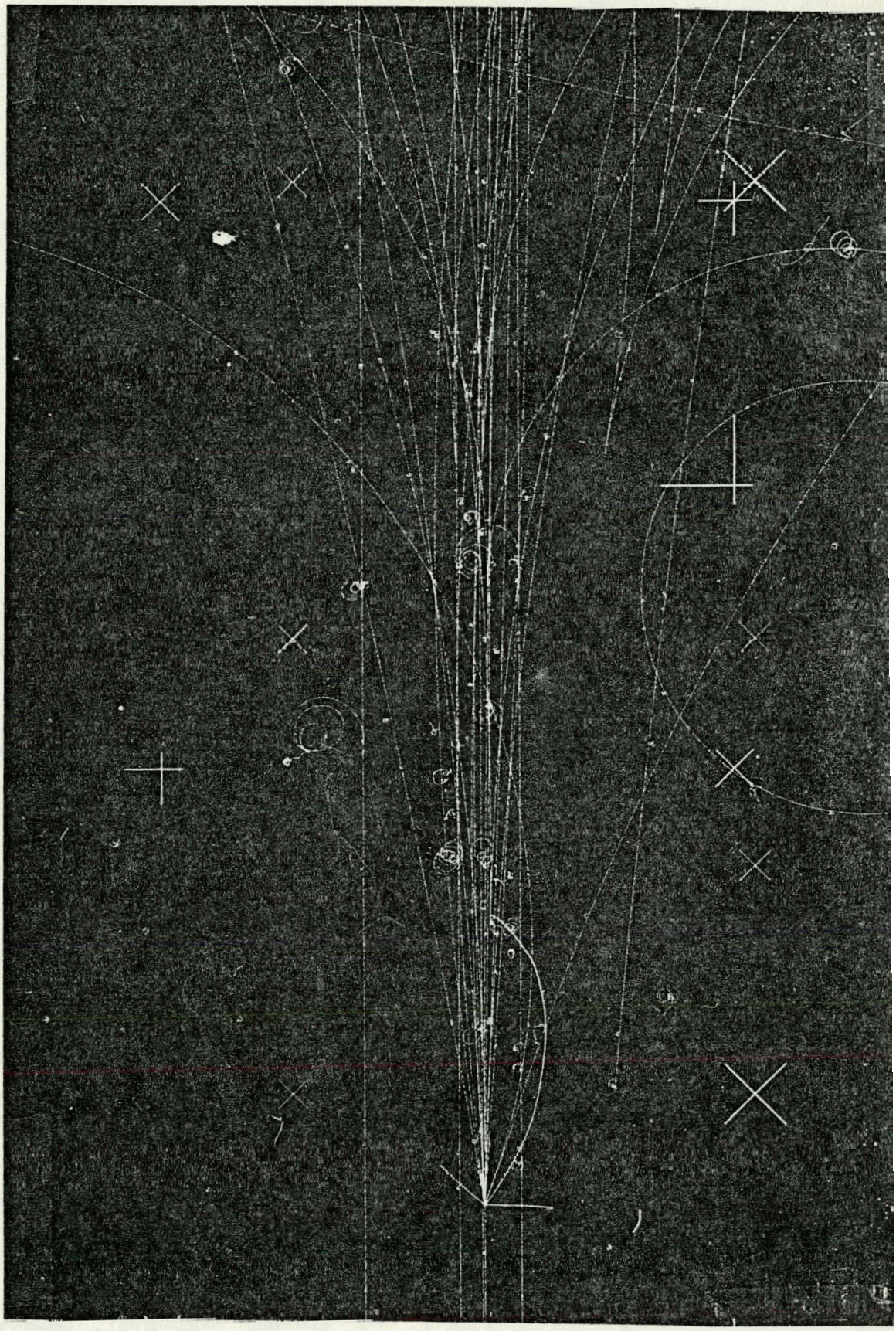

Figure 11: Typical event.

2.2.1 SUNY measurements

The initial measuring pass was done at the State University of New York at Albany(SUNY). The film was measured on a mangia-spago device which had a point setting error of 15 microns on film. The measurers attempted to measure only those tracks which lay outside a 2° cone about the beam direction. Neutral vertices were also measured at this time. The SUNY measurements were processed through MATCH and TVGP computer programs to reconstruct the tracks' momenta. The FRMS (chisquared deviation of the measured points from the reconstructed track) is a measure of the accuracy of the track measurement. The maximum allowed FRMS was 40. The FRMS of the SUNY measurements
is shown in Figure 12 a.

2.2.2 Scan table measurements

The measuring efficiency for the SUNY events was reduced by several effects. Tracks often would lie in the cone only in one view and consequently would not be measured in that view. Reconstruction would fail if a view was missed. As mentioned earlier gammas were often hard to separate from the outgoing charged tracks and many were mistakenly included in the charged track sample. To correct these deficiencies a remeasurement pass at Duke measured all tracks not correctly measured at SUNY, checked carefully for extra-

neous tracks, and measured all tracks in the forward 2° cone. These measurements were carried out on one of the scan tables. This table had 1.04 lifesize projection and was almost distortion free(<.5%). The measuring technique consisted of aligning a template with the beam direction at the vertex thereby fixing the vertical axis of the template. At 10 cm intervals on the vertical axis the offset of the track from the vertical axis was recorded. The typical measurement precision was 1mm on the table or approximately 50 microns on film. The measurers visually matched the tracks in all three views using delta rays, bubble gaps and curvature to identify tracks. The measurements were recorded on cards and processed through TVGP. The FRMS of these tracks is shown in Figure 12 b.

Clearly the relatively large point setting error of the scan table measurements implies that momentum measurements of high momentum tracks are imprecise. For tracks of less than 6 GeV/c lab momentum this method is accurate to 10%. The error in rapidity is also less than 10% for tracks with lab rapidities less than four. These measurents are thus of adequate precision in the kinematic regions of most importance.

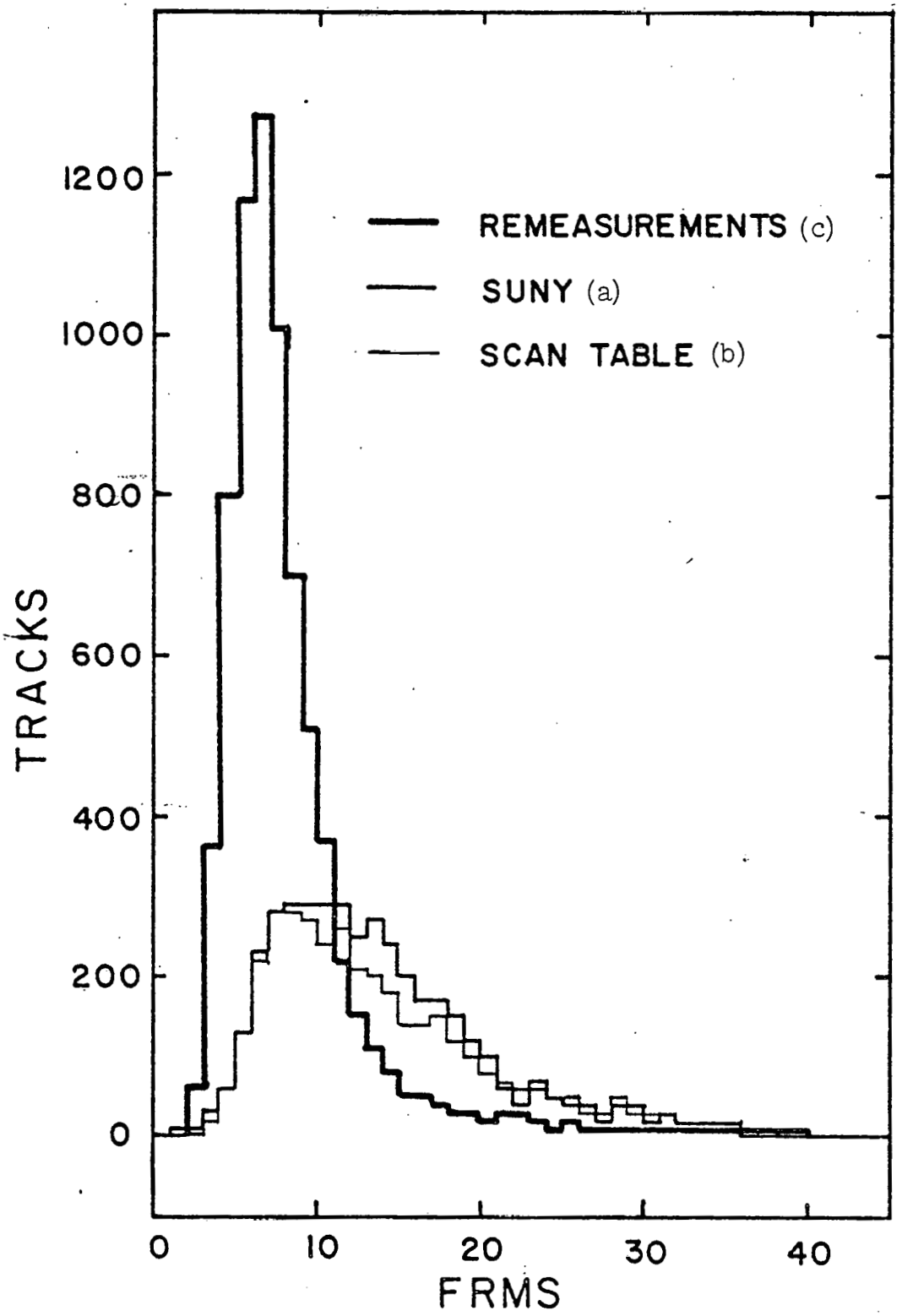

Figure 12: FRMS of charged tracks.

2.2.3 Duke remeasurements

The SUNY and scan table measuring passes successfully measured 60% of the events. The failure rate for events with a large number of minimum tracks or gammas was high. The measured event sample was thus seriously biased towards low multiplicity events. To correct these biases and to increase statistics a third measuring pass was carried out at Duke.

The remeasurement pass was done on the Duke semi-automatic measuring machine (RIPPLE) which has been described elsewhere(20). Several modifications to the normal RIPPLE measuring procedure were necessary because of the complex nature of these events. The automatic track recognition procedure was unable to resolve large numbers of tracks. Tracks were set up by operators manually. RIPPLE used this information to parameterize the track's curvature and then measured other points on the track unassisted.

Only a single view of an event was available to the measurer via the TV monitor at any given time. This often provided insufficient information for the measurer to properly set up the tracks. Many possible areas of confusion were caused by multiple overlapping tracks or gamma conversions. Detailed drawings of each event in views 1 and 2 were prepared with all minimum tracks and protons identified as well as all secondary vertices. Kinks or secondary interactions on the charged tracks were also noted as well as any

situation which could cause the measurer confusion. With these steps the remeasurements were highly successful and approximately 90% of the events were measured. The FRMS distribution of the charged tracks is found in Figure 12 c.

2.2.4 Neutral particle measurements

The accurate measurement of neutral particles requires the momentum measurement of the charged decay or interaction products (e-e+, pi+pi-, or ppi-) as well as the space angle between the secondary vertex and the main interaction vertex. The vertex measurement poses no problems if the vertex is visible in all three views. The momentum measurement is often limited in accuracy by the short track length of the charged products.

Two factors limit the charged track length. Tracks converting near the edge of the conversion volume are very close to the chamber wall and are thus visible for only several centimeters. Other short tracks are caused by interactions of one of the tracks in the chamber liquid. This effect is small for hadrons, but electrons have a large probability for a bremsstrahlung collision. The probability per cm for an electron of energy 2000 MeV/c to emit a gamma in a bremsstrahlung interaction is plotted in Figure 13 as a function of the gamma energy. Large bremsstrahlung losses are identifiable on the scan table and the track measurement is then limited to the initial portion of track.

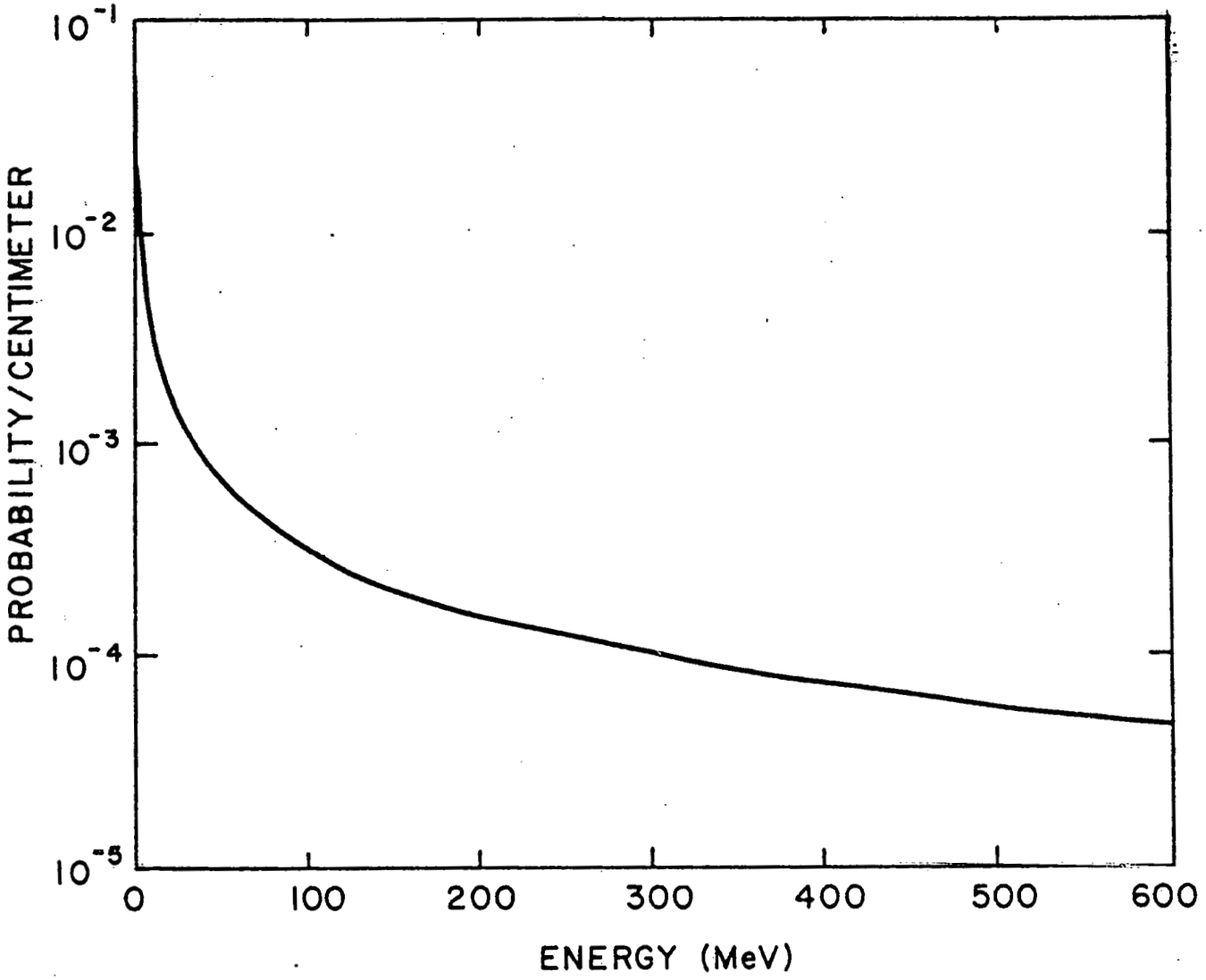

Figure 13: Probability per cm for bremsstrahlung collisions.

A more serious problem with the electrons is caused by the large number of small bremsstrahlung losses. Since no gross change of curvature is measurable the reconstruction programs fit a single curve to the entire measured track. The electron momentum is thus systematically underestimated. A correction procedure due to Elliott(21) was applied in TVGP which optimised the electron track length and increased the measured energy by about 15%.

The net effect of the restrictions on track length was that certain classes of neutrals could at best be measured only approximately. Therefore full energy measurements were attempted only on those neutrals with sufficient track length for an accurate momentum measurement. The remaining neutrals were measured only as secondary vertices. The partially unmeasurable gammas were those with one or both charged tracks having a track length of less than 10 cm. Others were gammas converting in the forward 2^{0} cone whose charged tracks were faster than 3 GeV/c as measured crudely on the scan table. The gamma momentum measurements are thus only valid for gammas in the range of 50 to 3000 MeV/c.

2.3 WEIGHTS

Given the complexity of these events it is not surprising that a number of tracks or events remained unmeasured after the three measuring passes. Continued measuring was impractical. A weight was assigned to each event and track to compensate for the unmeasured events. The weighted inclusive distributions approximate the true distributions that would have been obtained if all tracks and events had been measured.

If the scanning and measuring processes were unbiased then the weights would be the the reciprocal of the overall measuring and scanning efficiency. Often, however, the measuring process discriminates against events with certain characteristics(high multiplicity for example). The weight then is necessarily a function of the event or track's properties. Much effort was devoted to the study of measurement biases and the construction of weights that properly correct those biases.

The events in this experiment are either pi- proton (hydrogen) or pi- neon. Although many events are readily identified as neon, a large class of events are separable into hydrogenic and neonic groups by statistical methods only. This separation is accomplished by a weight which is a function of the number of minimum tracks and the number of protons. It is discussed later in this section. A helpful

aspect of the dual targets in this experiment is that the pi- p interaction has been measured previously by this group and others(18) in hydrogen bubble chambers. The hydrogen single particle distributions obtained in this experiment can be normalized to those results to study the scanning and measuring efficiencies. Assuming that the hydrogen and neon tracks are treated equally by the measuring process the track weights found for the hydrogen events can be applied to the neon events. A flow chart of the weighting schemes can be found in Figure 14.

2.3.1 Event weights

As described earlier only 50% of the events were selected for measurement. Of these about 90% had more than three-fourths of their tracks successfully measured. The combined effect of the scanning and measuring biases was a discrimination against events with large NMIN. Table 3 shows the scan event population. Table 4 shows the event population of the events on the measurement list(ML). Each event in the measurement list with NMIN (minimum ionizing tracks) and NP (protons) carried a weight given by:

$$W(NP,NMIN) = \frac{\text{Number scan events with NP and NMIN}}{\text{Number ML events with NP and NMIN}}$$

All events with NMIN greater than 20 minimum tracks were grouped together for better statistics.

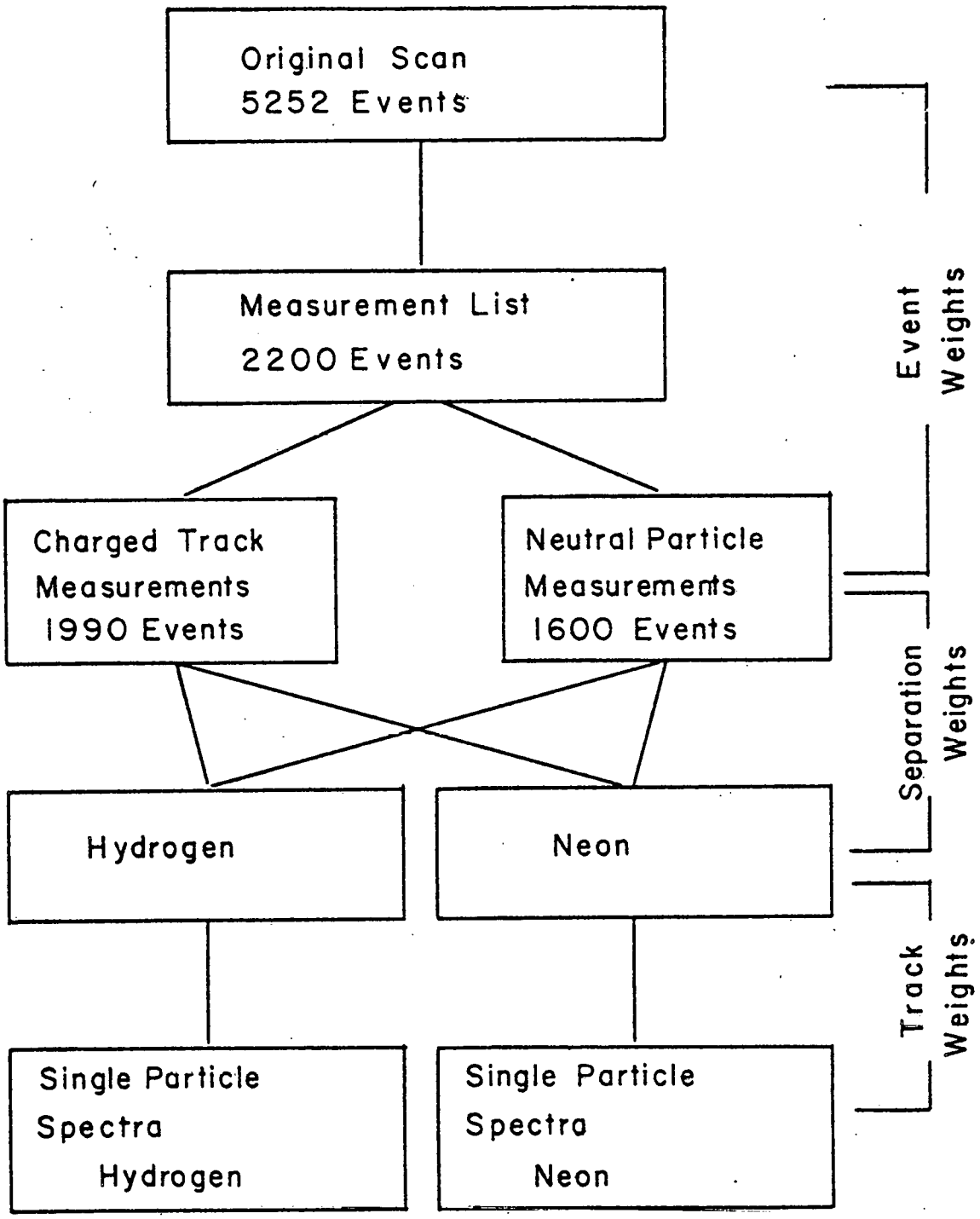

Figure 14: Weight flow chart.

A complication of this scheme is that the NMIN and NP of the events were sometimes altered during the rescan. The weights had to be remapped into functions of the new scan variables. The WT99 weight was also included at this time. The final weights for the events on the measurement list are shown in Table 5.

Since only 90% of the events on the measurement list were measured, an additional weight was needed to correct for this loss. The event weights for events with charged track measurements were constructed exactly as described in the previous paragraph.

TABLE 3

RAW SCAN EVENTS

NMIN	NP=0	NP=1	NP≥2
0	2	3	1
1	8	284	29
2	68	24	32
3	225	167	56
4	140	38	42
5	128	161	93
6	222	64	99
7	111	111	111
8	216	61	107
9	84	105	121
10	219	54	114
11	67	58	106
12	165	62	90
13	36	51	103
14	97	46	81
15	34	21	77
16	53	19	62
17	7	18	54
18	29	11	48
19	13	14	31
20	12	10	36
21	4	6	31
22	5	5	24
23	3	3	21
24	3	6	15
25	2	0	6
26	1	0	10
27	1	1	5
28	1	1	4
29	1	2	4
30	0	0	2
31	0	0	4
32	0	0	0
33	0	0	1

TABLE 4

MEASUREMENT LIST EVENTS

NMIM	NP=0	NP=1	NP≥2
0	0	1	1
1	6	198	21
2	44	19	20
3	136	100	30
4	83	21	25
5	87	80	49
6	118	33	49
7	57	57	56
8	105	28	62
9	45	50	52
10	97	29	48
11	33	24	39
12	64	23	33
13	14	13	28
14	36	18	23
15	12	7	25
16	19	10	21
17	3	5	21
18	8	5	16
19	2	7	11
20	4	1	13
21	1	1	10
22	1	4	4
>23	1	3	11

TABLE 5

EVENT WEIGHTS

NMIN	NP=0	NP=1	NP≥2
0	0.00	3.00	1.00
1	1.38	1.47	1.42
2	1.68	1.32	1.62
3	1.66	1.70	1.85
4	1.70	1.79	1.73
5	1.48	2.01	1.89
6	1.88	1.92	2.01
7	1.94	1.96	1.96
8	2.06	2.18	1.79
9	1.90	2.10	2.31
10	2.27	1.94	2.41
11	2.10	2.55	2.78
12	2.56	2.73	2.83
13	2.55	3.79	3.53
14	2.70	2.50	3.32
15	2.82	3.12	3.07
16	2.82	1.93	2.89
17	3.69	3.83	2.69
18	3.38	2.40	2.94
19	6.50	2.00	3.45
20	3.00	0.0	3.11
21	3.00	5.00	3.82
22	7.00	3.00	5.03
>23	0.0	3.0	7.30

2.3.2 Hydrogen-neon separation

The events in this experiment are due to pi- interactions with a proton (hydrogen) or with a neon nucleus. In many cases the scan information will identify the neon events. However some neon interactions are very similar to hydrogen interactions and can be separated from the later only by statistical means.

Since charge is conserved, all pi- proton interactions have an even number of charged tracks with a net charge of zero. Hydrogen events have no more than one visible proton. The angle the proton makes with the beam direction also must be compatible with momentum conservation. The neon interaction can occur on a single peripheral proton or neutron or with several nucleons at once. The net charge of the neon events ranges from -1 to +9, neglecting any second order processes. The number of protons and their production angles vary widely depending on the extent of the nuclear breakup during the interaction.

The events were divided into hydrogenic and neonic categories. The hydrogenic events had all the scan characteristics of pi- p collisions. The neonic events were those events which could only have occured on neon. The NMIN distribution of the hydrogenic events is shown in Figure 15. In

Appendix B the number of expected hydrogen events is calculated. Using the well measured hydrogen multiplicity distribution (Table 9) the predicted number of hydrogen events as a function of NMIN and NP was calculated(Figure 15). The excess hydrogenic events are attributed to misclassified neon interactions.

The hydrogenic neon interactions are thought to come mainly from collisions with a peripheral proton. Since such a proton is only loosely bound (on this energy scale) it is assumed that these events are completely similar in all details to pi- hydrogen interactions of the same multiplicity. By comparing the number of weighted hydrogenic events to the expected number of hydrogen events of a given NMIN and NP, a probability can be assigned for each event to be on hydrogen or neon. Each hydrogenic event is added to the hydrogen group with the total event weight being multiplied by the probability that the event is on hydrogen. The remaining hydrogenic events are added to the neon sample.

The validity of this separation can be checked by comparing the single particle distributions of this experiment with those of previous experiments on hydrogen(18,22). No significant differences between the data are exhibited (Figure 16 and 17).

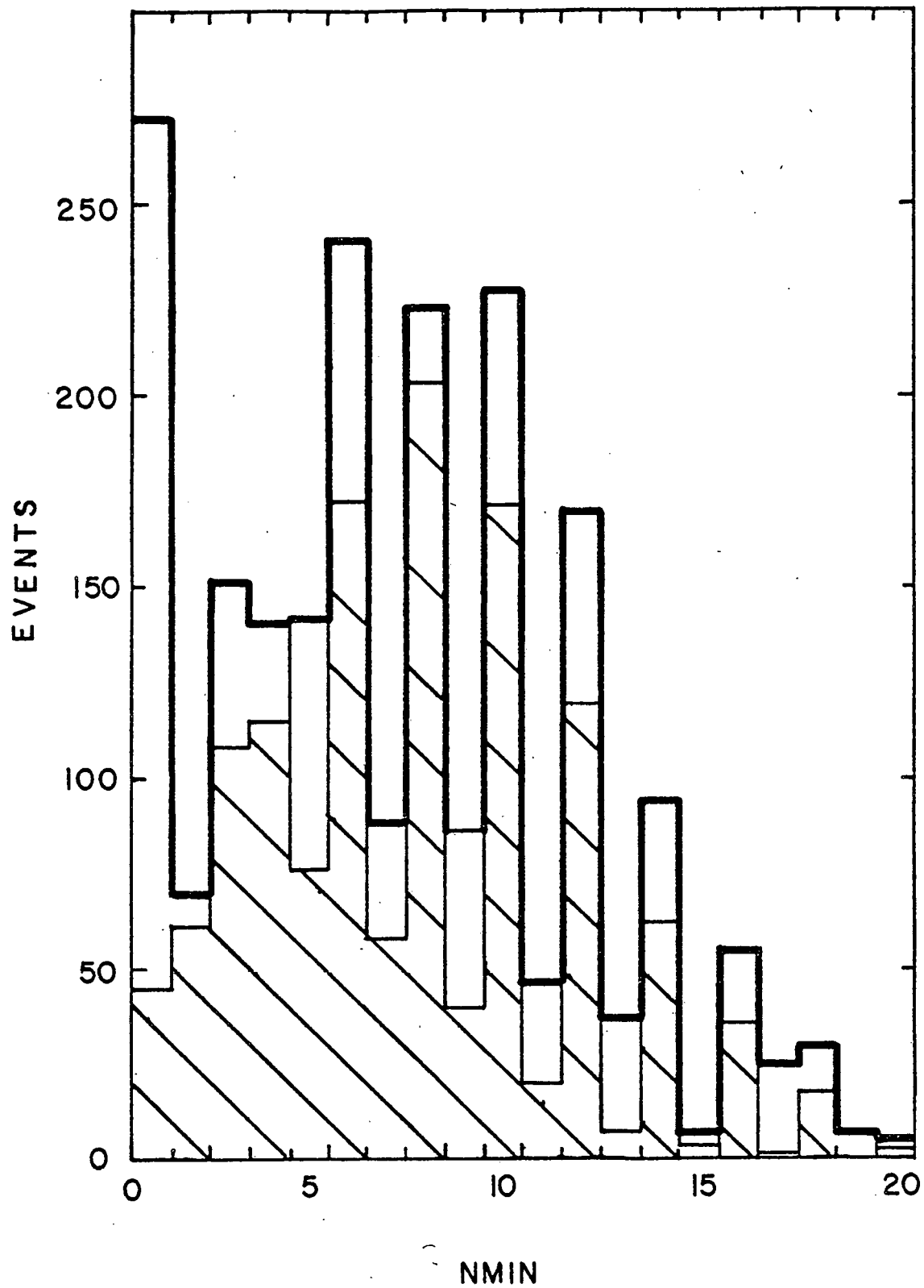

Figure 15: Hydrogen and hydrogenic multiplicity distributions.

2.3.3 Charged track weights

The track measuring efficiency for events having more than three quarters of their tracks measured was 92%. The event weights for this restricted sample were calculated as discussed previously. In addition a track weight for each measured track was necessary to correct for the unmeasured tracks. A comparison of the pi+ and pi- rapidity (y) distributions of this experiment with those found in hydrogen bubble chamber experiments at the same energy (Figure 16 and 17), show that the unmeasured tracks are predominantly fast. This loss of high rapidity tracks is also caused by measurement errors which tend to decrease the measured value of rapidity of high rapidity tracks. Below y=4.5 the rapidity distributions are consistent with an unbiased track excess of 2%. This value is consistent with the expected e+ e- contamination of the minimum tracks. By normalizing the rapidity spectrum to that of previous experiments a track weight which is a function of y is constructed for the hydrogenic events.

In principal the track measuring efficiencies for hydrogenic and neonic events should be equal as no attempt at separation was made until after the measuring process. The track measuring efficiency, however, decreases as NMIN increases. Consequently, the track measuring efficiency was lower for neonic events. Even for events with the same NMIN, however, the neonic events had a lower measuring effi-

ciency. This can be attributed to the generally higher complexity of the neonic events. The rapidity dependent track weights found in the hydrogenic events were modified for the slightly greater bias against low energy tracks found in the neon events. This weight was then multiplied by a constant to correct for the lower measuring efficiency for the neonic tracks.

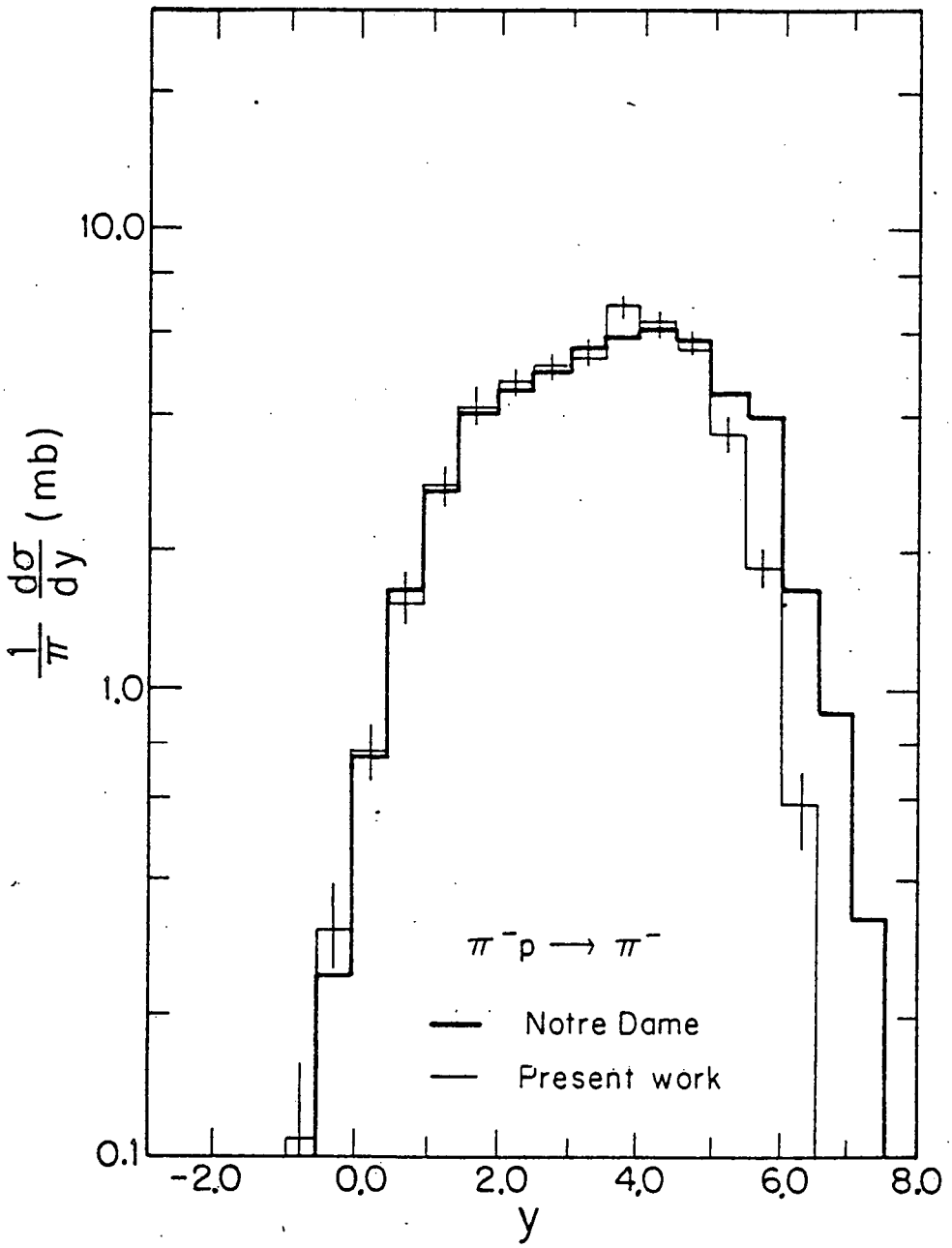

Figure 16: Pi- rapidity distribution of hydrogen events.

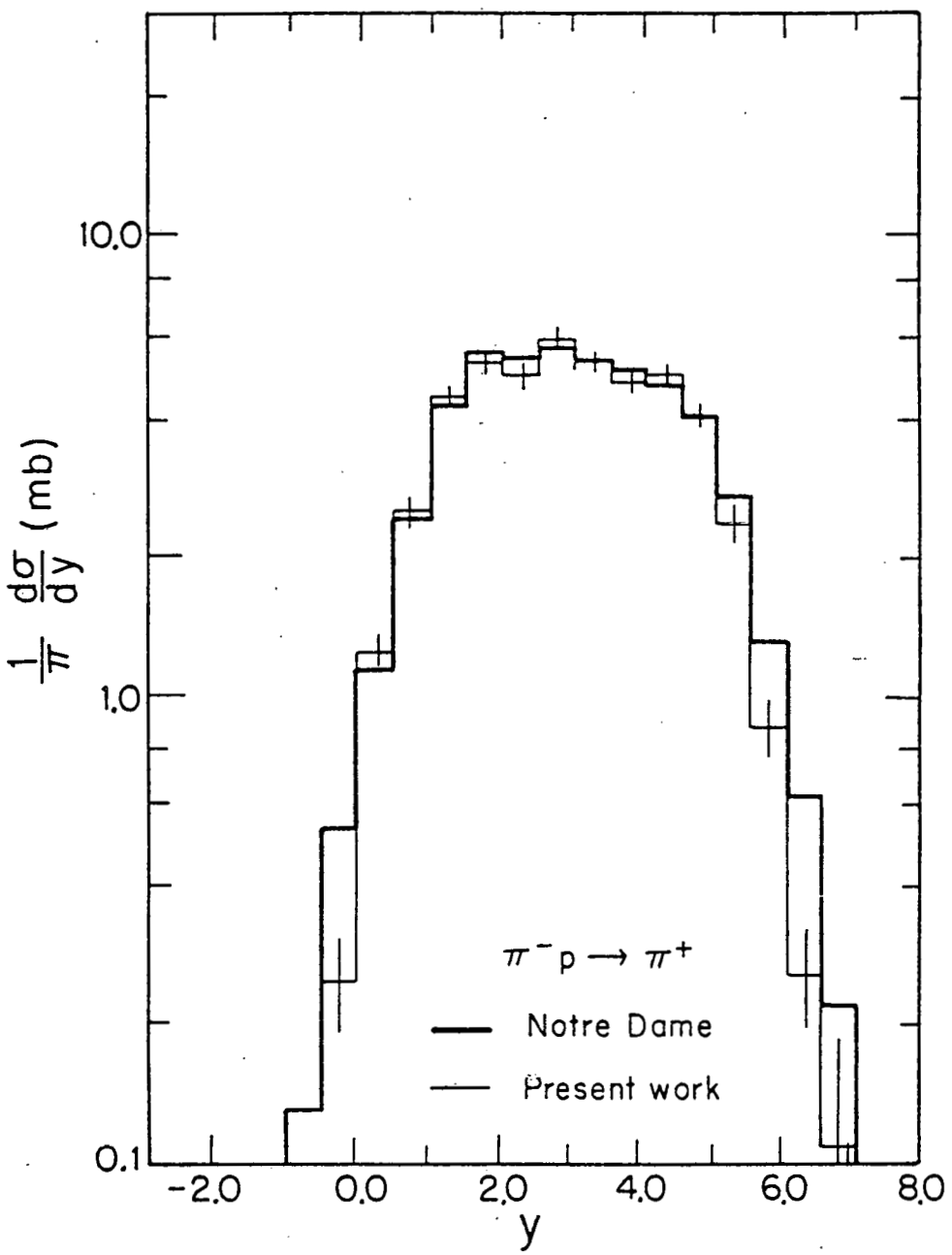

Figure 17: Pi^+ rapidity distribution of hydrogen events.

2.3.4 Neutral particle weights

Only charged particles are directly visible in the bubble chamber. Neutral particles are seen only through decays or interact within the bubble chamber which produce charged tracks. Several neutral particles which are of interest in this experiment are

$$\pi \longrightarrow \gamma\gamma$$

$$K^{\circ} \longrightarrow \pi\pi$$

$$\Lambda \longrightarrow p\,\pi$$

As only a fraction of the neutral particles are observed in the bubble chamber a weight is assigned to each particle seen so that the inclusive distributions are properly normalized. The probability of a neutral decay or interaction can be calculated. The weight is then the inverse of the probability.

The probability is a function of several particle dependent quantities and of the potential path length in the bubble chamber. The path length is determined by the position of the primary vertex and the production angle of the neutral particle. A computer subroutine (RAY) was written to calculate the potential length from the vertex to the surface of a geometric fiducial region. This surface, depicted in Figure 18, consists of a cylinder aligned along the Z

axis intersecting with planes of constant X and Y. The exact location of the surfaces could be varied to study the effects of fiducial volume changes on scanning efficiency. The values displayed in Figure 18 were the final set used for this experiment.

As discussed in Appendix A the interaction length (IL) for gammas was calculated for each gamma energy. Only pair conversions were scanned and measured in this experiment. The probability of a gamma converting to a pair between two points S1 and S2 is

$$p = \frac{\sigma(\text{pair})}{\sigma(\text{total})} * (\exp(-S1/IL) - \exp(-S2/IL))$$

The conversion weight is then 1.0/p.

Conversion weights for strange particles were calculated similarly with the interaction length IL being replaced by the mean decay length DL of that strange particle. Further discussion of the strange particle weights can be found in Appendix C.

In addition to the conversion weights, a weight must be applied to the measured neutrals to correct for the neutral particles lost in the measuring process. The neutral particle detection and measuring efficiency is discussed in Appendix D. It is shown that inside the conversion region the detection efficiency is unbiased.

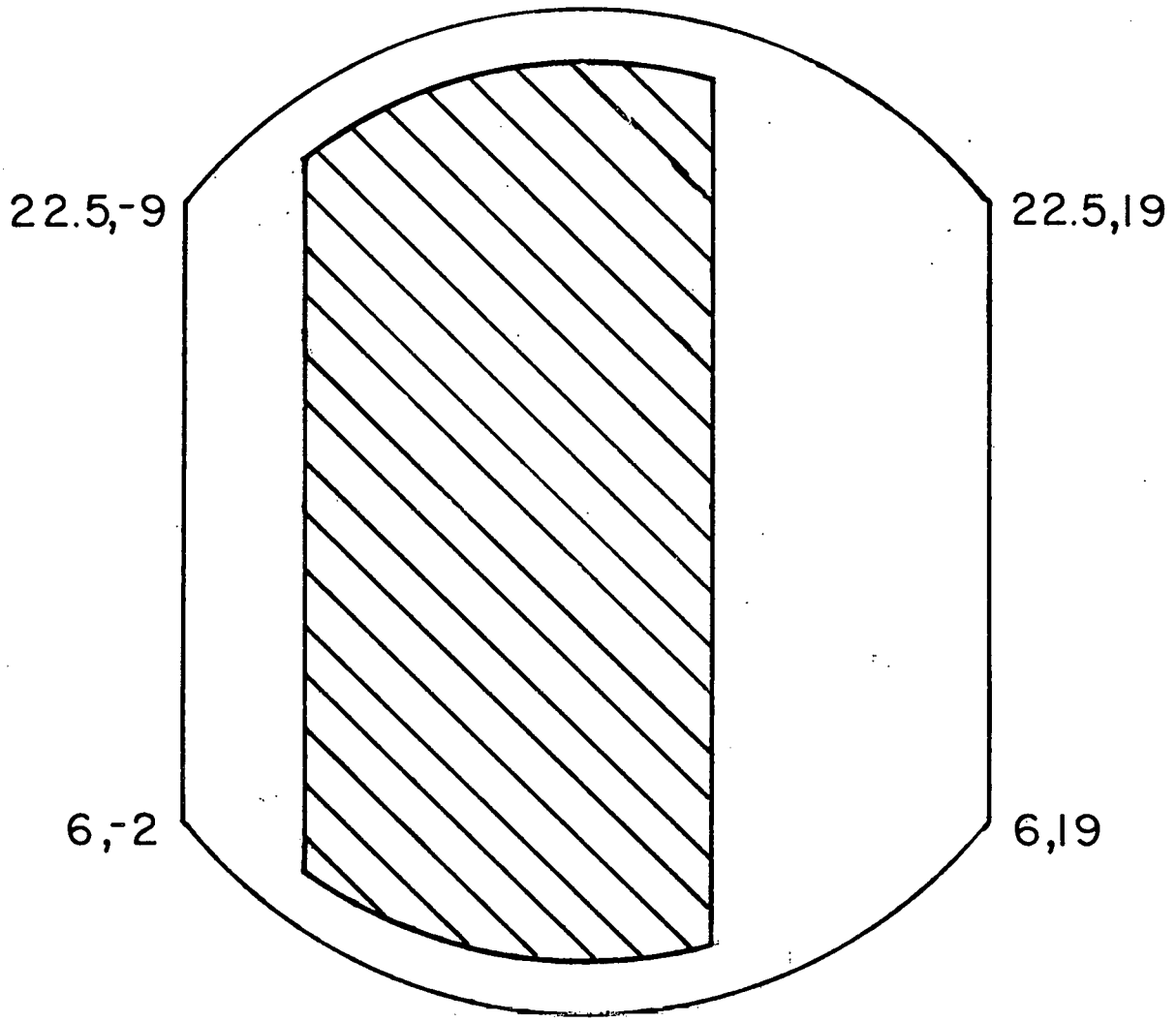

Figure 18: Gamma conversion region. Only gammas converting in this region and further than 10 cm from the vertex were used in data analysis.

Chapter III

DATA ANALYSIS

From the original scan and edited scan NMIN distributions the neon NMIN distribution is extracted. Average charged track and neutral particle multiplicities are calculated with corrections for unrecognised gamma conversions and minimum ionizing protons. σ_n is found to obey KNO scaling when compared to 10.5 GeV/c pi-neon and 200 GeV/c pi-p data. Comparisons of the average pion multiplicity in neon to hydrogen data are made through the variable R and compared to similar studies at 10.5 GeV/c. Correlations between the average pion multiplicity <pi> and the number of scanned protons are investigated.

Weighted gamma data are used to estimate the average pi^0 multiplicity $<pi^0>$ as a function of NMIN. Correlations between $<pi^0>$ and the number of scanned protons are also examined and correspond well to correlations seen among the charged pions. Other pi^0 moments are found and compared to hydrogen data. The gamma rapidity distribution of neon events is compared to that of hydrogen. Production characteristics of the pi^0 are investigated through Monte Carlo simulations of pi^+ and pi^- decays to gammas.

Structure functions for the charged tracks are plotted. PT^2 distributions of pions from neon interactions are similar to equivalent distributions from hydrogen. The increase in average particle multiplicity due to the neon target is seen to occur in the target fragmentation and central pionization regions. Dependence of the pion structure functions on the proton multiplicity are investigated. Energy dependence of the $p_{||}$ and y distributions are studied by comparison with 10.5 GeV/c data.

3.1 MULTIPLICITIES

3.1.1 Charged Pions

After the edited NMIN distribution had been properly weighted, estimates of non-pion components of the minimum ionizing tracks were made. The $K^{\pm}$ contamination had been estimated at 4% (12) and was ignored. As mentioned previously gammas converting close to the primary vertex were sometimes included in the NMIN count. In Appendix D the procedure for estimating the number of gamma conversions $\leq$ 10 cm from the primary vertex is discussed. When the predicted and observed number of gammas are compared for each NMIN, the estimated number of unseen gammas can be calculated. Assuming that at most one gamma is unseen per event, each unseen gamma is associated with an event of true multiplicity NMIN - 2. An iterative subtraction starting at low multiplicity corrected the NMIN distribution for these unseen gammas.

The expected hydrogen events were subtracted from the corrected scan sample. Scan multiplicities from 200 GeV/c pi- p data (18,22) were used after modification for the lower proton scanning efficiency of this experiment. The NMIN distribution is shown in Figure 19. The most prominent feature of the data is the diffractive peaks at NMIN = 3, 5, or 7.

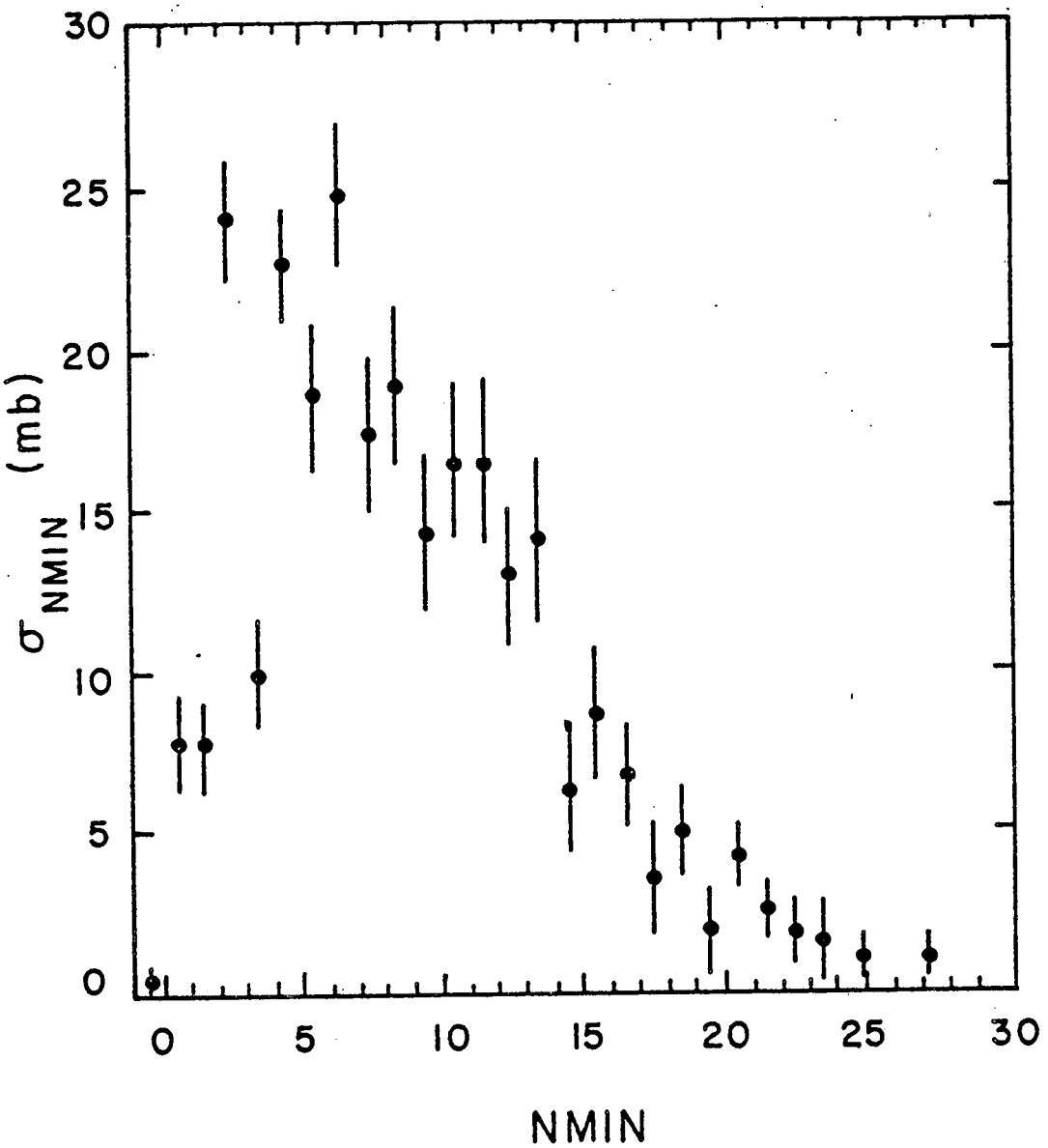

Figure 19: Neon topological cross sections.

The neon NMIN data still contains a substantial number of minimum ionizing protons. In Appendix E the estimated number of such fast protons is calculated. These minimum ionizing protons are likely associated with higher multiplicity events, however, no procedure for estimating the number of fast protons as a function of NMIN was found reliable. The fast protons constitute a 5% contamination of the minimun tracks in Figure 19.

Table 6 contains the average number of minimum ionizing tracks per event with the estimated number of proton tracks. The average number of pi$^{\pm}$ was found for all neon events and for all non-diffractive neon events. The ratio R defined previously as:

$$R = \frac{\langle pi^{\pm} \rangle \text{ pi- neon}}{\langle pi^{\pm} \rangle \text{ pi- proton}}$$

was calculated for each sample of neon events.

Also printed in Table 6 are the corresponding multiplicities for pi- neon at 10.5 GeV/c (12). Although the average multiplicity more than doubles between the two energies, R shows no significant change. R is approximately the same for event samples including or excluding the diffractive events at 200 GeV/c. Conversely R at 10.5 GeV/c increases if the diffractive events are removed from the sample.

For comparison the values of R predicted by several models are listed below.

TABLE 6

AVERAGE CHARGED TRACK MULTIPLICITY

Pi- neon	200.0 GeV/c	10.5 GeV/c
<minimum tracks>	9.41± 0.21	3.91± 0.03
<scan protons>	1.77± 0.10	1.50± 0.08
<fast protons>	0.44± 0.14	0.46± 0.12
<protons>	2.21± 0.17	1.95± 0.14
$\langle pi+,pi-\rangle^{\dagger}$	8.97± 0.25	3.45± 0.05
$\langle pi+,pi-\rangle^{*}$	9.46± 0.27	3.74± 0.06
$R^{\pm} = \frac{\langle pi+,pi-\rangle}{\langle pi+,pi-\rangle}$	1.21± 0.04	1.11± 0.03
$R^{*} =$	1.22± 0.05	1.20± 0.04
$D^{\square} = \langle pi^2\rangle - \langle pi\rangle^2$	5.34± 0.67	2.04± 0.03
<pi>/D	1.86± 0.24	1.83± 0.06

† All neon events
* All non-diffractive neon events
□ Calculated for non-diffractive events using NMIN uncorrected for fast protons

R = 1.21 Energy Flux Cascade (1)

R = 1.34 Parton (16)

R = 1.33 Coherent Tube Model (9)

The dispersion

$$D = (\langle pi^{\pm 2}\rangle - \langle pi^{\pm}\rangle^2)$$

is a measure of the width of the σ_n distribution. As expected D increases with increasing <pi±>. The ratio <pi+_>/D is closely related to KNO scaling. If KNO scaling is valid <pi±>/D should be energy independent, as is well supported by the values seen in Table 6. The scaled σ_n distribution is seen in Figure 20 with distributions from 200 GeV/c pi- p and 10.5 GeV/c pi- neon. Significant deviations from KNO scaling are seen for NMIN = 3, 5 and 7 (dominanted by diffractive events). Higher multiplicities satisfy the KNO form except for the wider distribution shown by the neon events when compared to hydrogen.

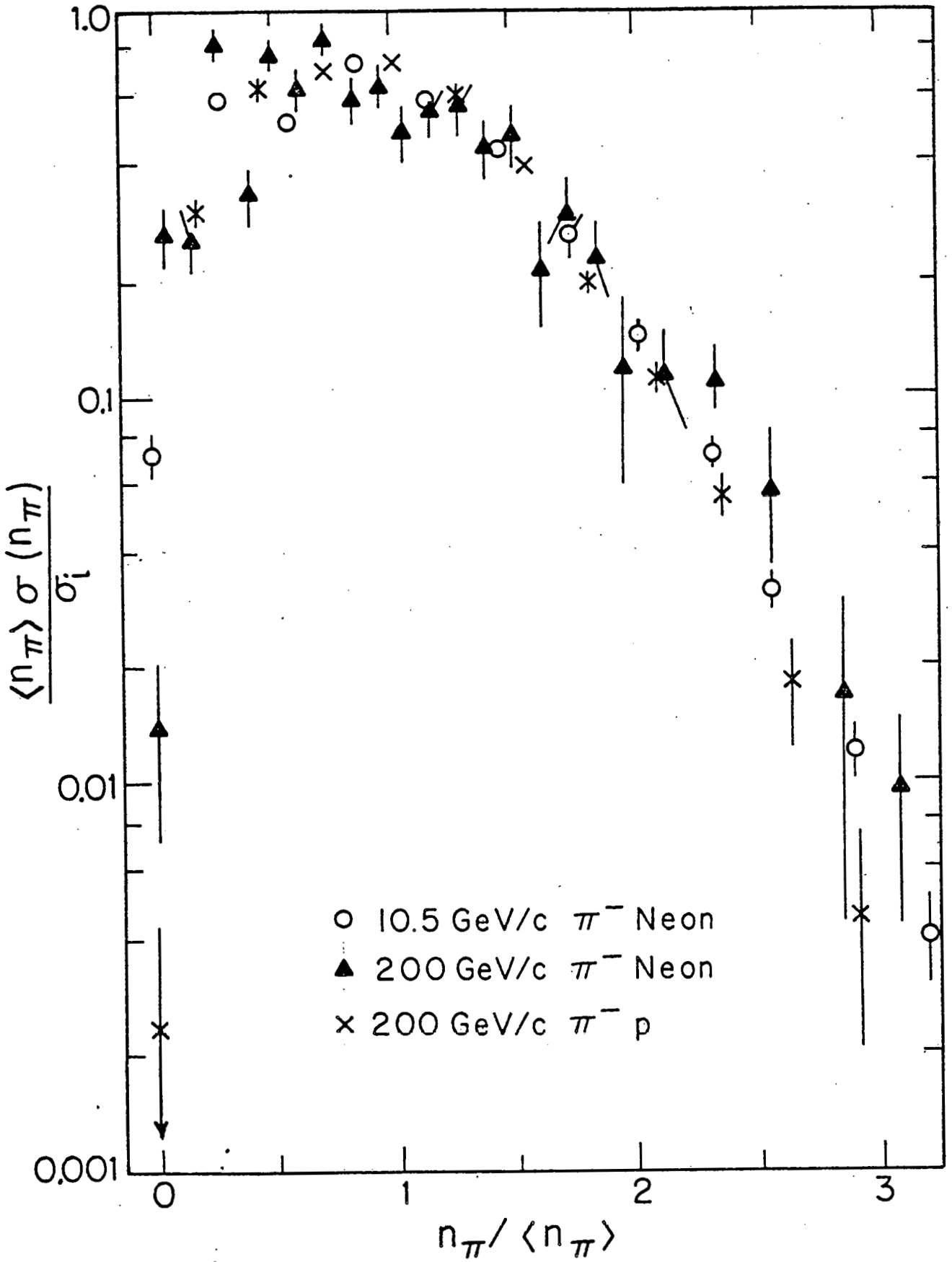

Figure 20: KNO scaling in pi-neon interactions. All inelastic events. Hydrogen multiplicities were modified by assuming 0.6 protons per event.

3.1.2 Protons

The weighted proton multiplicity distribution is shown in Figure 21 a. Events with up to 9 or 10 protons corresponding to the complete breakup of the nucleus are observed. Since the neon nucleus contains equal numbers of protons and neutrons the protons are probably associated with equal numbers of neutrons.

Proton identification was better than 95% for protons with lab momenta between 0.2 and 0.8 GeV/c. Below 0.2 GeV/c protons were missed due to short track length (< 5mm) and the general confusion of tracks about the vertex. Protons above 0.4 GeV/c were identified by scanners on the basis of track density. Because of the unusual bubble chamber operating conditions caused by the neon fill, track densities were found to vary throughout the exposure. Consequently, identification of the faster protons (track density less than twice minimum) was uncertain. Although some protons were identified with momenta up to 1.4 GeV/c other protons of similar energy were misclassified as minimum tracks. These protons were identified by the same procedure used to find the fast (minimum ionizing) protons.

A procedure for estimating the number of fast protons is discussed in Appendix E. The same procedure was used to find

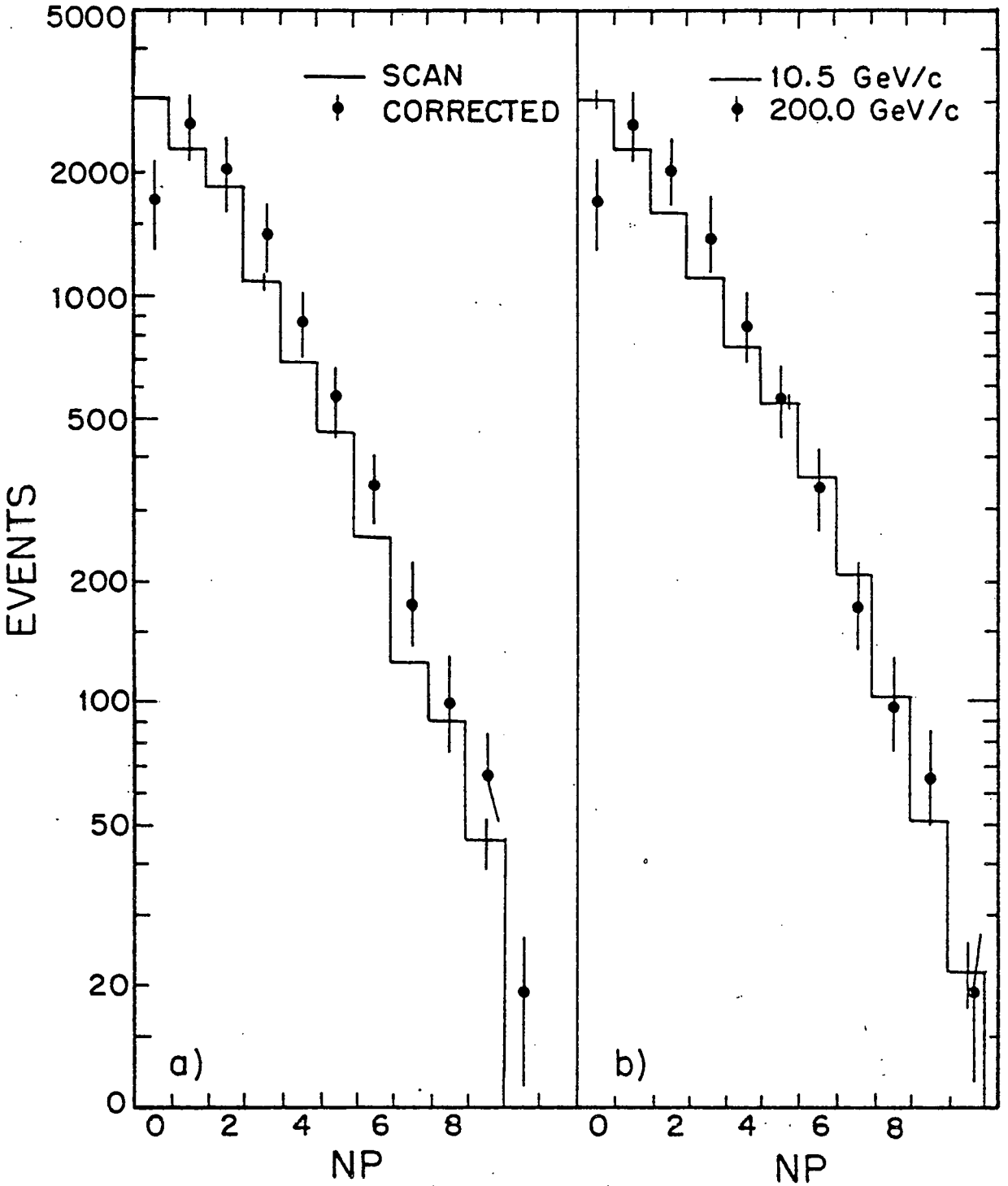

Figure 21: Proton multiplicity distributions.
a) Scan distributions were corrected for fast protons.
b) 10.5 and 200 GeV/c proton multiplicity distributions.
All distributions are normalized to 10000 events.

the number of fast protons as a function of NP. No dependence on NP was found. The scan NP distribution was then corrected by assuming an average of .44 fast protons per event. The corrected proton multiplicity distribution is also shown in Figure 21 a and b.

The corrected proton distribution is compared to that found at 10.5 GeV/c. As seen in Table 6 and Figure 21 b. the average number of protons has increased slightly with energy. For NP>4 the distributions are identical. Further discussion of the change in proton multiplicity is found in subsection 3.2.2.

3.1.3 Gammas

As described in Chapter II the the number of gammas can be estimated from the observed gamma conversions and the gamma conversion probability. Corrections for several small sources of error were then made. Gammas with energy $\leq$ 50 MeV were not measured and were also easily missed during the initial scan. Using Monte Carlo simulations of the pi^0 decay (described in subsection 3.2.3) it was estimated that 2.4 $\pm$ 0.5% of the gammas were $\leq$ 50 MeV. Bremsstrahlung gammas were eliminated during the rescan with possible error +0.0 $\pm$ 1.0%. Very fast neutral strange particles could have been misclassified as gammas at level of -0.5 $\pm$ 1.0%. The total gamma loss was thus 2.2 $\pm$ 1.5%. The weighted number of gammas was corrected for these effects and for loss of gammas during measurement.

In all subsequent discussion it is assumed that all gammas originate from pi^0 decays. This implies that

$$< pi^0 > = 1/2 <\gamma>$$

The average number of gammas for neon is found in Table 7. The ratio of the average gamma multiplicity in neon to that of hydrogen $R(\gamma)$ was also calculated. $R(\gamma)$ has increased slightly when compared to data at 10.5 GeV/c but is extremely close to the ratio found for charged tracks.

A common parameterization of the gamma data at high energies is

TABLE 7

AVERAGE GAMMA MULTIPLICITY

Pi- neon	200 GeV/c	10.5 GeV/c
<gammas>	9.10± 0.27	3.54± 0.3
<pi°>	4.55± 0.24	1.77± 0.05
R^1=<pi°> neon / <pi°> hyd	1.21± 0.05	1.09± 0.07

[1] All neon events

$$< \pi^0 > = 1/2 < \pi^\pm >$$

This is in contrast with low energy data where little or no correlation between <pi°> and <pi±> is found. The dependence of $< \gamma >$ on NMIN is shown in Figure 22. Also shown are the data from the hydrogen events of this experiment. The average gamma multiplicity for both targets rises linearly with increasing NMIN before levelling off to a constant value for NMIN $\geq$ 14. The asymptotic value for the neon events is about 1.5 times that for the hydrogen events.

For NMIN $\leq$ 7 an even - odd dependence in $<\gamma>$ is seen in both hydrogen and neon. Events with NMIN odd are consistent with diffractive production on hydrogen and coherent diffraction on neon. If the non-coherent neon events are produced by either pi-p or pi-n, diffractive events would have NMIN odd or even. A greater proportion of neon events with

NMIN odd are diffractive than with NMIN even. Since diffractive events are generally associated with low $<\gamma>$, the even - odd dependence in $<\gamma>$(NMIN) can be attributed to the differing fractions of diffractive events in even and odd NMIN.

It has been proposed (25) that the $<\gamma>_{NMIN}$ distribution for both hydrogen and neon can be understood in terms of a two component model of particle production. Paricles are produced in a diffractive process (dominant at low NMIN) or by an unspecified non-resonant process (dominant at high NMIN). Diffractive events are associated with low $<\gamma>$. The $<\gamma>$ for the non-resonant production is almost independent of NMIN and is primarily a function of s or the available energy in the center of mass. The observed linear rise in $<\gamma>_{NMIN}$ is caused by the steadily decreasing fraction of diffractive events.

Of particular interest to this experiment is the large NMIN behavior predicted by the model. The $<\gamma>_{NMIN}$ at large NMIN is strongly s dependent. The fact that $<\gamma>_{NMIN}$ for neon is approximately 1.5 times $<\gamma>_{NMIN}$ hydrogen (NMIN large) supports the premise that s and consequently the effective target mass are increased in hadron-nucleus collisions. Similar behavior is also seen $<\gamma>_{NP}$ Figure 23. There exists an almost linear rise between $<\gamma>$ and NP which can be interpreted as evidence for increasing target mass with NP.

Another strongly energy dependent function of the gamma multiplicity is the f_2^{00} moment

$$f_2^{00} = < pi^0(pi^0 - 1) > - < pi^0 >^2$$

Experimental observations (26) and theoretical predictions (27) show that f_2^{00} increases strongly with s. Using the weighted gamma distribution and relations between $< pi^0 >$ and $< \gamma >$ (26) the following values were found

$f_2^{00} = 2.4 \pm 1.1$ hydrogen

$f_2^{00} = 3.8 \pm 1.2$ neon

Again the difference between the hydrogen and neon events can be explained by the larger energy available in hadron - nucleus collisions.

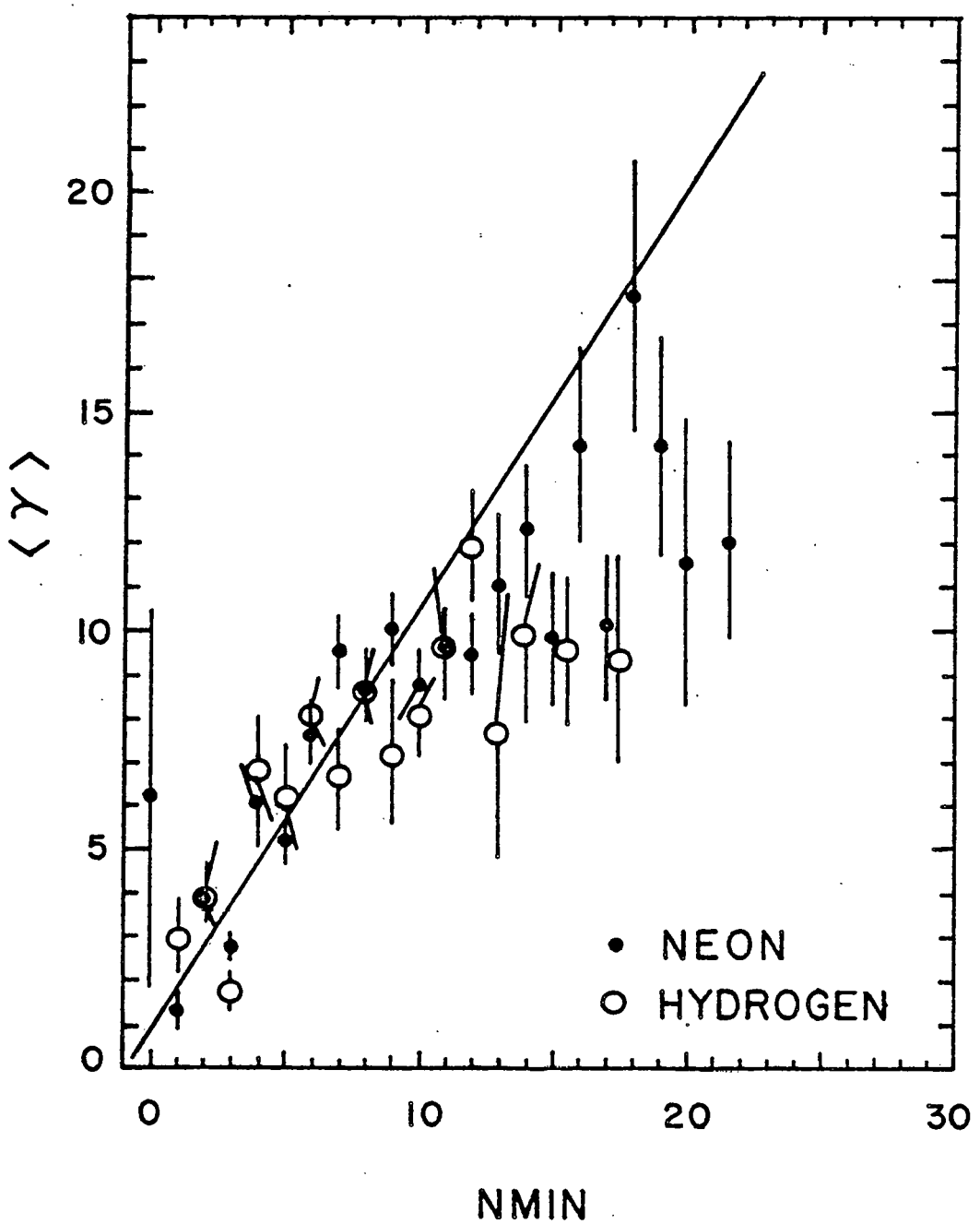

Figure 22: Gamma multiplicity vs NMIN for 200 GeV/c pi- neon and hydrogen.

3.1.4 Correlations

Previous emulsion and bubble chamber experiments (11,12,10) have noted a correlation between the observed number of protons (NP) and the average multiplicity of the event $\langle pi^{\pm} \rangle$. Several theories (9,13,14) suggest the use of NP as a measure of the effective target mass in the collision. The center of mass energy

$$s = 2\, M(\text{target})\, E(\text{beam})$$

increases for a fixed energy beam as the target mass increases. As noted in the Introduction $\langle pi^{\pm} \rangle$ is proportional to ln(s). Thus events with several observed protons should be associated with events of high average multiplicity.

The average pion multiplicity was calculated as a function of NP as shown in Figure 23. A definite increase in $\langle pi^{\pm} \rangle$ with large NP is seen. The events with largest NP would have R values of 1.5. In contrast the NP = 0 events which are dominated by diffractive processes have a smaller average multiplicity than hydrogen events. $\langle pi^{\pm} \rangle$ shows signs of levelling off at large NP, perhaps indicating that the maximum number of protons are already involwed in the collision. The average gamma multiplicity $\langle \gamma \rangle$ corresponds well to $\langle pi^{\pm} \rangle$ indicating that the $\langle pi^{0} \rangle$ dependence on NP is the same as for the charged pions.

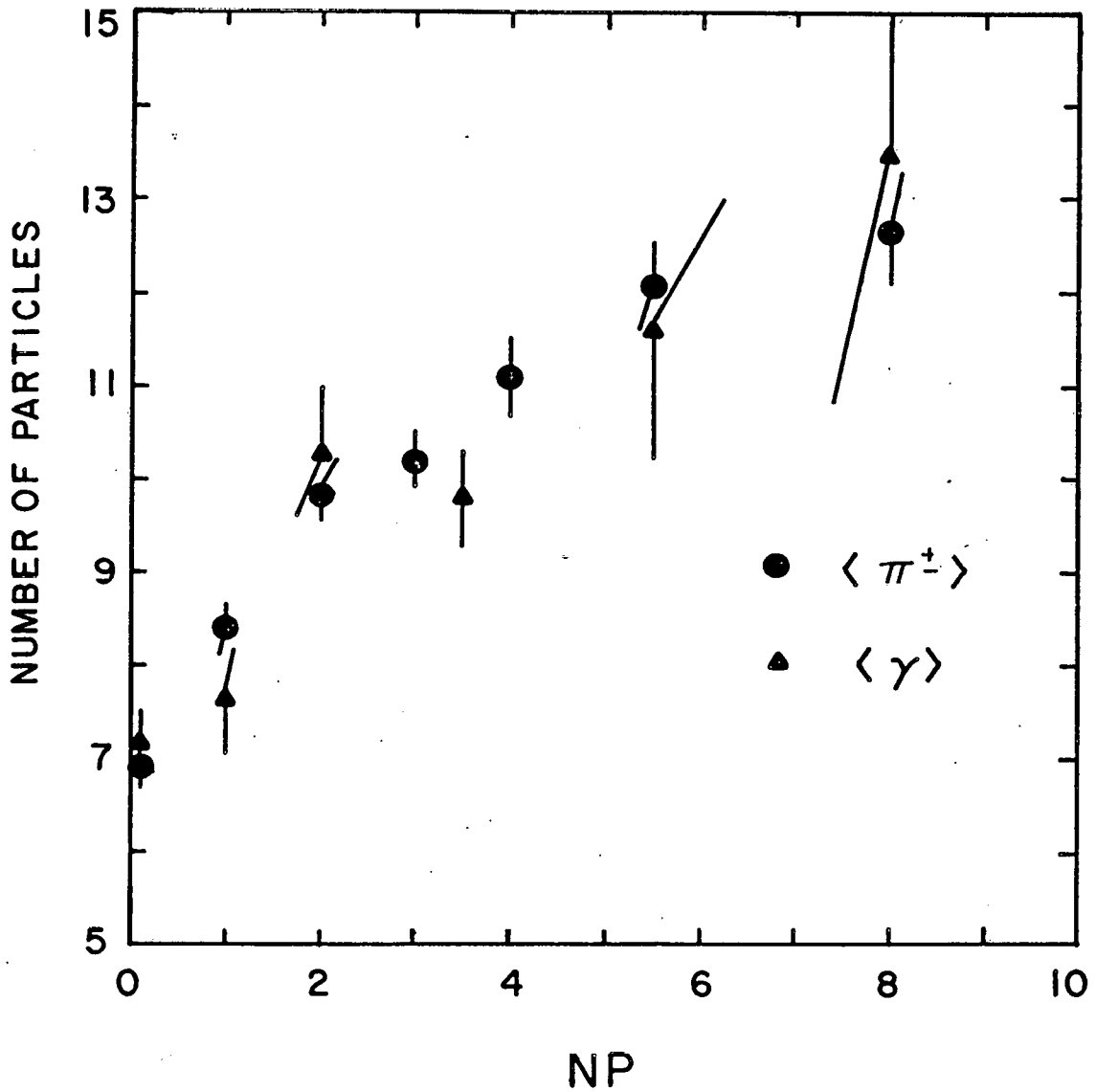

Figure 23: Average pion and gamma multiplicity vs NP. (number of observed protons). Data sample was all inelastic neon events at 200 GeV/c.

If <pi±> at each NP is scaled by the overall average multiplicity, the data at 200 GeV/c can be compared with data at 10.5 GeV/c (Figure 24). Striking agreement between the data are seen. The increase in particle production in pi - nucleus collisions is seen to depend strongly on the number of observed protons and very little if at all on the beam energy. Models of pion nucleus interactions in which the collision parameters' dependence on NP is energy independent would be supported by these data.

Figure 25 shows the NMIN distribution (uncorrected) for several cuts on the number of protons. The most prominent feature of the NP = 0 or 1 events are the large diffractive peaks at 3,5 and 7 NMIN. These diffractive peaks are absent for the NP>1 events which have broad central regions shifting to higher NMIN as NP increases. The fraction of events which can be attributed to diffraction processes decreases dramatically as NP rises.

The dispersion (D) for each group of events was calculated (Table 8). As expected the dispersion increases with NP. The ratio of D to <pi±> is seen to decrease with NP. The dependence of the D/<pi±> on NP implies that the same KNO scaling function will not describe events with differing NP. When averaged over all NP KNO scaling behavior was shown in section 3.1.1. Early versions of the Tube model (9) predicted KNO scaling for all NP in contrast to our results.

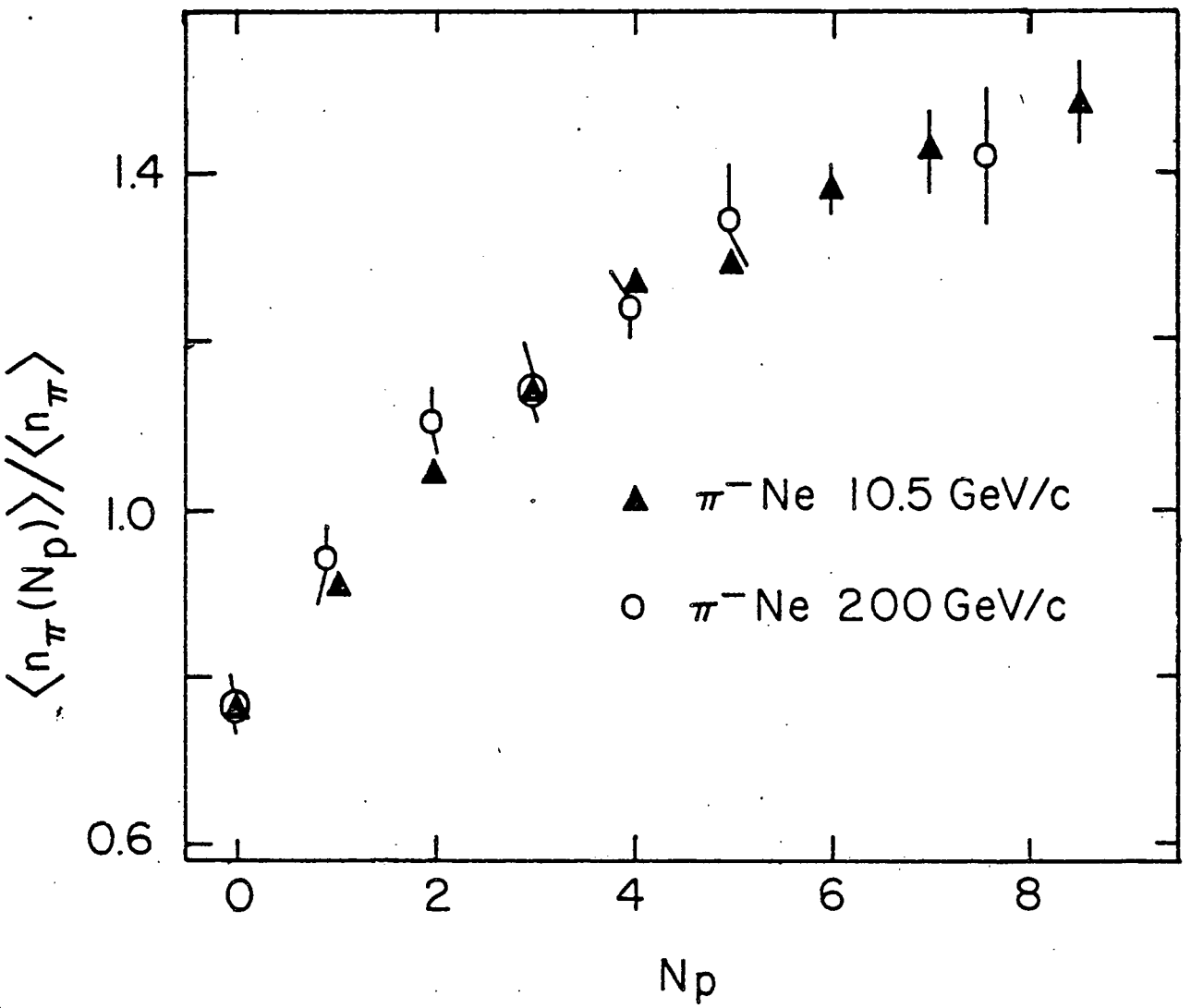

Figure 24: Scaled pion multiplicity vs NP. Data sample was all inelastic events.

Later variations (13,14) however, predict scaling only if averaged over all NP values.

TABLE 8

DISPERSION

	Dispersion	D/<pi±>
NP = 0,1	4.80 + 0.33	.59 + 0.04
NP = 2,3,4	5.38 + 0.49	0.50 + 0.05
NP≥ 5	6.00 + 0.95	0.47 + 0.08

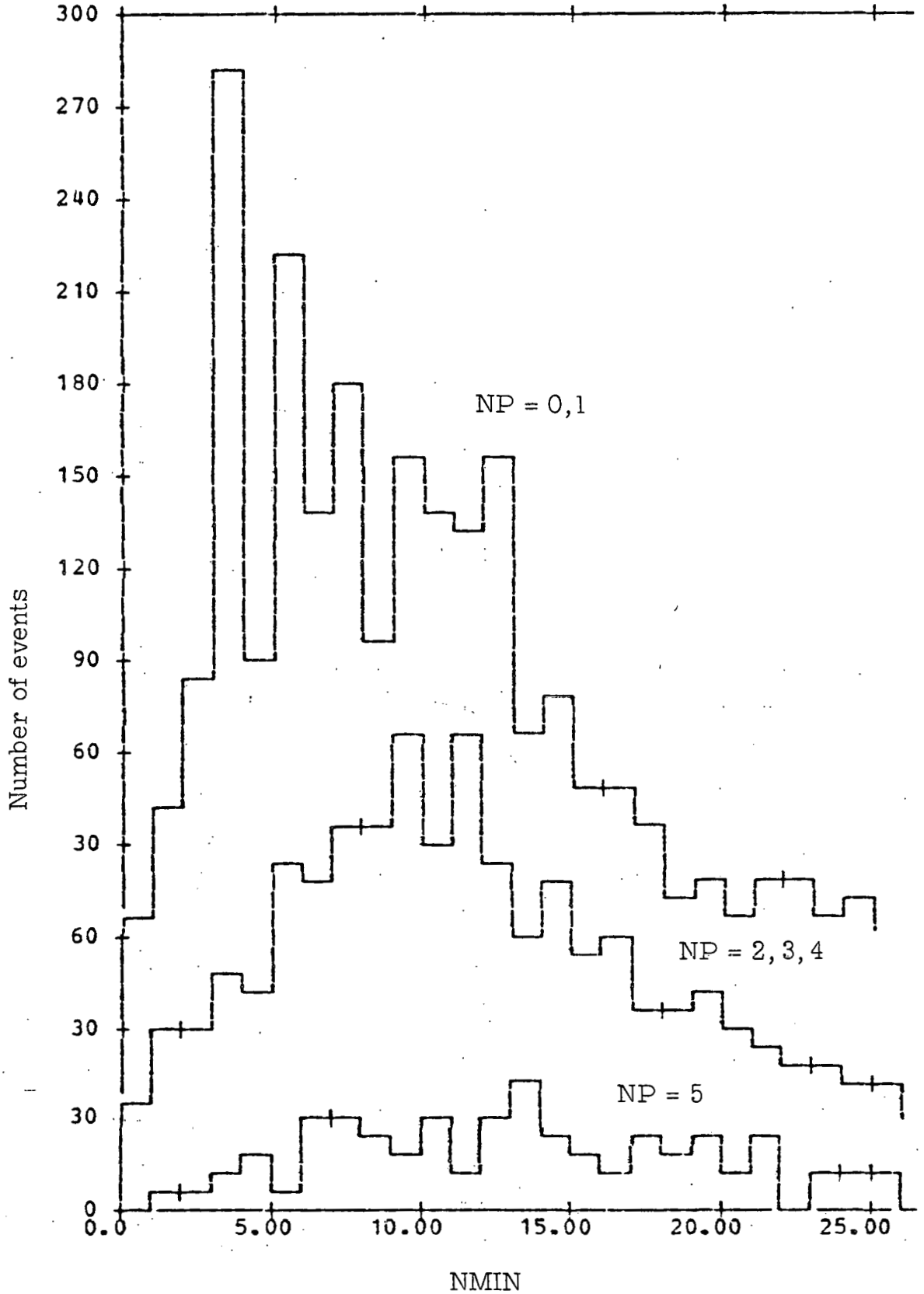

Figure 25: NMIN distributions vs NP. Data are uncorrected for fast proton or gamma contamination.

3.2 SINGLE PARTICLE SPECTRA

The average pion, gamma and proton multiplicities of neon events have been shown to be significantly larger than the corresponding multiplicities on hydrogen. Study of the single particle distributions will define the kinematic properties of the increased particle production.

The single particle spectra of this experiment's 200 GeV/c pi- neon interactions are compared to spectra from 10.5 GeV/c pi- neon and 200 GeV/c pi- p. Ideally comparisons to the hydrogen data would be supplemented by comparisons to pi- neutron data. No such data exist, however, at comparable beam energies. Comparisons of the neon data to hydrogen data show a pronounced dependence on the charge of the pion. This dependence is due in large part to those neonic interactions which resemble pi- neutron collisions.

3.2.1 Charged pions

In Figure 26 the PT^2 distributions of pi- from 200 GeV/c pi- neon and hydrogen are compared. The distributions are normalized by division of < pi- >. No appreciable difference is seen between the two distributions. The PT^2 distribution is insensitive to the exact nature of the target or to whether the particles are produced by single collisions (hadron - nucleon) or multiple collisions (hadron - nucleus).

Figures 27 and 28 show the longitudinal momentum ($p_{||}$) spectra of pi- and pi+ from neon and hydrogen interactions at 200 GeV/c. The neon pi+ data were corrected for fast protons (Appendix E). Both pi+ and pi- show a strong excess multiplicity (1.6 to 2.8 times) over the corresponding hydrogen data for $p_{||} \leq 0.2$ GeV/c. For $p_{||} > 0.2$ GeV/c the comparison between neon and hydrogen is quite different for pi+ and pi- final state particles. The neon pi- are consistently higher than the hydrogen pi- ($p_{||} \geq 0.2$). Above $p_{||}$ = 1 GeV/c the pi+ hydrogen and neon data are virtually indistinguishable. The ratio R

$$R = \frac{< pi\pm > \text{ pi- neon}}{< pi\pm > \text{ pi- hydrogen}}$$

for the region $-0.6 \leq p_{||} \leq 9.0$ GeV/c

$$R = \int \frac{d\sigma}{dp_{||}} dp_{||} \text{ neon} \Big/ \int \frac{d\sigma}{dp_{||}} dp_{||} \text{ hydrogen}$$

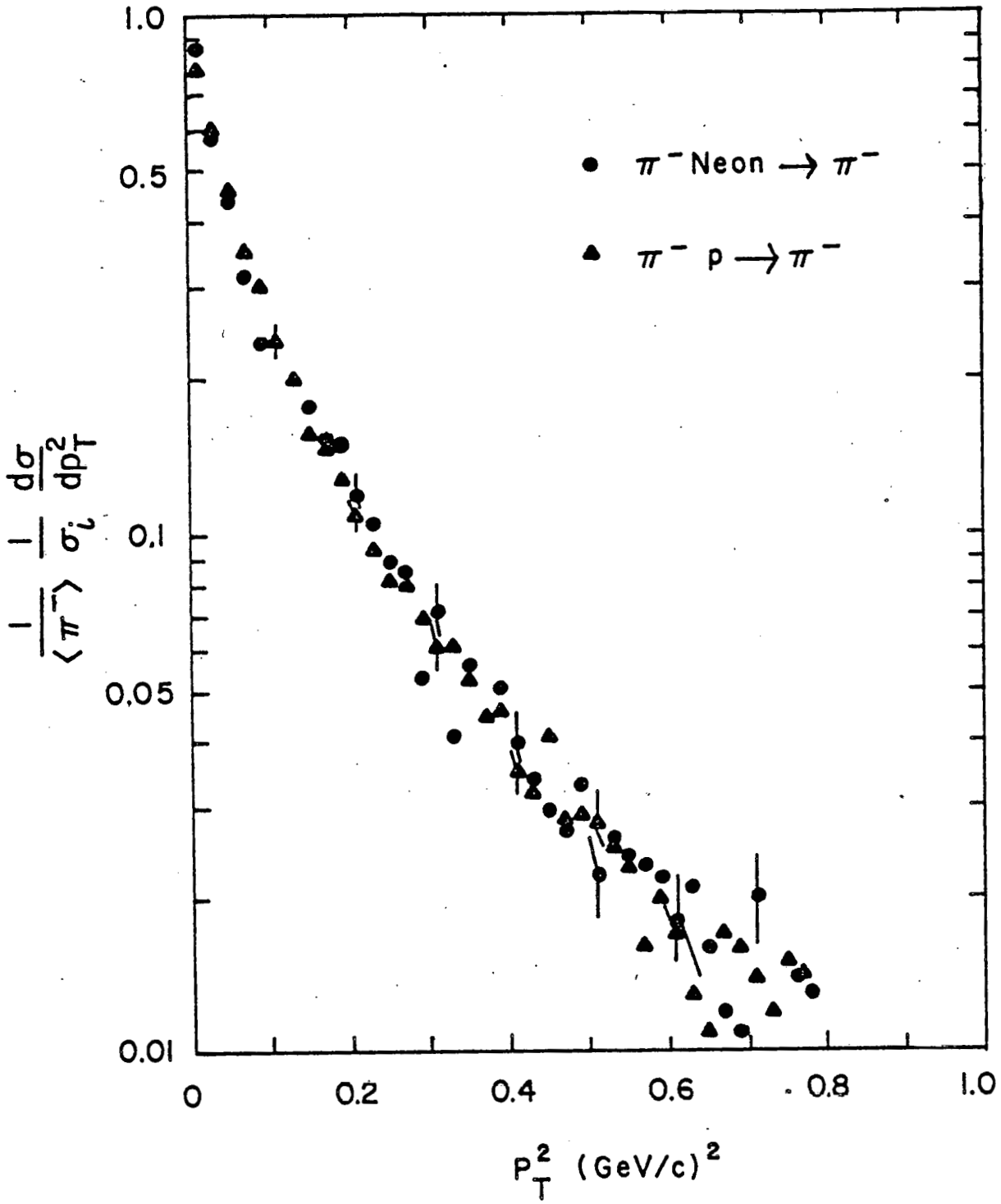

Figure 26: PT**2 distributions of 200 GeV/c neon and hydrogen.

was found to be 1.13± 0.02 for pi+, 1.42± 0.03 for pi-, and 1.26± 0.02 averaged over all charges.

Figure 29 compares the pi- $p_{||}$ distributions at two beam momenta, 200 GeV/c and 10.5 GeV/c. There are more pi- in the region $p \leq 0.4$ GeV/c at 10.5 GeV/c than at 200 GeV/c despite the much higher multiplicity of the higher energy events. The increased multiplicity due to increased energy is only apparent above $p_{||} = 1.0$ GeV/c.

The p behavior with seen in neon is very similar to that found for pi+ and pi- proton collisions. Whitmore et al. (23) have shown that limiting fragmentation in the target region is only valid at the high energy limit ($s^{-1/2} = 0$). At beam energies of 100 GeV or less limiting fragmentation is only approximately true. (Limiting fragmentation implies that the particle production in the target or beam fragmentation region is independent of the exact quantum numbers of the beam or target.)

If the integrated cross section for the range $-0.4 \leq p_{||} \leq 0.2$

$$ICR = \int \frac{E \quad d\sigma\, dp_{||}}{dp_{||}}$$

for several different experiments (23) is plotted against $s^{-1/2}$ (Figure 30). A linear dependence on $s^{1/2}$ is seen.

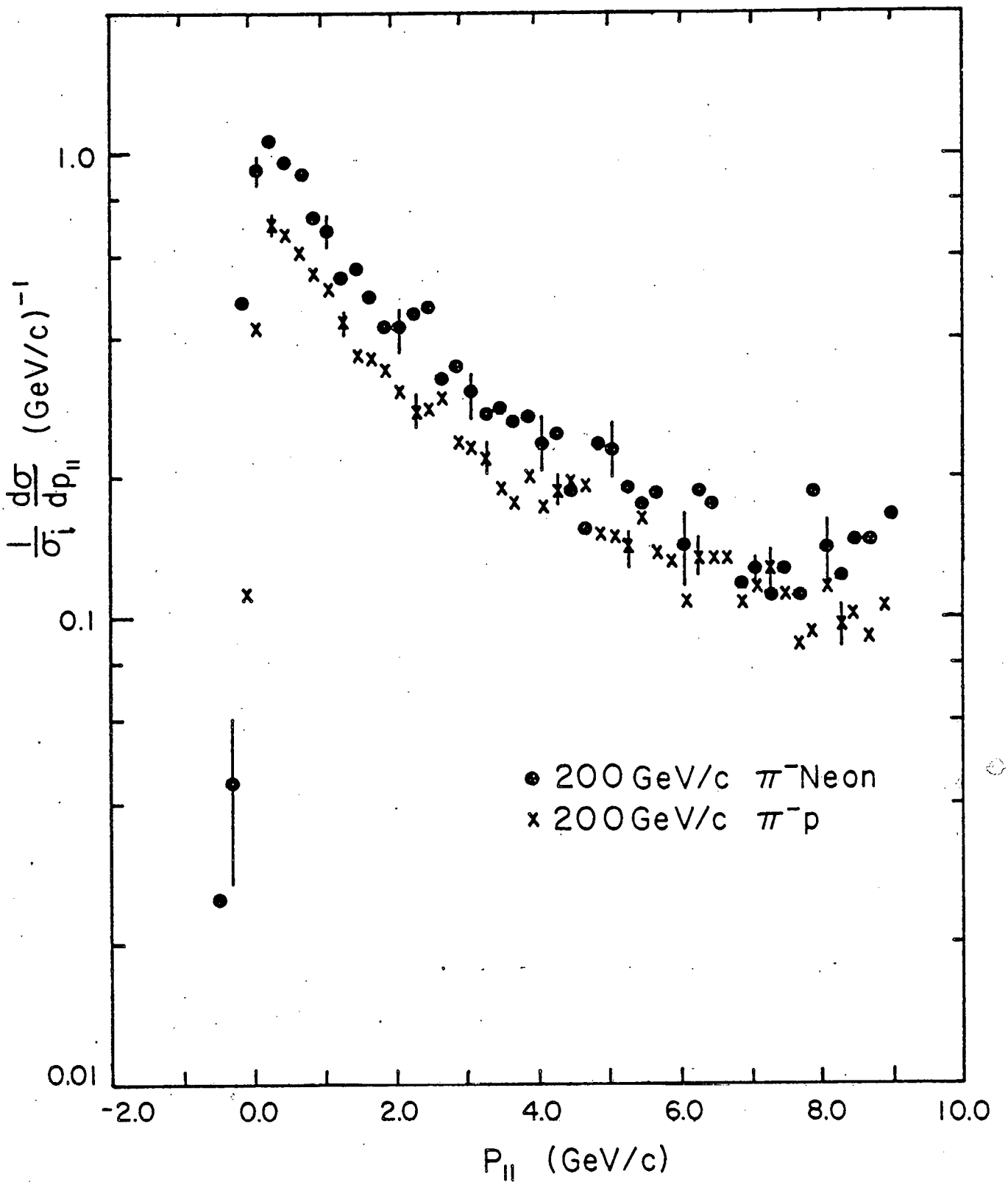

Figure 27: Pi- longitudinal momenta for neon and hydrogen.

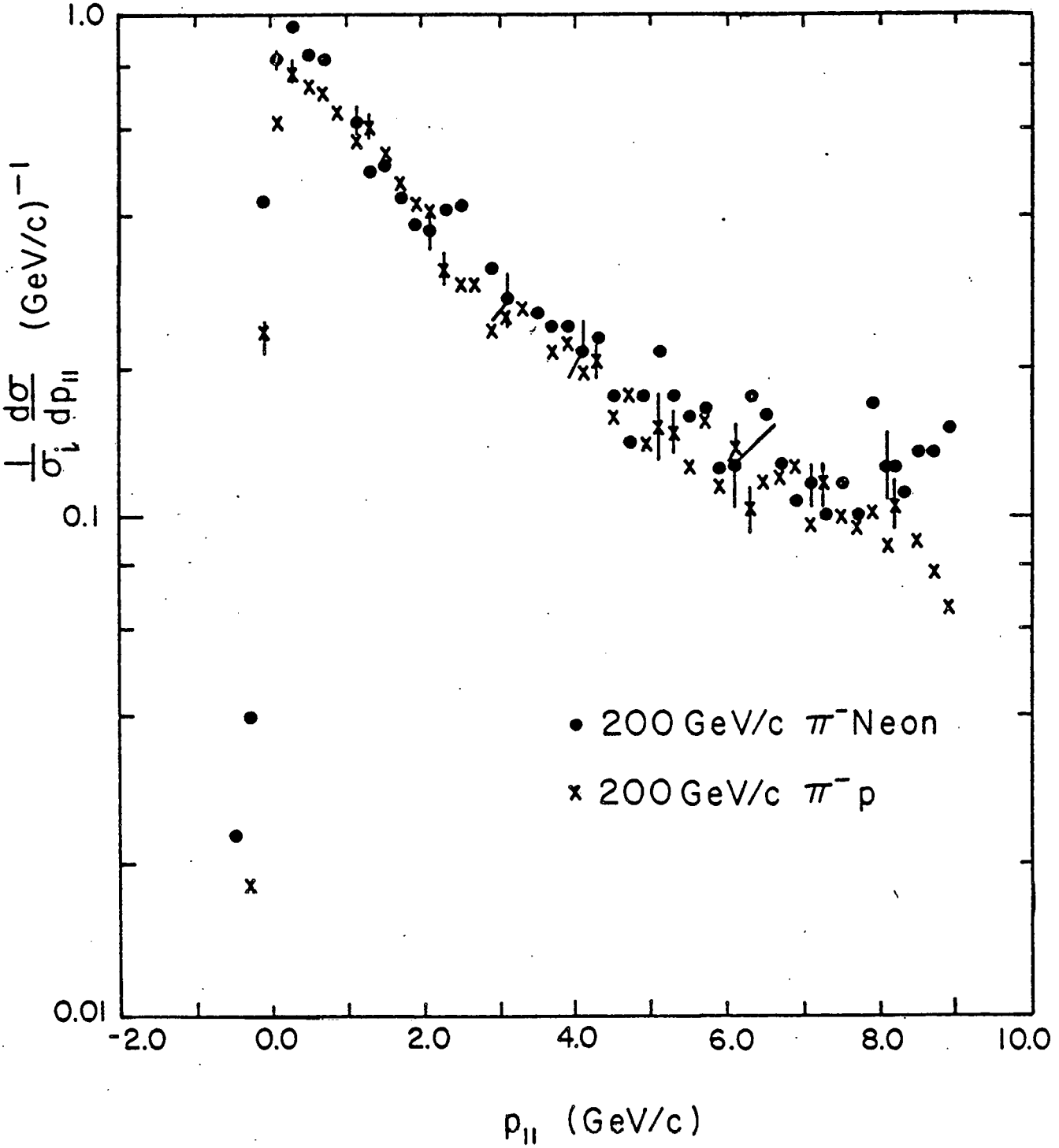

Figure 28: Pi+ longitudinal momenta for neon and hydrogen.

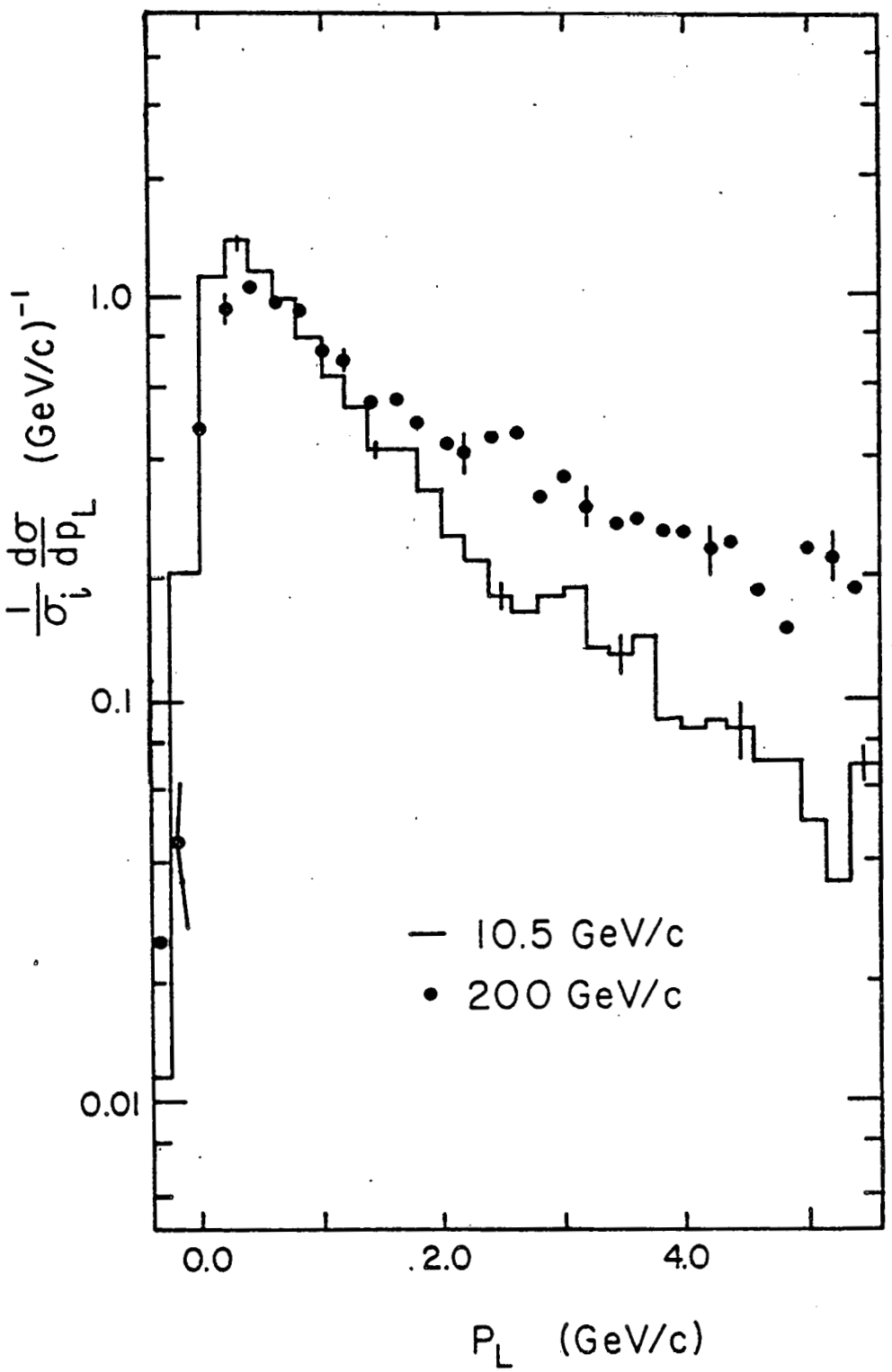

Figure 29: Pi- longitudinal momenta at 200 and 10.5 GeV/c neon.

If the corresponding values for neon at 200 GeV/c and 10.5 GeV/c are plotted (Figure 30) similar behavior is seen. Linear extrapolations to $s^{-1/2} = 0$ show that not only are the cross sections insensitive to the charge of the beam, but they are also equivalent for pi+ and pi- final states. This is in contrast to the hydrogen data where pi+ final states have larger cross sections than pi-. This probably reflects the equal numbers of protons and neutrons in the neon nucleus.

The asymptotic value ($s^{-1/2} = 0.0$) of the integrated cross section in this $p_{||}$ range is 0.072 ± 0.006 for both pi+ and pi-. The corresponding values for hydrogen are 0.024 ± 0.002 for pi- and 0.042 ± 0.002 for pi+ final state particles. As noted previously the hydrogen asymptotic values reflect the preferred fragmentation of the target proton into slow pi+. If the ratio of the asymptotic values is calculated

$$R(-0.4 \leq p_{||} \leq 0.2) \quad \frac{(\text{pi- neon})}{(\text{pi- p})}$$

$$= 3.0 \pm 0.4 \qquad \frac{\text{pi-Ne} \rightarrow \text{pi-}}{\text{pi-Ne} \rightarrow \text{pi+}}$$

$$= 1.7 \pm 0.2 \qquad \frac{\text{pi-Ne} \rightarrow \text{pi+}}{\text{pi-p} \rightarrow \text{pi+}}$$

$$= 2.2 \pm 0.3 \qquad \frac{\text{pi-Ne} \rightarrow \text{pi}\pm}{\text{pi-p} \rightarrow \text{pi}\pm}$$

The predictions of the Energy Flux Cascade(1) and the Parton models (16) are $R = \bar{\nu} = 1.55$ in the target fragmentation region.

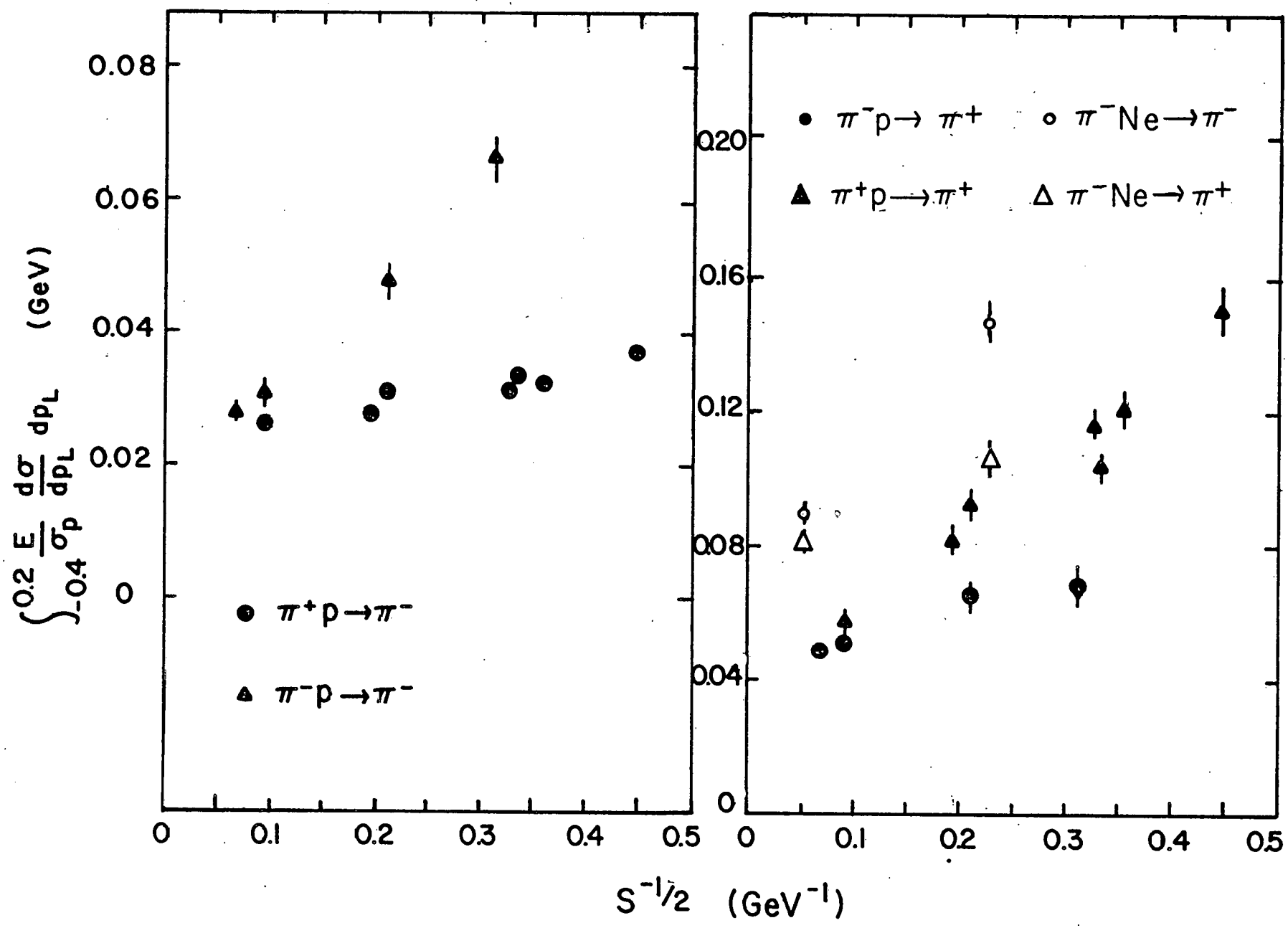

Figure 30: Projectile dependence in the target fragmentation region. Data are from reference 23.

The pi+ and pi- rapidity (lab) distributions of both hydrogen and neon are seen in Figures 31 and 32. The neon pi+ distributions are contaminated by minimum ionizing protons (20% of the tracks with $y < 3.0$). As in the $p_{||}$ distributions the pi+ and pi- comparisons differ dramatically.

A more quantitative comparison of pion production in neon interactions and hydrogen interaction is made through

$$R(y) = \frac{\sigma_i(\text{hyd})}{\sigma_i(\text{neon})} \frac{d\sigma(\text{neon})}{dy} \Big/ \frac{d\sigma(\text{hyd})}{dy}$$

which is plotted in Figure 33. A charge dependence in R(y) is seen except for $y \leq 0.5$ and $2.0 \leq y \leq 5.0$. The large R(y) for $y \leq 0.5$ may be evidence for cascading of the slowest pions. The R(y) for pi+ are still contaminated by protons with $y < 3.0$. The parton model predicts the R(y) function in the central rapidity region (see Figure 33). Although close to the pi- values the predicted R(y) is too small for $y > 4.0$.

The pi- rapidity distributions are compared to pi- rapidity spectra of 10.5 GeV/c pi- neon interactions (Figure 35). The large increase in particle multiplicity at the higher energy is evident as well as the shifting of the center of the distribution to the new center of mass. As in the $p_{||}$ distributions, energy independence has not been reached in the target fragmentation region. The maximum particle density (in the central region) increases slightly with beam energy as do corresponding data for pi-p data (Figure 3).

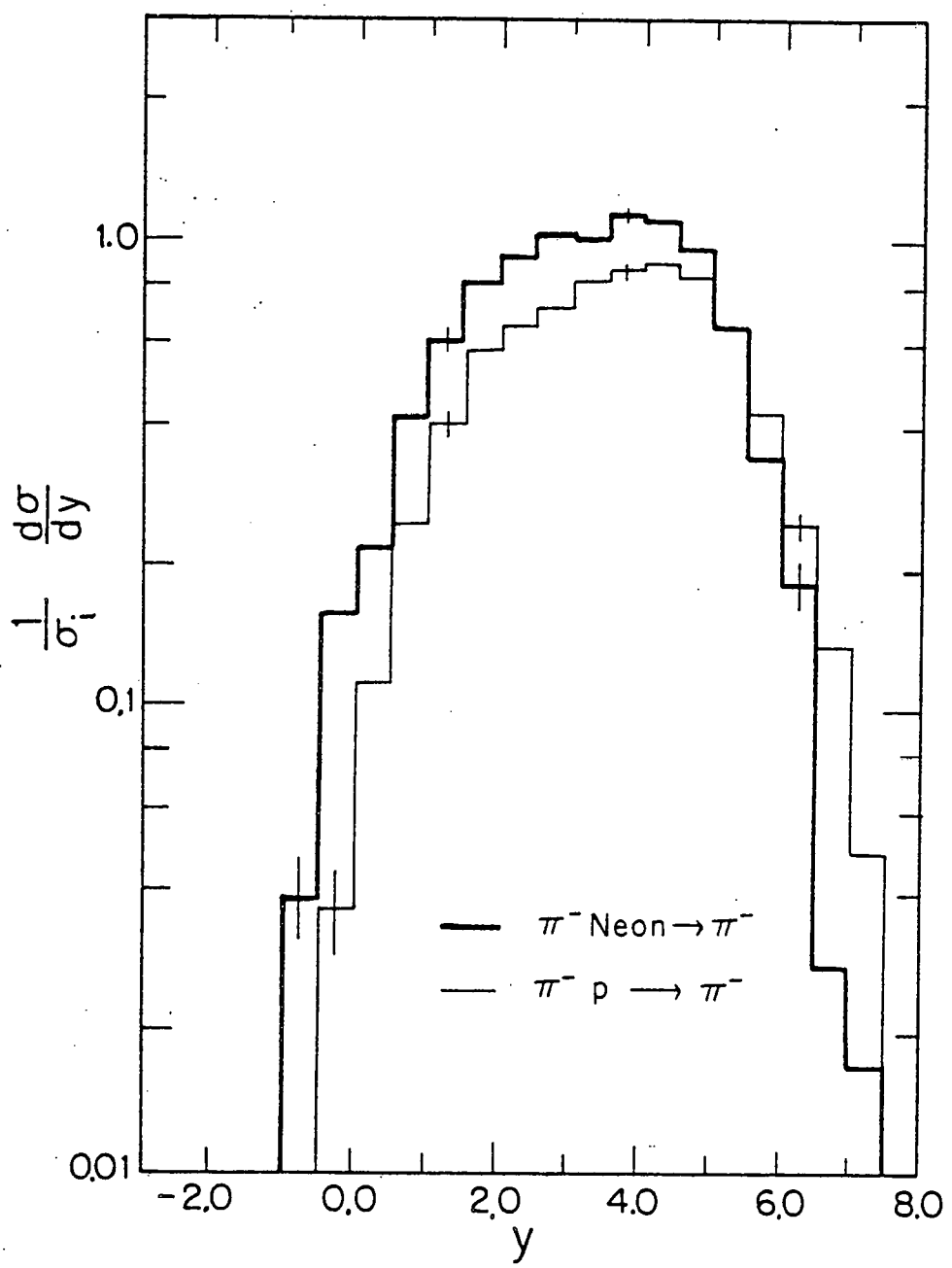

Figure 31: Pi- rapidity 200 GeV/c neon and hydrogen.

To compare the R as a function of rapidity for the neon targets at the two energies, the rapidity y is transferred to the center of mass frame and scaled by the maximum rapidity y(max) (y(max) = y(beam)). The resulting $R(\hat{y})$ distributions are shown in Figure 34. Both $R(\hat{y})$ have comparable values in the extreme target fragmentation region ($y < 0.5$). At 10.5 GeV/c $R(\hat{y})$ is a smoothly falling function going through 1.0 at a value near the center of mass before levelling off in the beam fragmentation region. At 200 GeV/c $R(\hat{y})$ falls more quickly with increasing $\hat{y}$, but reaches a constant value in the central fragmentation region before crossing 1.0 in the beam fragmentation region.

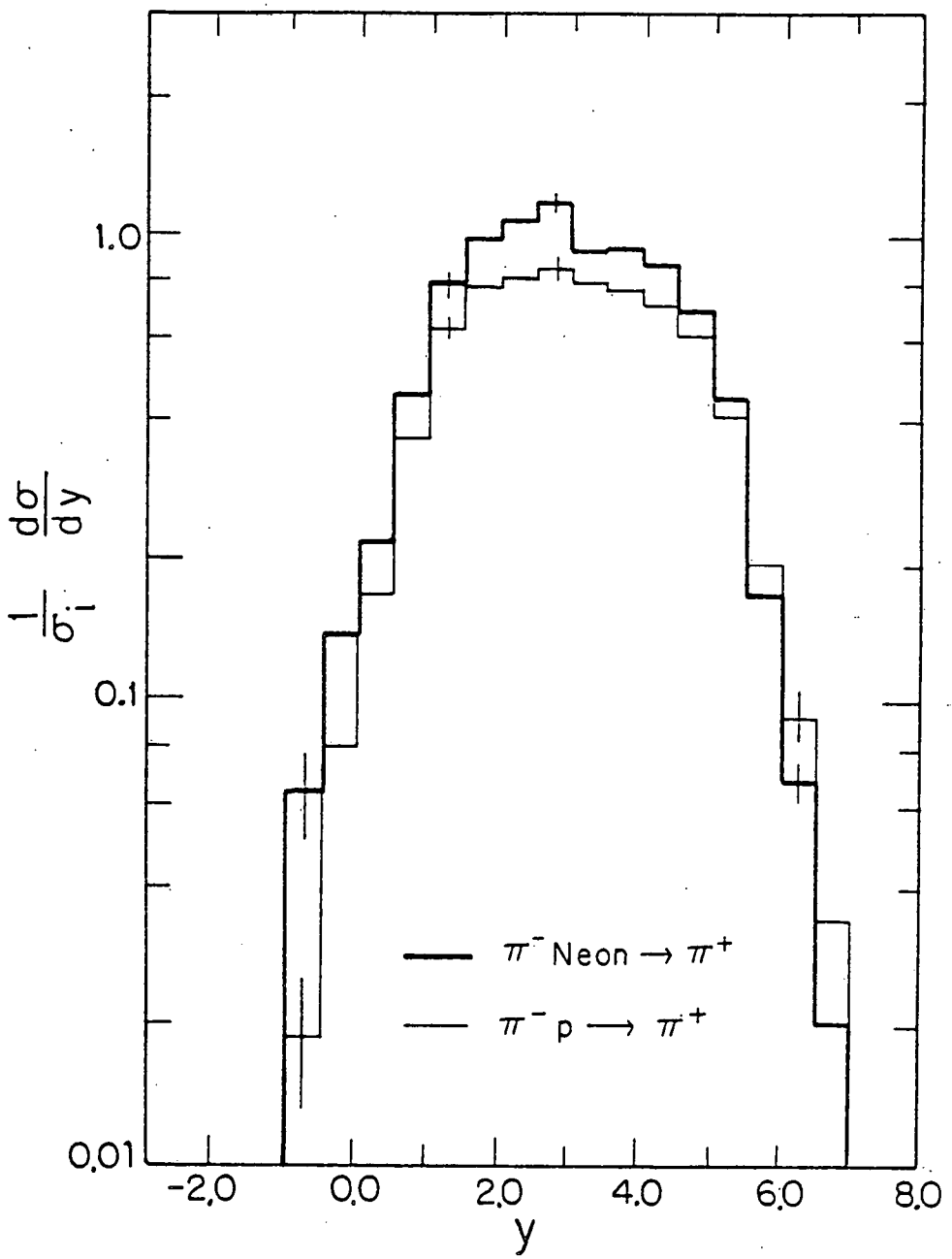

Figure 32: Pi+ rapidity at 200 GeV/c for hydrogen and neon.

The pi- rapidity distributions of 200 and 10.5 GeV/c pi-neon interactions are shown in Figure 35. The shift in the central maximum is readily apparent (ycm = 1.5 at 10.5; ycm = 3.03 at 200 GeV/c). The target fragmentation region shows signs of energy dependence (in contrast to predictions of energy independence) with more pions produced with $y < 1.0$ at 10.5.

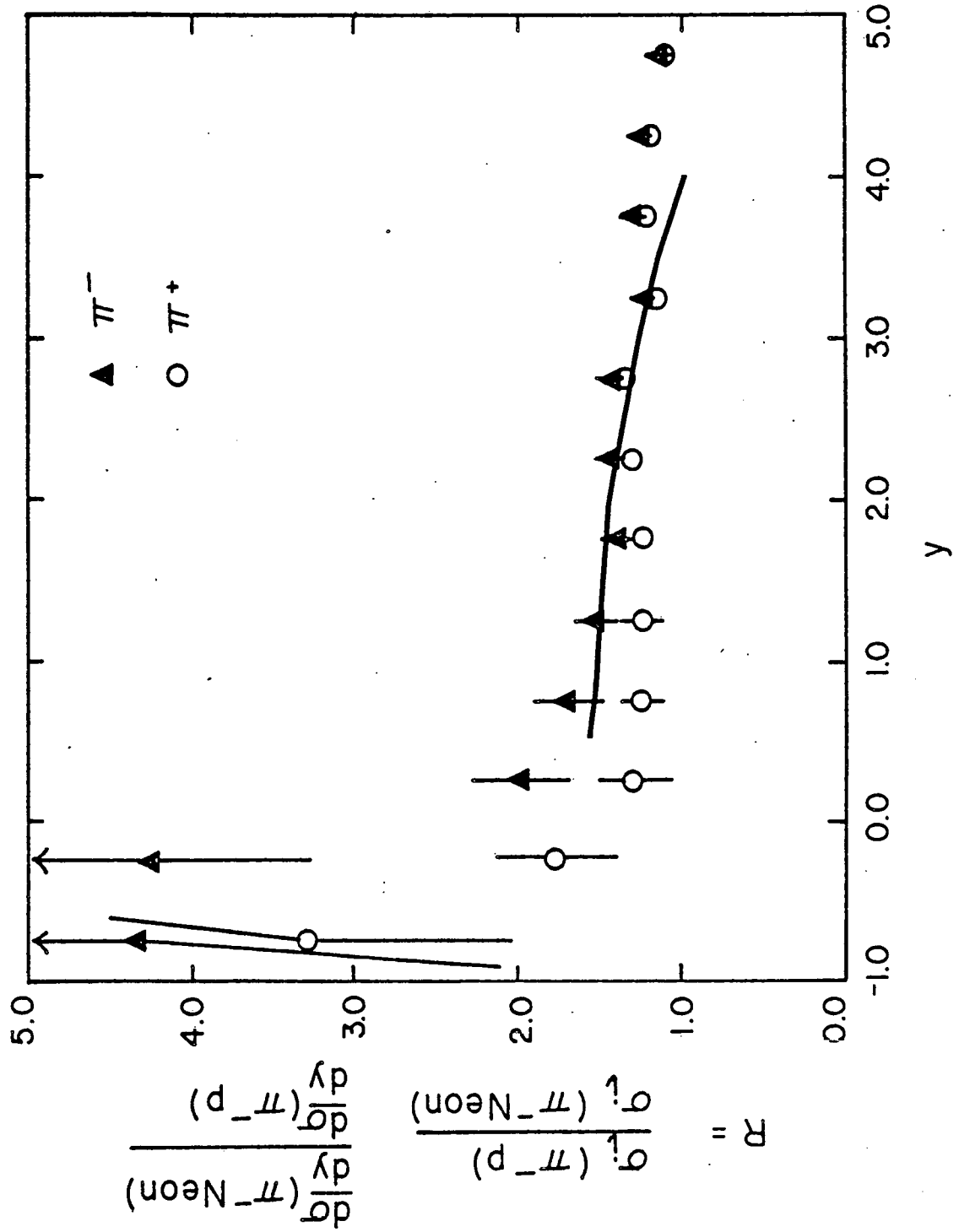

Figure 33: R(y) for pi+ and pi- at 200 GeV/c.

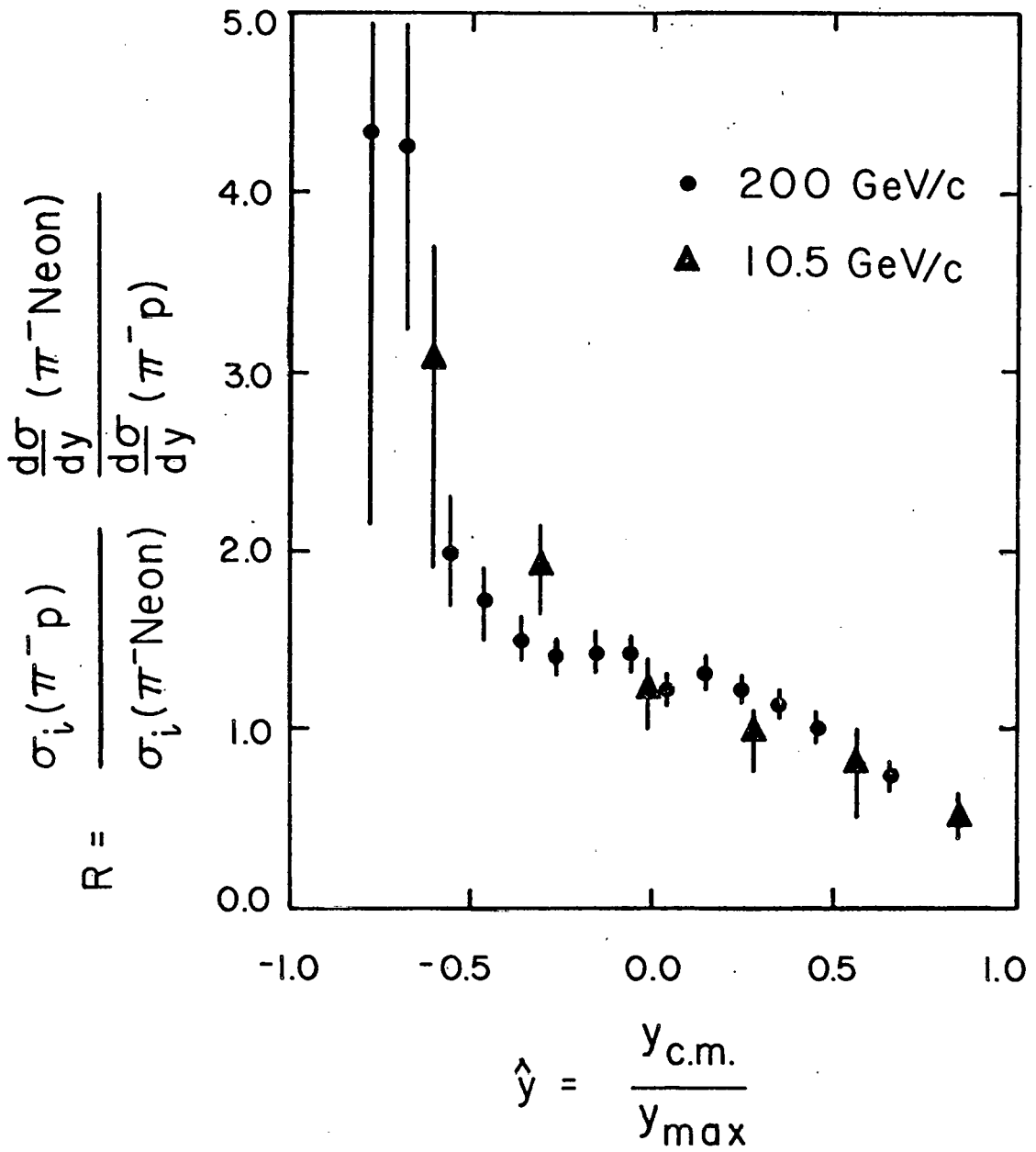

Figure 34: R as a function of the scaled rapidity at 10.5 and 200 GeV/c.

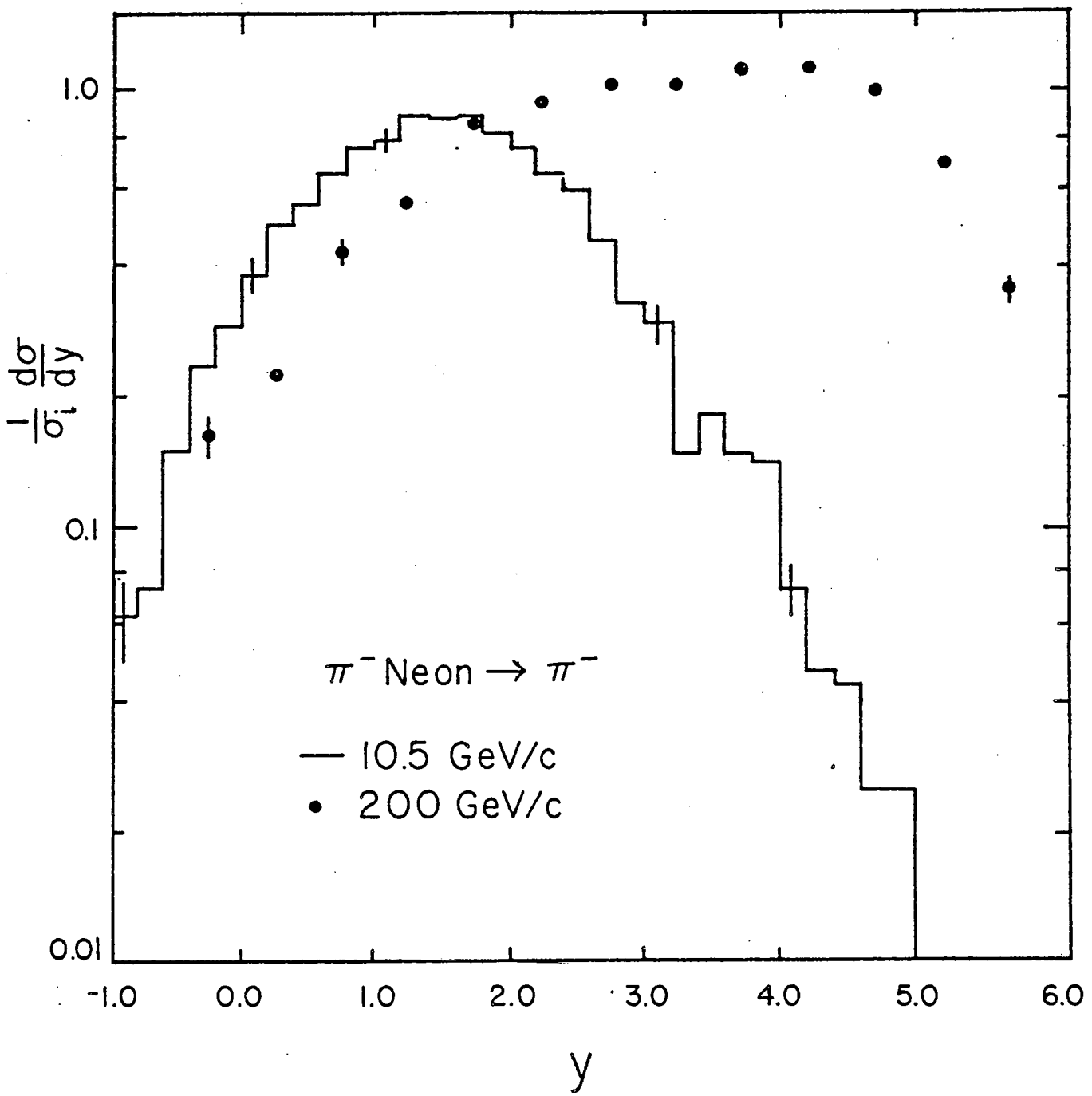

Figure 35: Pi- rapidity at 200 and 10.5 GeV/c.

3.2.2 Protons

As discussed previously the protons fall into two categories; the scan identified protons and the minimum ionizing protons. The scan identified protons are seen with momenta $\leq$ 1.4 GeV/c with the probability for scan identification falling quickly above 0.8 GeV/c. The statistical method for obtaining the minimum ionizing protons is covered in detail in Appendix E. This method estimated the longitudinal momentum ($P_{||}$) distribution of the fast protons. In order to compare the 200 GeV/c data with the 10.5 GeV/c data, the laboratory momentum distributions were needed. The same subtraction procedure was used as in Appendix E but with p(lab) as the particle variable. The validity of this procedure is supported by the fact that both procedures yield the same number of fast protons.

In Figure 36a the laboratory momentum of the scan identified protons and the total proton sample are plotted. The scanned proton momentum distribution was corrected for measuring losses by a track weight which decreased with increasing momentum. The proton momentum spectrum is peaked at momenta < 400 MeV/c. Protons of this or smaller momenta are consistent with the breakup of the neon nucleus after an interaction.

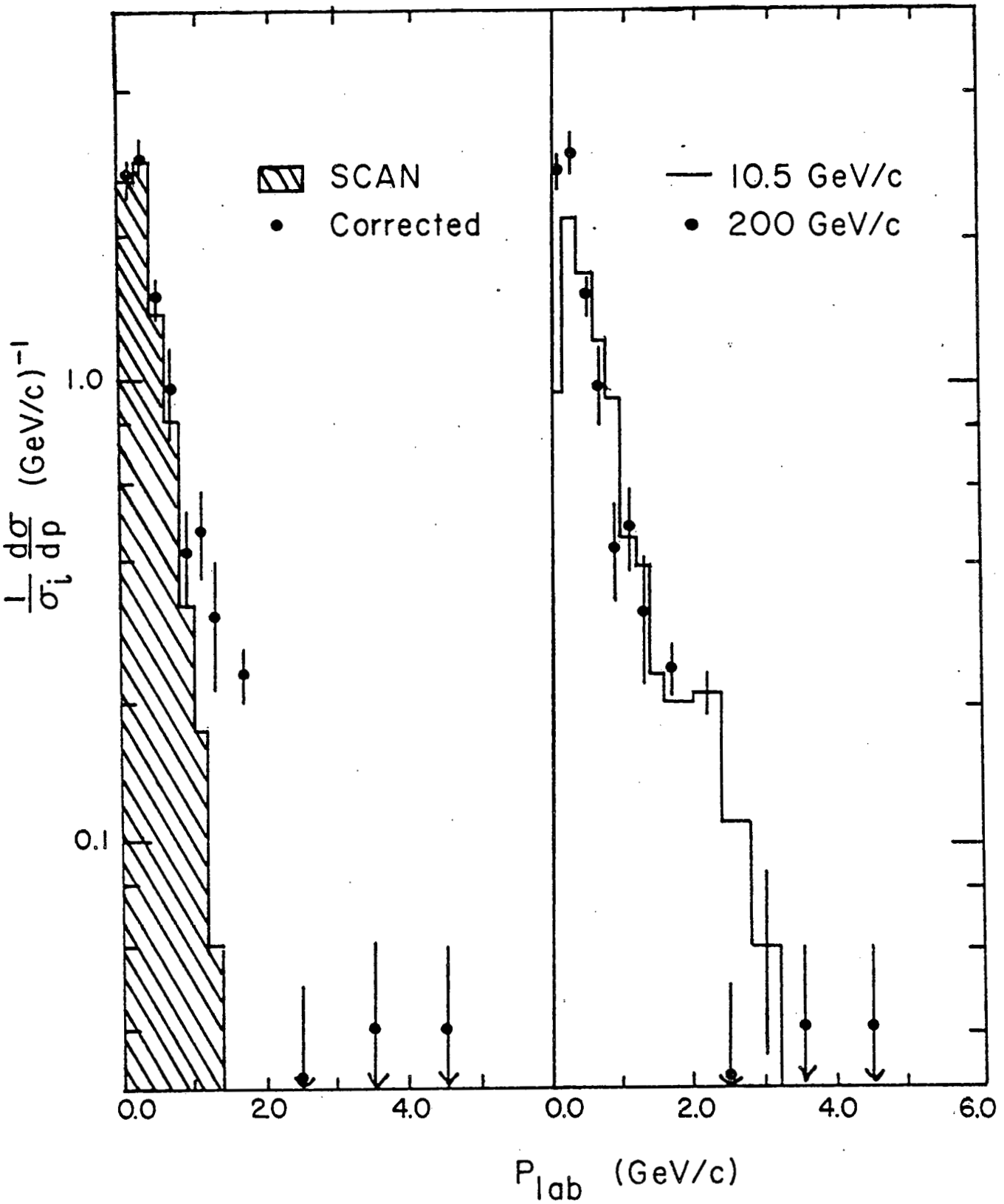

Figure 36: Proton momentum distribution.
a) Scan proton momentum distribution was corrected for minimum ionizing protons.
b) Proton distributions of 200 GeV/c and 10.5 GeV/c are compared.

In Figure 36b the proton momentum distributions of 10.5 and 200 GeV/c pi- neon interactions are compared. Below 0.4 GeV/c the number of protons at 200 GeV/c has increased by a factor of two when compared with the low energy data. Above 0.4 GeV/c the number of protons at 200 GeV/c has decreased by 20%. Given the experimental difficulties associated with the proton measurements, it is probable that the proton momentum distribution is energy independent. The near energy independence of the proton distributions contrast sharply with the energy dependence seen in the pi+ and pi- distributions. The energy independence in proton multiplicity could be explained in terms of the CTM, however, an energy independent proton momentum distribution is not compatible with the assumptions of the CTM.

3.2.3 Gammas

Gamma momentum measurements were only attempted on gammas whose scan table estimated energy was greater than 50 MeV and less than 3 GeV. Momentum measurements of these gammas were often of poor quality due to bremsstrahlung radiation losses of the $e^{\pm}$. Thus the momentum measurements were of limited range and utility.

For particles of zero mass the pseudo - rapidity

$$\eta = -\ln[\tan(\theta/2)]$$

(where θ is the angle between the line of flight and the beam direction) is equal to the rapidity. The accurate measurement of the angle θ is well within the capabilities of the measuring system. The preferred variable therefore is the rapidity for gammas.

The gammas are assumed to originate in the decays of π^0s and it is the properties of the π^0s that are of principal interest. For experiments with sufficient data the π^0 spectra can be extracted from the gamma data. Lacking that possibility, the most useful procedure is to compare the gamma distributions to that of gammas generated by Monte Carlo simulated decays of known π^+ and π^- distributions.

The decay of the π^0 to two gammas is isotropic in the π^0 rest frame. A π^0 of rapidity y will decay to gammas whose rapidity spectrum will be several units wide but will

be fairly sharply peaked at y. Thus the spectrum will be generally similar to a pi^0 spectrum that has been smeared.

The gamma rapidity spectrum of neon and hydrogen events at 200 GeV/c is shown in Figure 37. The neon gammas are more numerous in the central region and in the target fragmentation region. The increased gamma production is smaller in the target hemisphere than one would naively expect from the charged track data, but this is probably due to smearing effect of the pi^0 decay.

In Figure 38 the gamma rapidity spectra are compared to Monte Carlo generated gamma spectra of pi+ and pi- decays to two gammas. Each charged pion was allowed to decay twenty times to gammas to minimize statistical fluctuations. The real gamma rapidity distribution is bracketed by those of the Monte Carlo gammas for all rapidities $y > 0.5$. The gamma data below $y = 0.5$ are consistent with the Monte Carlo gammas if corrections for the unmeasured gammas of energy < 50 MeV are made. The pi^0 rapidity spectrum is similar to the pi+ and pi- spectra with magnitude close to an average of the charged pion data.

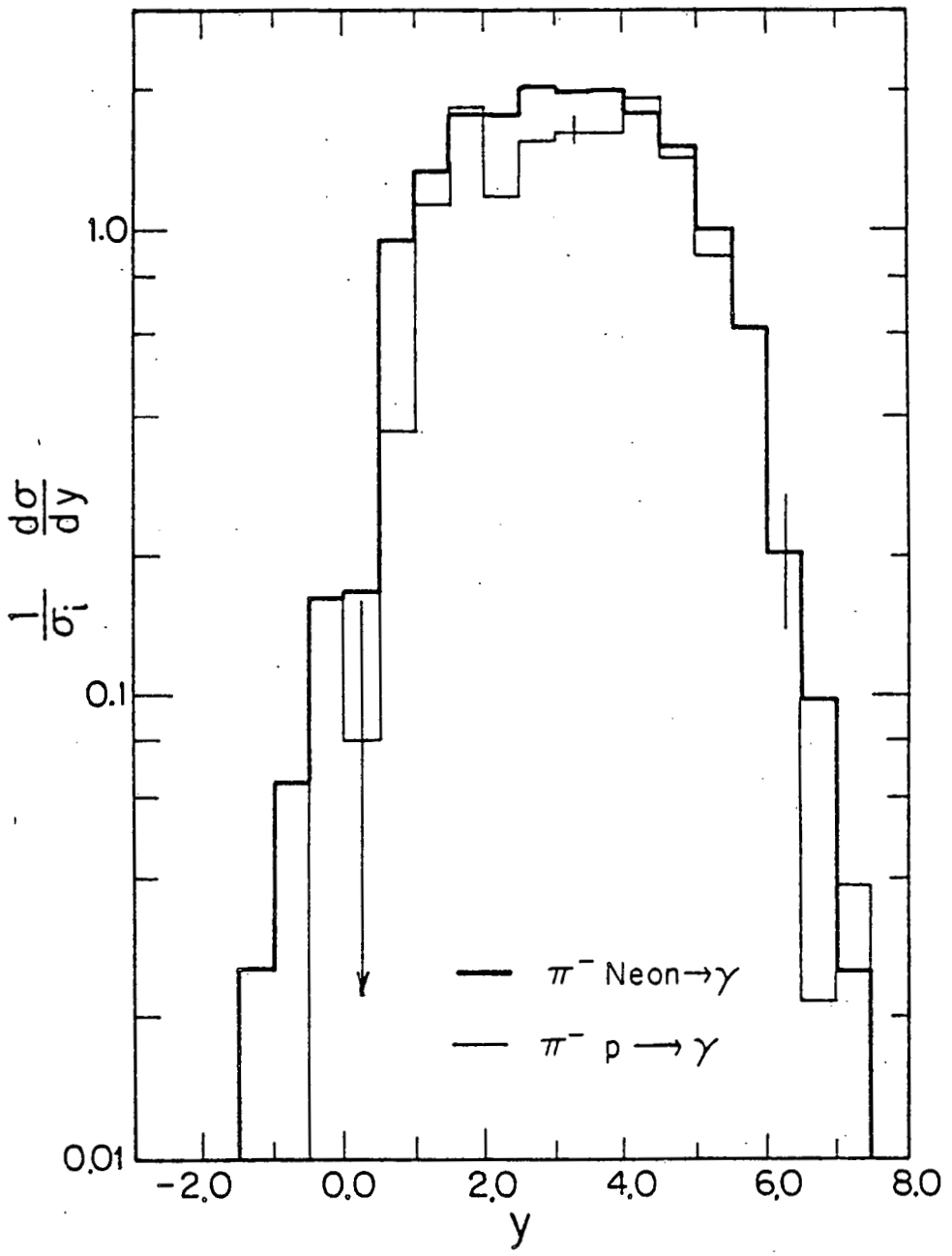

Figure 37: Gamma rapidity 200 GeV/c neon and hydrogen.

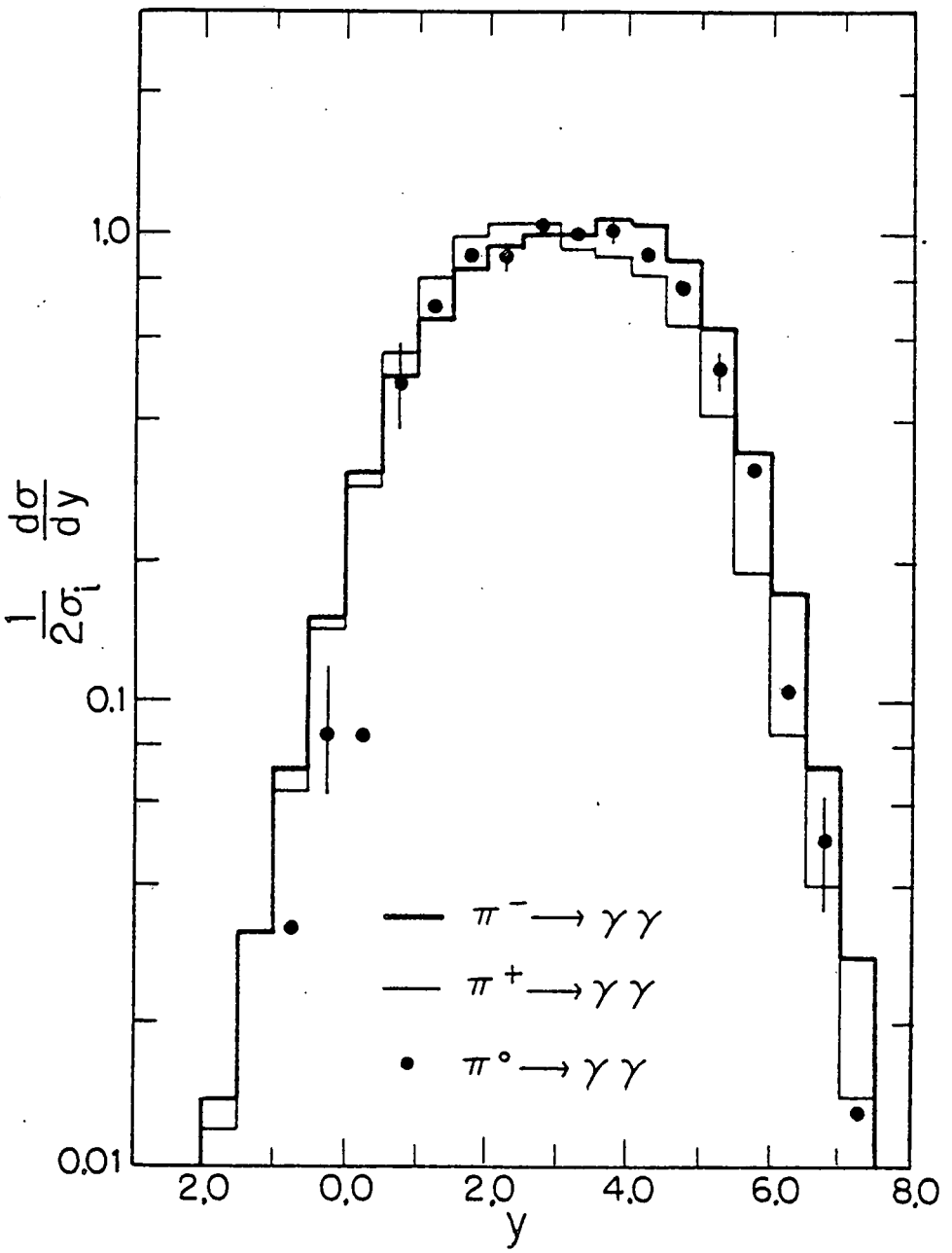

Figure 38: Monte Carlo gamma rapidity distribution.

3.2.4 Correlations

The strong correlation between <pi±> and NP found previously should be reflected in the rapidity distributions. The average rapidity of pi± and gammas for all events with NP protons <y>NP was calculated and plotted in Figure 40. For comparison the average rapidity of <pi±> for 200 GeV/c pi-p events was found to be <y> = 3.30. The lab rapidity of the center of mass in 200 GeV/c pi- interactions is

pi-p = 3.03

pi- (2p) = 2.68

pi- (3p) = 2.48

The center of mass rapidity was also calculated for targets of effective mass double or triple the nucleon mass. The decline of <y> with NP is evidence that the effective target mass is increasing with NP as has been previously suggested. Comparison of neon and hydrogen events of identical multiplicity show the average rapidity of the neon events is always smaller than that of hydrogen. events.

In Figure 39, the rapidity distribution for pi± are plotted for events with NP = 0,1; NP = 2,3,4 and NP $\geq$ 5. The center of the rapidity spectrum is seen to shift to lower y as NP increases. The widths of the y distributions also seem to decrease as NP rises. The center of the respective distributions are shown by the arrows in Figure 39 and are shown below.

	min	$pi^{\pm}$,°	
$\langle y \rangle$ =	3.27	3.47	NP = 0,1
$\langle y \rangle$ =	2.92	3.04	NP = 2,3,4
$\langle y \rangle$ =	2.72	2.81	NP $\geq$ 5

The rapidity distributions contain minimum ionizing protons. $\langle y \rangle$ was calculated for all minimum tracks and then corrected for the fast proton contamination (assuming 0.44 proton per event with $\langle y \rangle$ = 1.5). The distributions in Figure 39 and 40 are consistent with increasing target mass as NP rises. The NP$\geq$ 5 events are consistent with collisions on two or three nucleons.

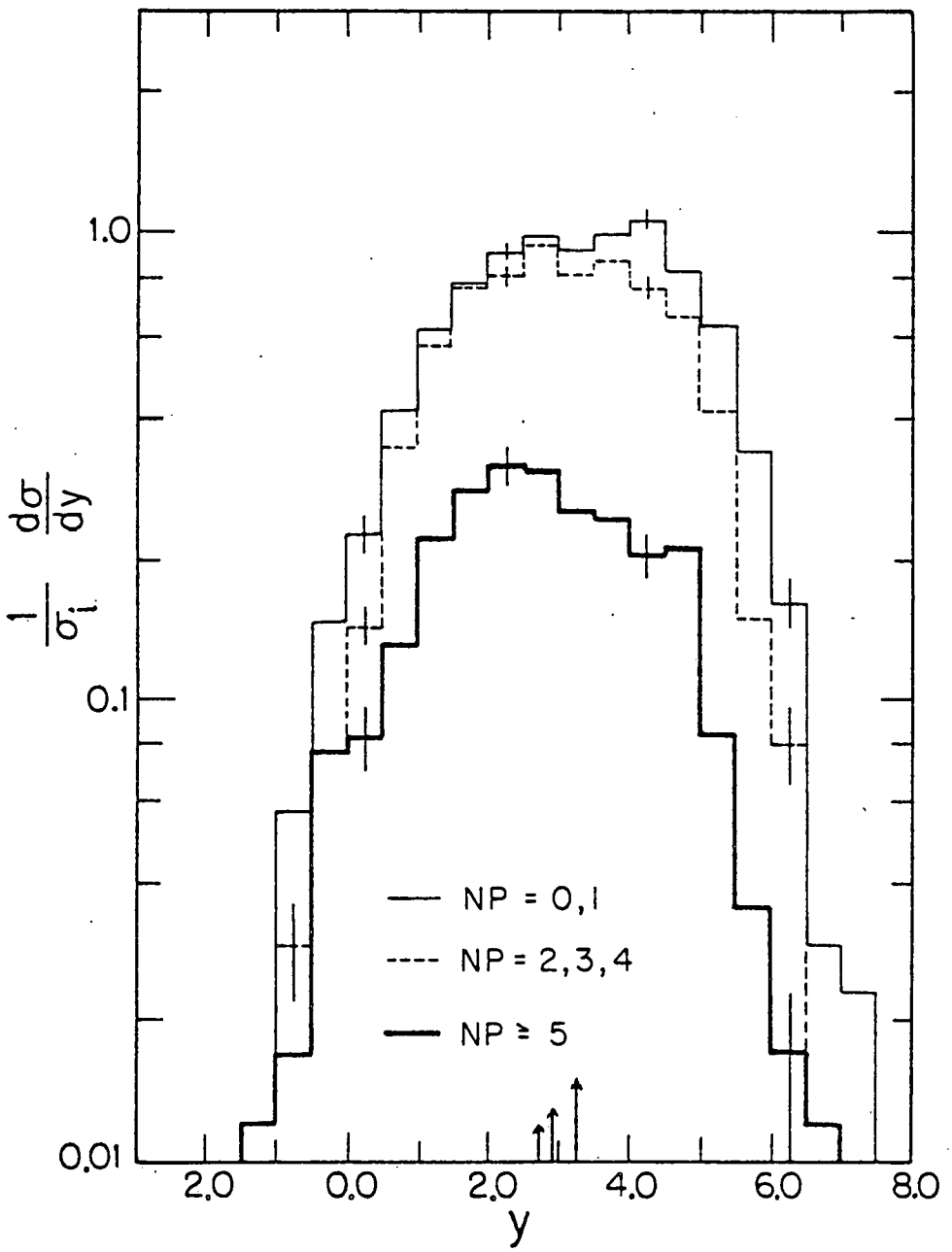

Figure 39: Pion rapidity vs NP. Pi± rapidity for NP = 0,1; NP = 2,3,4; and NP = 5. The y of each distribution is represented by arrows with NP = 0,1 corresponding to the rightmost arrow.

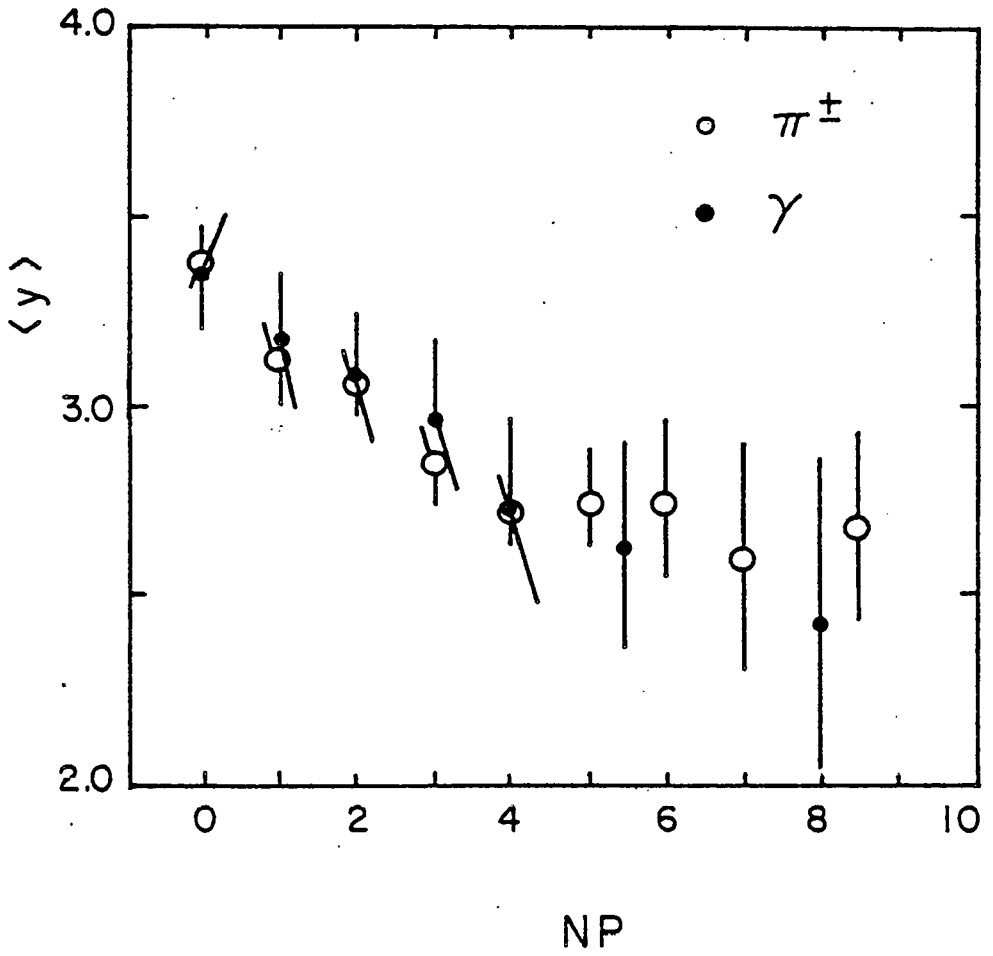

Figure 40: Average rapidity vs NP (number of visible protons).

Chapter IV

CONCLUSIONS

The multiplicity distributions of pi-neon interactions have been shown to be quite similar to hydrogen interactions apart from a slight increase in the average multiplicity. The R ratio of 1.21 ± 0.05 is almost identical for charged and neutral pions and is energy independent. After corrections for undetected gamma conversions and minimum ionizing protons were made, the topological cross sections exhibit KNO scaling. Violations of KNO scaling are seen if only events with a fixed number of protons are considered.

Monte Carlo studies of $pi^+ \rightarrow \gamma\gamma$ and $pi^- \rightarrow \gamma\gamma$ show that the pi^0 rapidity spectra have approximately the same magnitude and shape as the charged pions. The $< pi^0 >$ is about $1/2 < pi^{\pm} >$. Correlations between $< pi^0 >$ and $< pi^{\pm} >$ (NMIN) support two component models (diffractive and non-resonance) of particle production. For large NMIN the $<\gamma>$ is independent of NMIN and about 1.5 times $<\gamma>$ of hydrogen interactions. The neon f_2^{00} moment was calculated to be 3.8 ± 1.1. Both the f_2^{00} and the large NMIN behavior of $<\gamma>$ reflect the increased center of mass energy available to pion - nucleus collisions.

The asymptotic behavior ($s \rightarrow \infty$) of pion p distributions in the region $-0.4 \leq p_{\parallel} \leq 0.2$ was shown to be analogous to that seen in hydrogen data. The leading particle effect is significant even for beam energies greater than this experiment. The asymptotic ratio (R) of the neon multiplicity to the hydrogen multiplicity is in the range $-0.4 \leq p_{\parallel} \leq 0.2$ is strongly charge dependent with an average value of 2.2 ± 0.4.

In contrast to the pi$\pm$ distributions little energy dependence is exhibited by the proton momentum distribution.

Studies of the rapidity distribution of the increased particle production show significant production for lab rapidities ≤ 5.0. For $2 < y < 5$, R(y) is charge independent. Comparisons with hydrogen at small y show marked differences in pi+ and pi- production which can be attributed to the neutron - like neon events.

In the central region $1 < y < 5$ R(y) has an average value of 1.28 ± 0.2 and agrees well with a parton model which predicts $R(y) = 1.27$ at $y=3.0$. The data disagree with the model prediction for the shape of the R(y) function. The excess particle production in the beam hemisphere would seem to rule out the energy flux cascade model. The lack of scaling for events with fixed NP contradicts the simpler versions of the CTM. Ctm's which restrict predictions to regions outside the target region are not tested. However,

the CTM has difficulties in explaining the energy independence of the proton momentum distribution.

Appendix A

INTERACTION LENGTHS

Using the composition of the bubble chamber liquid and published cross sections the interaction probabilities for specific particles were calculated. These values were subsequently used for constructing gamma weights or in predicting the number of beam interactions.

For a beam of N particles the number of interactions in an interval dx is given by:

$$dN(x) = -\sigma * P * N(x) dx$$

Where N(x) is the number of beam particles at a position x, P is the density of scattering centers per unit volume and is the cross section (dimensions area/scattering center). Integrating the above equation and then taking the exponential on both sides:

$$\ln(N(x)) = -\sigma * P * x + C$$

$$N(x) = C * \exp(-\sigma * P * x)$$

If we set $N(0)=N^0$ then $C=N^0$. Defining the interaction length IL as

$$IL = 1.0/(\sigma * P)$$

then

$$N(x) = N^0 * \exp(-x/IL)$$

IL has the correct dimension of length. If a beam of N^0 particles tranverses a thickness IL of material then it is reduced 1/e in intensity. The number of interactions in a thickness L is

$$N(L) - N(0) = N^0(1.0 - \exp(-L/IL))$$

If N^0 is 1 then $(1.0 - \exp(-L/IL))$ is the probability the particle will interact in that distance.

For this experiment we have a mixture of two types of scattering centers, hydrogen and neon.

$$\sigma * P = \sigma(HYD) * P(HYD) + \sigma(NEON) * P(NEON)$$

Where P(HYD) and P(NEON) are the number of atoms/cc. We calculate the interaction length using the molar weight of neon(20.18 gm) and hydrogen(2.016 gm), the density of the mixture(.255gm) and Avogadro's number($6.023*10^{23}$ atoms or molecules per mole). One mole(M) of mixture weighs

$$M\ WT = 0.309M * 20.18\ gm/M(Ne) + 0.691M * 2.016\ gm/M$$

$$\%\ Ne\ by\ weight = \frac{.309\ M * 20.18\ gm/M}{M\ WT}$$

$$P(Ne) = \frac{0.255gm/cc * \%Ne * 6.023*10^{23}\ atoms/M}{20.18\ gm/M}$$

$$P(Ne) = 6.21 \pm 0.3 *10^{21}\ atoms/cc$$

$$P(Hyd) = 27.8 \pm 1.8 *10^{21}\ atoms/cc$$

The density of hydrogen was similarly calculated. Using the published cross sections of 200 GeV/c pi- on hydrogen and neon

(hydrogen) = 24.01 mb (18)

(neon) = 270 mb (8)

The interaction length is calculated to be:

IL = 427± 17 cm.

Gammas undergo several electromagnetic interactions, only two of which are important at energies of interest. Compton scattering produces a gamma of reduced energy and an electron which is visible in the bubble chamber. In pair production the positron and electron share the incident gamma's energy. Cross sections for both processes are functions of the gamma's energy. For the purposes of calculating gamma weights the total interaction length (IL), the Compton interaction length(CL),and the pair conversion length(PL) are needed. The relationship between them is expressed by

$$\sigma_T = \sigma_p + \sigma_c$$

$$1.0/IL = 1.0/PL + 1.0/CL$$

As before each cross section has contributions from neon and hydrogen. The pair and total interaction lengths are shown in Figure 41.

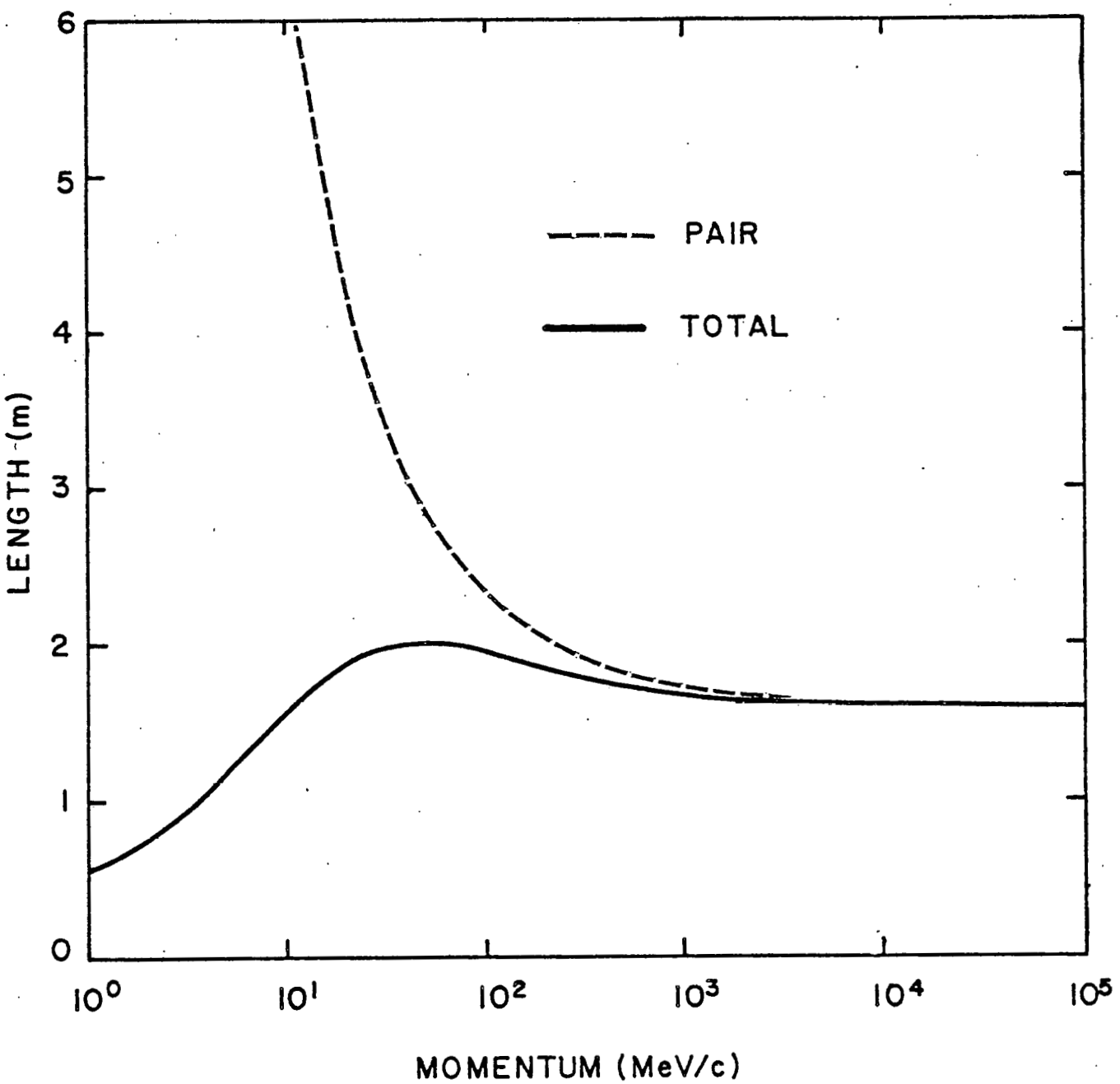

Figure 41: Gamma interaction lengths. Pair conversion and total interaction lengths for gammas in this experiment.

Appendix E

TOTAL CROSS SECTION

Using the interaction length for 200 GeV/c pi- the expected number of beam interactions was calculated. This predicted value agrees within errors to the observed number for events with greater than two minimum tracks. The scanning efficiency for events with fewer than two minimum tracks is shown to be approximately 85%. The observed events are normalized to the published cross sections giving the sensitivity of this experiment as 63 events/mb for hydrogen and 14 events/mb for neon. The fraction of events that are attributable to hydrogen is calculated to be 25% (inelastic only).

The distribution in the number of beam tracks per frame is shown in Figure 42. There were 28,850 frames which satisfied the scan criteria of good quality beam tracks and no interactions before the interaction region. The interaction region is 25.4 $\pm$.2 cm. long. The probability for a track interacting in this length is

$$p = 1.0 - \exp(-25.4/438).$$

The previously calculated interaction length for pi- (427 cm) was corrected for beam contamination. The probability

of a frame with N beam tracks having one or more interactions is

$$P(N) = N * p$$

However, only frames with a single interaction were accepted. The probability for this occuring is

$$P(N) = N * p - \sum_{M=2}^{N} \frac{N! * p^M * (-1)^{M-1}}{(N-M)! * M!}$$

Summing over all good frames the expected number of interactions is

$$N(\text{total}) = 5466 \pm 190$$

The observed number of events is 5252 somewhat below the predicted value. As events with 1 or 2 minimum tracks are easily missed on the scan table the events were divided into those with greater than 2 minimum tracks and those with less. The hydrogen cross section for 0 and 2 prongs has been well measured (Table 9). The neon component has been estimated by assuming KNO scaling for events with less than 3 minimum tracks.

Number of events

	Scan	Predicted
≤ 2	444	522
≥ 3	4808	4944 ± 171

Since the experimental uncertainty in the predicted number of events is larger than the errors caused by scan effici-

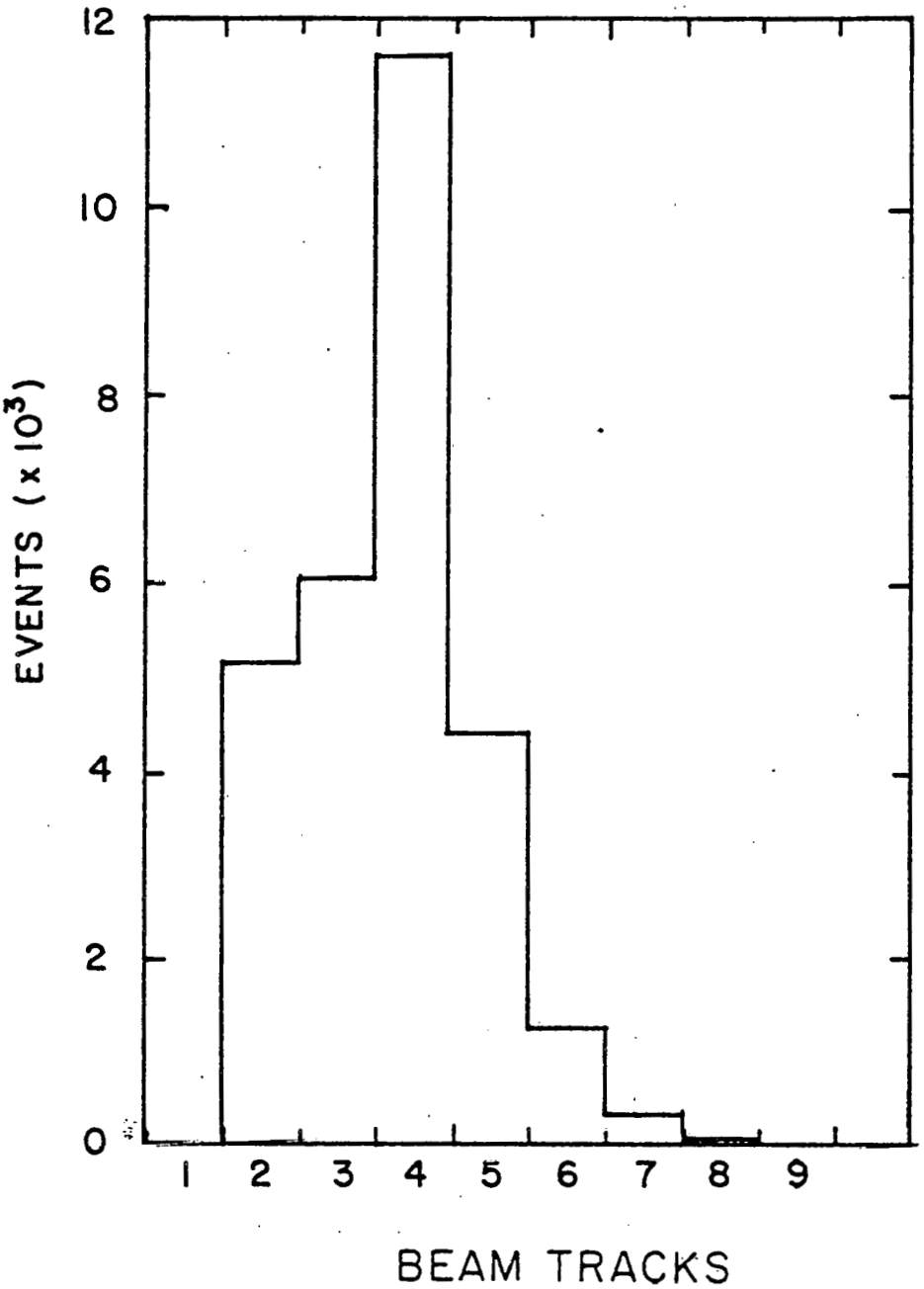

Figure 42: Beam track distribution. Distribution in number of beam tracks for all good frames. (See text.)

ency or statistics the observed distribution of events was normalized to published cross sections for events with greater than 2 minimum tracks. The sensitivity of this experiment is thus

63.06 events/mb hydrogen

14.09 events/mb neon

TABLE 9

HYDROGEN MULTIPLICITY DISTRIBUTION

PRONGS	CROSS SECTION IN MB	% OF EVENTS WITH VISIBLE PROTON
0	0.01	0
2	1.68	75
4	3.53	49
6	3.93	31
8	4.14	22
10	3.33	19
12	2.21	14
14	1.12	12
16	0.62	11
18	0.31	10
20	0.1	6
total(inelastic)	21.01	

Appendix C

STRANGE PARTICLE CONVERSION WEIGHTS

The strange particles(K^0, Λ) decay by weak interactions with well defined lifetimes(ML). The probability that a particle decays between $t=t^0$ and t is

$$p = \exp(-t^0/\gamma * ML) - \exp(-t/\gamma * ML).$$

The γ multiplying the lifetime properly accounts for the relativistic time dilation if the particle is moving in the lab frame. This probability is more conveniently expressed in terms of the distance x the particle decays from its production point and the mean decay length (DL).

$$t/\gamma * ML \dashrightarrow x/DL$$

where

$$DL = \frac{P(MeV/c)}{M(MeV/c^2)} * ML$$

The decay lengths for K^0 and Λ are plotted in Figure 43.

The conversion weight for the strange particle is then 1.0/p times 1.0/B.R., the branching ratio for the decay of interest. Since only charged tracks are visible in the bubble chamber only decays to charged tracks are counted. The two decays seen in the bubble chamber are;

$K^0 \rightarrow \pi^+ \pi^-$ B.R. 69%

$\Lambda \rightarrow p\ \pi^-$ B.R. 65%

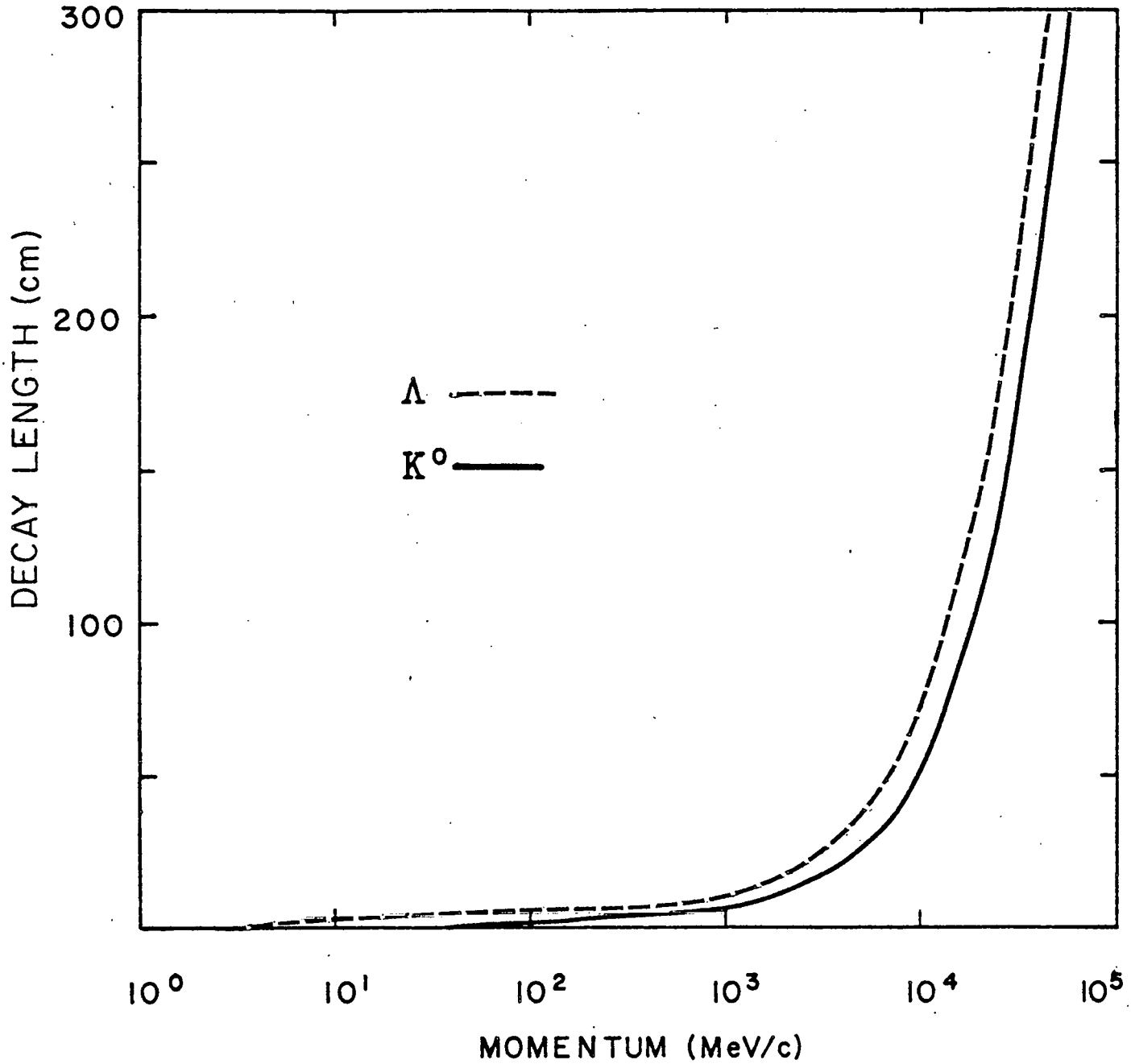

Figure 43: Strange particle decay lengths.

Appendix D

NEUTRAL PARTICLE SCANNING EFFICIENCY

The scanning efficiency for neutral decays or interactions is not constant over the chamber volume. Two effects are dominant. Particles converting near the edge of the chamber or photograph are missed. The conversion or interaction vertex of neutrals near the primary vertex are often obscured by charged tracks. The products of such conversions are then asummed to come from the primary vertex and are included in the NMIN count. The loss of neutrals not only causes a underestimation of the neutral cross sections but is also likely to distort the inclusive distributions.

Much experimentation went into defining a neutral conversion region in which the detection efficiency was high and no type of particle was preferentially missed. A valuable tool in the study of detection efficiencies is the variable Q defined as

$$Q = \frac{\exp(S1/IL) - \exp(x/IL)}{\exp(S1/IL) - \exp(S2/IL)}$$

Where x is the distance of the neutral decay from the primary vertex. S1 and S2 are the minimum and maximum allowed conversion distances. IL is the interaction length for a

gamma of that energy. For strange particles IL is replaced by DL the mean decay length of the particle. If the detection efficiency is unbiased then it can be shown that the Q plot will be uniformly populated between 0.0 and 1.0. A Q plot of all measured gammas in the conversion region is shown in Figure 44 a. A loss of gammas at small values of Q is evident. If the allowed conversions are restricted to gammas converting further than 10 cm from the primary vertex (S1=10.0) the Q plot is Figure 44 b. This plot is consistent with an unbiased detection efficiency over the entire conversion region.

The expected number of gamma conversions $\leq$10 cm was calculated from the measured gamma population. The expected number of conversions is:

$$MG = \sum \frac{1.0 - \exp(-10.0/IL)}{\exp(-10.0/IL) - \exp(-S2/IL)}$$

where the sum is over all gammas in the conversion region. This expected number of conversions was calculated for each set of events of equal NMIN (minimum ionizing tracks). The expected and the observed number of gamma conversions $\leq$10 cm are seen in Figure 45.

The number of events with NMIN scanned tracks can be written as:

$$S(NMIN) = R(NMIN) - X(NMIN) + X(NMIN - 2)$$

R(NMIN) is the true number of events with NMIN minimum tracks. X(NMIN) are the events with NMIN minimum tracks which were scanned and measured to have NMIN + 2 minimum tracks because of an unseen gamma conversion. If there is at most one unrecognized gamma per event then X(NMIN) is equal to the number of gammas not seen for the scan NMIN sample. The true NMIN distribution can then be calculated using the scan NMIN distribution and the predicted and observed number of gammas.

Figure 44: Q plot for measured gammas.
See page 126 for details.

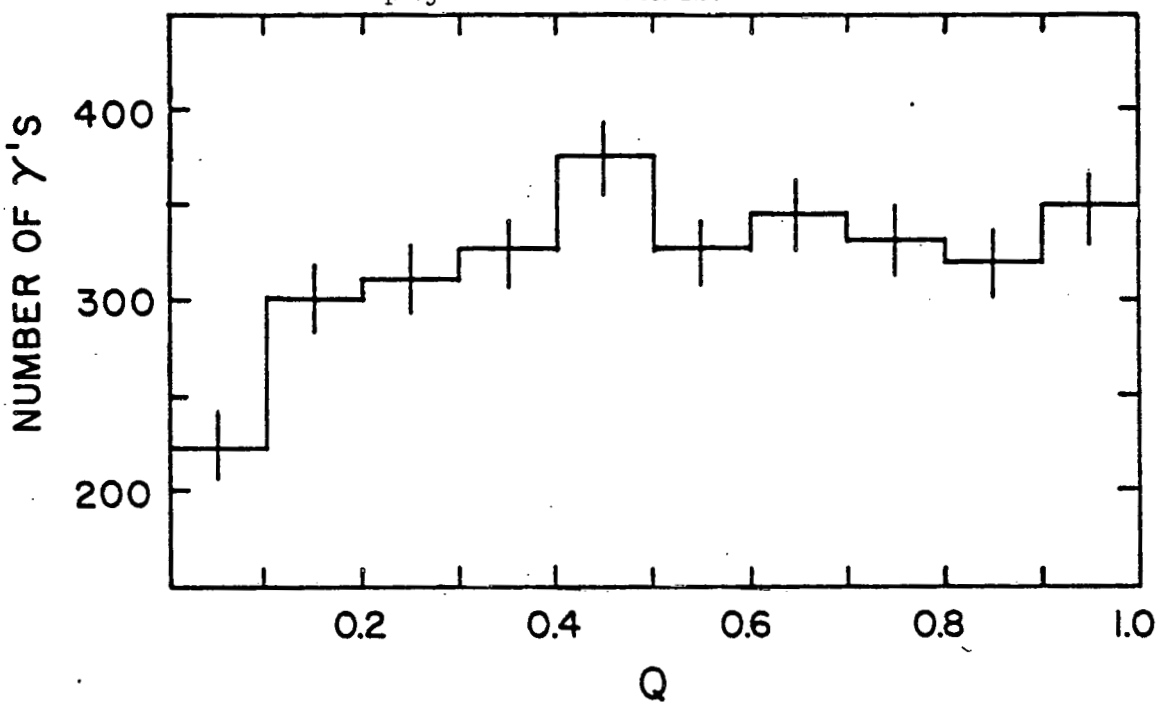

a) All gammas inside conversion region.

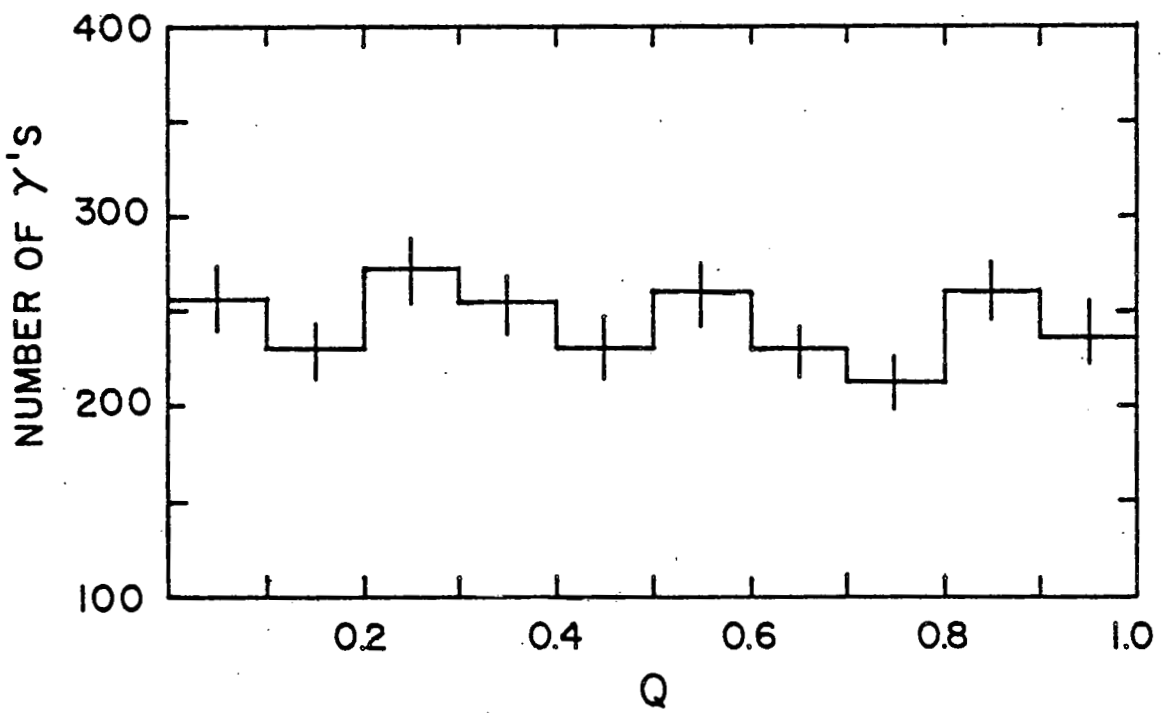

b) All gammas inside conversion region and further than 10 cm from the primary vertex.

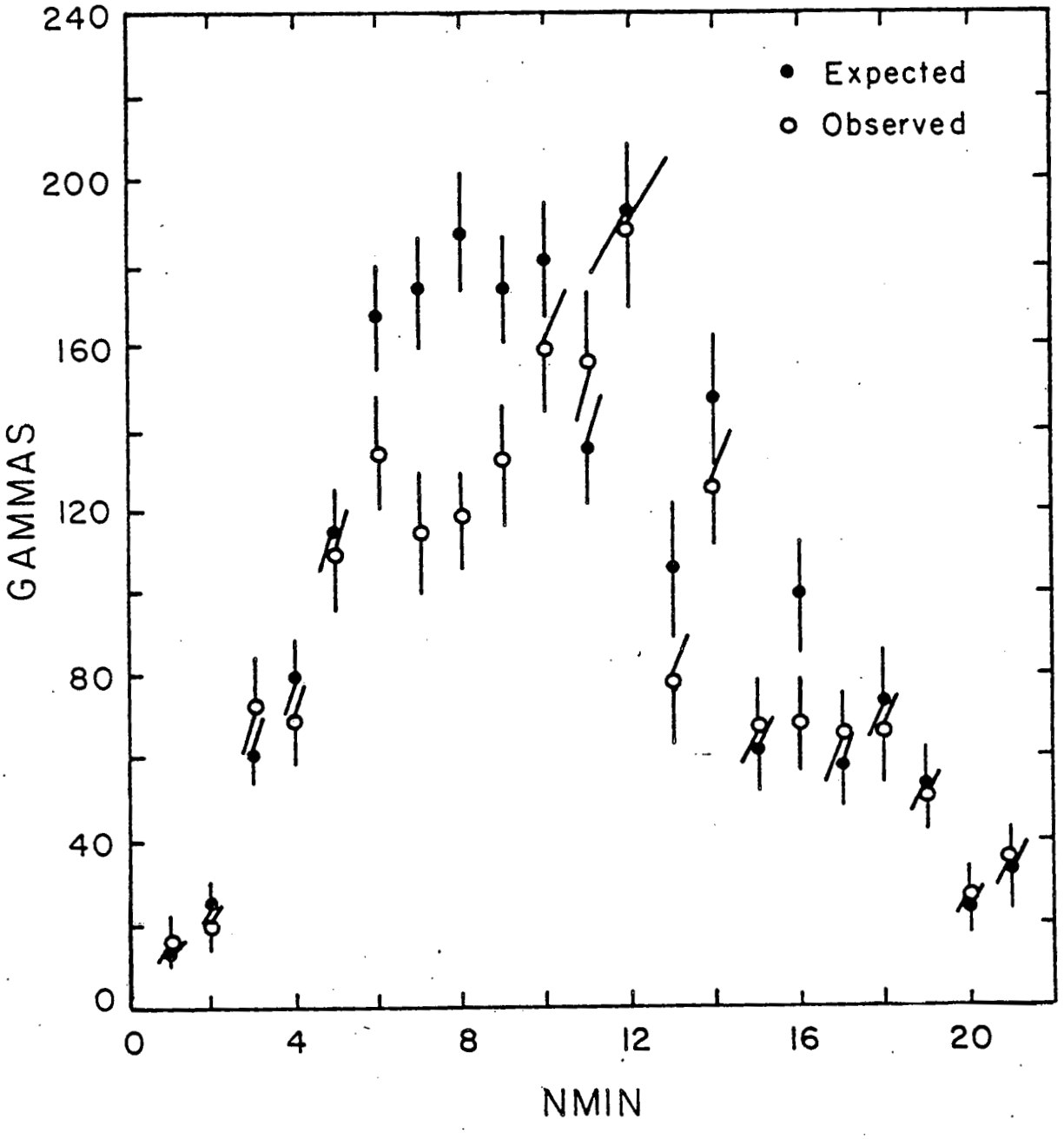

Figure 45: Number of gamma conversions ≤ 10 cm. The number of expected gamma conversions less than 10 cm from the primary vertex is compared with number of conversions observed. Discrepencies between the two values are evidence for unseen gamma conversions.

Appendix E

FAST PROTONS

Previous experiments(12,10) on nuclear targets have found large numbers of minimum ionizing protons. No method for identifying these protons exists on an event by event basis in the bubble chamber. However, the number of such fast protons (momentum > 0.8 GeV/c) can be estimated by statistical means. This procedure is based on the invariance of strong interactions under rotations in isospin space and the insensitivity of single particle distributions in the target fragmentation region to the projectile quantum numbers.

The inclusive reaction

pi- neon -> pi-

with isospin values

I=	1	0	1
I3=	-1	0	-1

becomes

pi+ neon -> pi+

I3=	+1	0	+1

under rotation of 180° about the I2 axis. Since strong interactions are invariant under this rotation the inclusive

distributions of the produced pi- in reaction (1) should be identical to those of the produced pi+ in reaction (2). (This is true if the incident pi beams in reactions 1 and 2 are of the same energy.) If the positive minimum tracks of reaction (2) have larger cross sections than the corresponding negative minimum tracks of reaction (1) then that difference can only be attributed to fast protons being included in the postive sample. The same argument holds for the inclusive reactions

pi- neon -> pi+

and

pi+ neon -> pi-.

This procedure has been used on neon data(12) at lower energies to estimate the proton spectrum.

The above procedure utilizes experimental information of both pi+ and pi- neon interactions. This experiment is limited to a pi- beam. An estimate of pi+ neon --> pi- data is necessary if the minimum ionizing protons are to be extracted from the positive minimum data. Such an estimate (valid in the target fragmentation region) can be made using the pi- neon data and several reasonable assumptions about the behavior of high energy interactions.

That the inclusive particle distributions in the target fragmentation region are independent of the beam charge at $s^{-1/2} = 0$ (s is center of mass energy) has been proposed by

several theorists (24). Data at several beam energies with pi+ and pi- beams are consistent with this assumption (see Figure 30). Complete independence, however, as not been reached at the energy of this experiment ($s^{-1/2} = 0.0516$). The residual dependence on the charge of the beam is demonstrated by the slightly higher cross sections for beam - like particles when compared to nonbeam - like particles. The excess of beam - like particles was found to be constant through the longitudinal momentum range -0.4 to 1.6 GeV/c for pi+p and pi-p interactions at 100 GeV/c by Whitmore et al. (23) The relationship between pion production by pi+ and pi- beams in the target fragmentation region is shown in Figure 46.

A few definitions will aid the following discussions. We will be interested in the invariant structure function

$$E \frac{d\sigma}{dp_{||}}$$

of pi+ and pi- produced by pi+ and pi- beams incident on protons.

$$E \frac{d\sigma}{dp_{||}} (+ -) = pf(+ -)$$

will refer to pi-'s produced by a pi+p interaction. Also,

$$E \frac{d\sigma}{dp_{||}} (- -) = pf(- -)$$

will refer to pi-'s produced by a pi-p interaction. The ratio of two structure functions will be written as

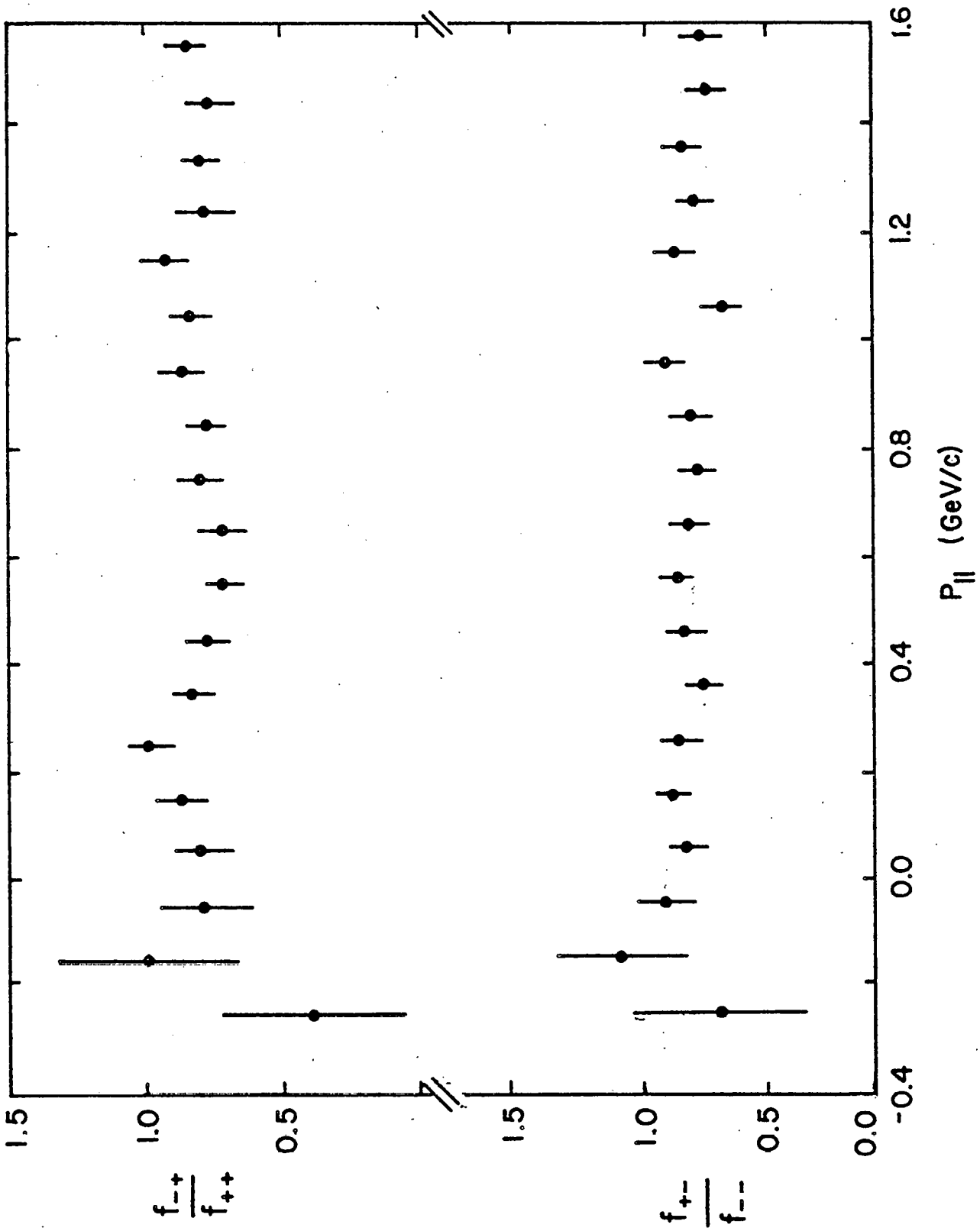

Figure 46: Charge dependence in target fragmentation region. See text. Data are from reference (23).

$$\frac{E\, d\sigma(+\ -)/dp}{E\, d\sigma(-\ -)/dp} = \frac{pf(+\ -)}{pf(-\ -)}$$

For pi-'s produced by pi+ on a neutron or neon target nf(+ -) and Nef(+ -) will be used. The data of Figure 46 show that the ratios pf(+ -)/pf(+ +) and pf(- +)/pf(+ +) are constant and equal to each other in the longitudinal momentum range -0.4 to 1.6 GeV/c.

The average value of pf(+ -)/pf(- -) can be taken from Figure 30 where

$$\int_{-0.4}^{0.2} pf(+\ -)\ dp_{||}$$

is plotted vs $s^{-1/2}$. No experimental data for pi+p at 200 GeV/c exist. Linear or quadratic fits were made to the data in Figure 30 to calculate

$$\frac{pf(-\ +)}{pf(+\ +)} = \frac{pf(+\ -)}{pf(-\ -)} = 0.91 \pm 0.05$$

at 200 GeV/c.

To estimate the minimum ionizing protons we need to calculate the relationship between Nef(+ +) and Nef(- +). A reasonable approximation is

$$Nef(+\ +) \simeq \frac{A^{2/3}}{2} * [pf(+\ +) + nf(+\ +)]$$

Our earlier work found

$$pf(+\ +) = \frac{pf(-\ +)}{0.91}$$

Again no experimental data exist for pi+n -> pi+. By isospin symmetry

$$nf(+\ +) = pf(-\ -)$$

And

$$pf(-\ -) = \frac{pf(+\ -)}{0.91} = \frac{nf(-\ +)}{0.91}$$

Nef(+ +) can then be given by

$$Nef(+\ +) = \frac{A^{2/3}}{2} * [pf(+\ +) + nf(+\ +)] =$$

$$= \frac{A^{2/3}}{2} \frac{1}{0.91} [pf(-\ +) + nf(-\ +)]$$

$$= \frac{1}{0.91} * Nef(-\ +)$$

The final relationship is

$$Nef(-\ -) = \frac{Nef(-\ +)}{0.91}$$

Nef(- +) and Nef(- -) are plotted in Figure 47 The integrated value of Nef(+ +)/Nef(- -) between -0.4 GeV/c and 0.2 GeV/c is 0.91 $\pm$ 0.08 in excellent agreement with the predicted value of 0.9. Above 0.2 GeV/c the ratio is greater than 0.91 indicating the presence of minimum ionizing protons. The estimated longitudinal momentum distribution of the protons is given by

$$E \frac{d\sigma}{dp_{||}} \text{ (protons)} = Nef(-\ +) - 0.91 * Nef(-\ -)$$

Integrating over the entire proton excess the average number of protons per event can be calculated to be

$$\langle \text{minimum ionizing protons} \rangle = 0.44 \pm 0.14$$

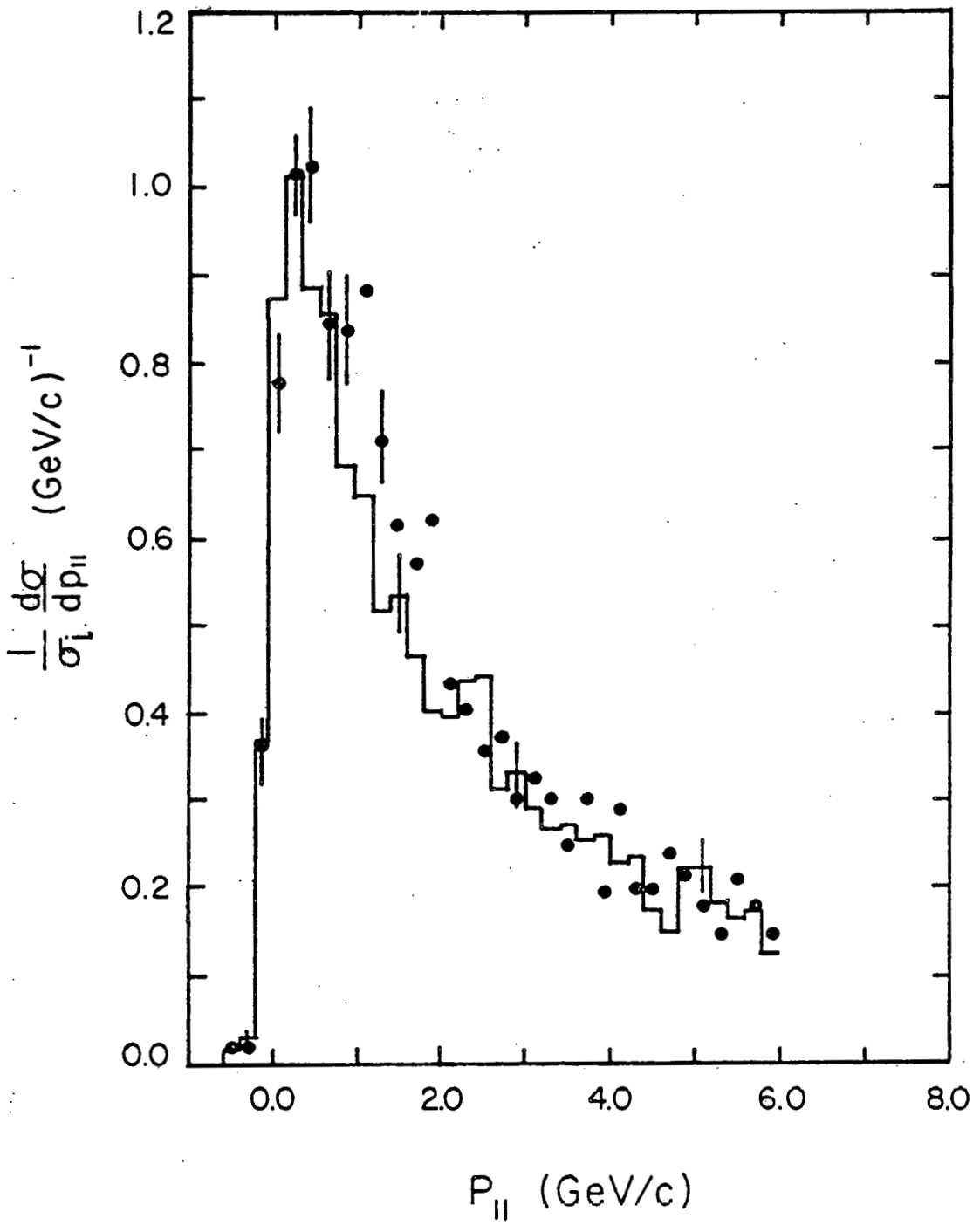

Figure 47: P_{II} momentum distribution of positive minimum tracks. P_{II} for positive minimum ionizing tracks compared to expected p_{II} distribution for pi+ = ($\frac{0.91}{\sigma_i}$ $\frac{d\sigma}{dp_{II}}$ pi-). The excess positive tracks are attributed to minimum ionizing protons.

BIBLIOGRAPHY

1. K.Gottfried, Phys. Rev. Lett 32 957 (1974).

2. W.Busza, Proceedings of the VI Internatitonal Congerence on High Energy Physics and Nuclear Structure, Santa Fe and Los Alamos, 1975.

3. Z.Koba, H.B.Nielsen and P.Oleson, Nucl. Physics B40 317 (1972).

4. R.P.Feynman, Phys. Rev. Lett. 23 1415 (1969).

5. M.Jacob, "Proceedings of the XVIth International Conference on High-Energy Physics" (Chicago - Batavia, 1972) 373.

6. W.Morris et al., Phys. Lett. 56B 395 (1975).

7. R.L.Bolduc, unpublished PhD dissertation, Notre Dame (1979).

8. S.P.Denisov et al., Nucl. Physics B61 62 (1973).

9. G.Berlad, A.Dar and G.Eilam, Phys. Rev. D13 161 (1976), and references therein.

10. M.A. Faessler et al., "Inelastic Hadron-Nucleus Collisions at 20 and 37 GeV/c" CERN Preprint (1979)

11. W.Busza et al., Reported at XVIII International Conference on High Energy Physics, Tbilsi, 1976.

12. W.M.Yeager et al., Phys. Rev. D16 1294 (1977).

13. L.Bergstrom and S.Fredriksson, Phys. Lett. 68B 177 (1977).

14. F.Takagi, Tohuku University preprint TU/77/176 (1977).

15. S.Fredriksson, Nucl. Physics B111 167 (1976).

16. S.J.Brodsky, J.F.Gunion and J.H.Kuhn, Phys. Rev. Lett. 39 1120 (1977).

17. R.P.Feynman, Photon - Hadron Interactions, (Benjamin, Reading, Mass., 1972), and references therein.

18. D.Bogert et al., Phys. Rev. Lett. 31 1271 (1973).

19. F.T.Solmitz, A.D.Johnson, T.B.Day, "Three View Geometry Program", Alvarez Group Programming Note P-117 U. of Calif., Berkeley. T.B.Day, "TVGP-SQUAW Operational Information" 1967-1973 Supplements AEC ORO-2504-100. P.L.Bastien et al., Computer Physics Communications 2 394 (1971).

20. L.R.Fortney, "A Branch off the PEPR Tree" Int. Conf. on Data Handling Systems in High Energy Physics (1970). "Resolution Improvement for Flying Spot Digitizers" Proceedings of the Oxford Conference on Computer Scanning (1974).

21. J.R.Elliott et al., Phys. Rev. D17 83 (1978).

22. Internal report (unpublished), Notre Dame-Duke-Toronto.

23. J. Whitmore et al., Phys. Rev. D 16 3137(1979).

24. J.Benecke et al., Phys. Rev. 188, 2159 (1969).

25. W.D.Walker private communication.

26. T.Kafka et al., Phys. Rev. D 19 76(1979).

27. D.Horn and A.Schwimmer,Nucl. Physics B52 627(1973).